APPENDIX A – EQUIPMENT RODEO ON HOT MIX ASPHALT

A.1. INTRODUCTION

Figure A.1.1 illustrates an aerial view of the project location. The candidate project for this rodeo was located in El Dorado County, California near El Dorado Hills. This project was part of the construction of the new Silva Valley Parkway and its undercrossing with US 50 highway. Figure A.1.2 shows the location of the test section within the construction area. Figure A.1.3 demonstrates a typical cross section of the road. The project contains a 6.5 in.-thick HMA layer (which was placed and compacted at two lifts of 2.5 in and one lift of 1.5 in.) on top of an 18-in.-thick base layer. The base layer was compacted before the research team arrived at the site.

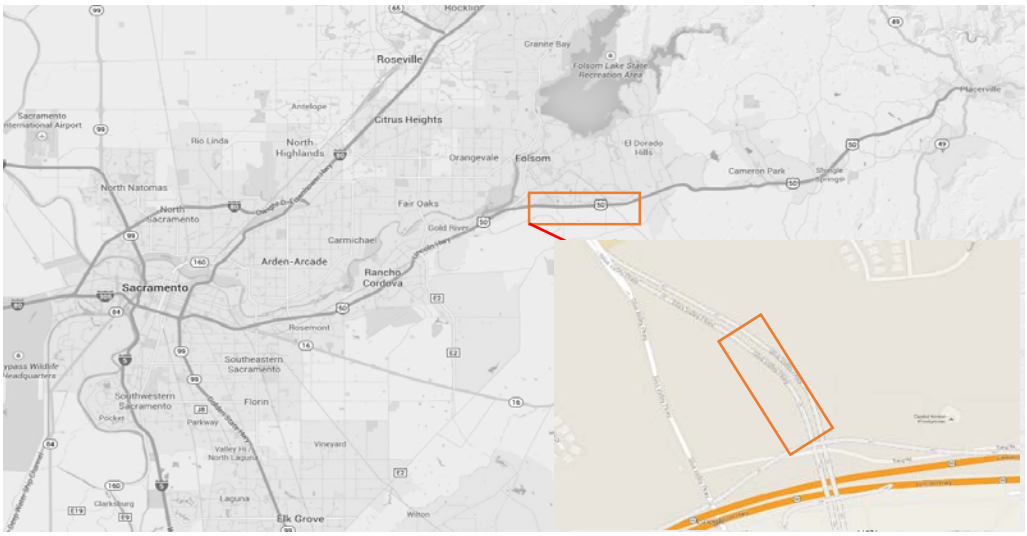

Figure A.1.1. Aerial View of the Project Location

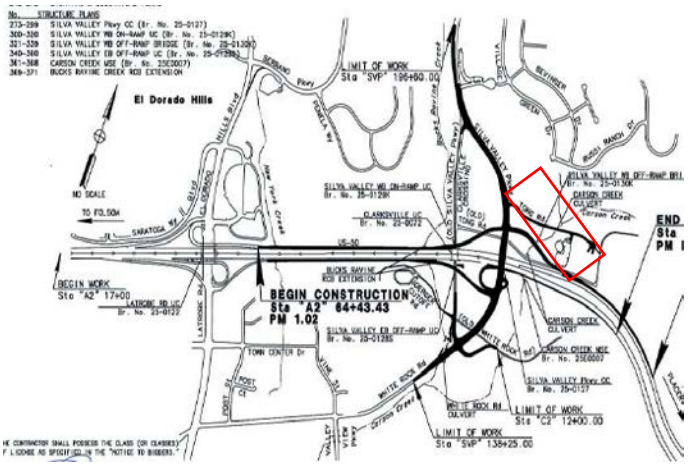

Figure A.1.2. Location of Construction Site

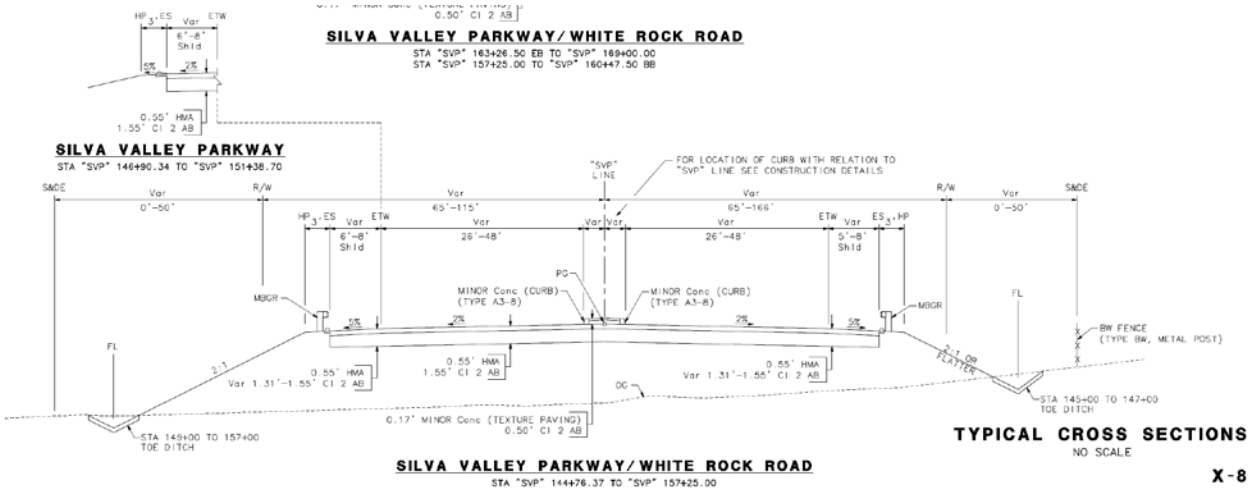

Figure A.1.3. Typical Cross Section of the Designated Road

Figure A.1.4 contains a schematic of the test section. The NDT testing spots were marked along the selected test section. The test grid consisted of 33 points along lines A, B and C as shown in Figure A.1.4. Figure A.1.5 demonstrates the test grid as marked prior to the spot tests.

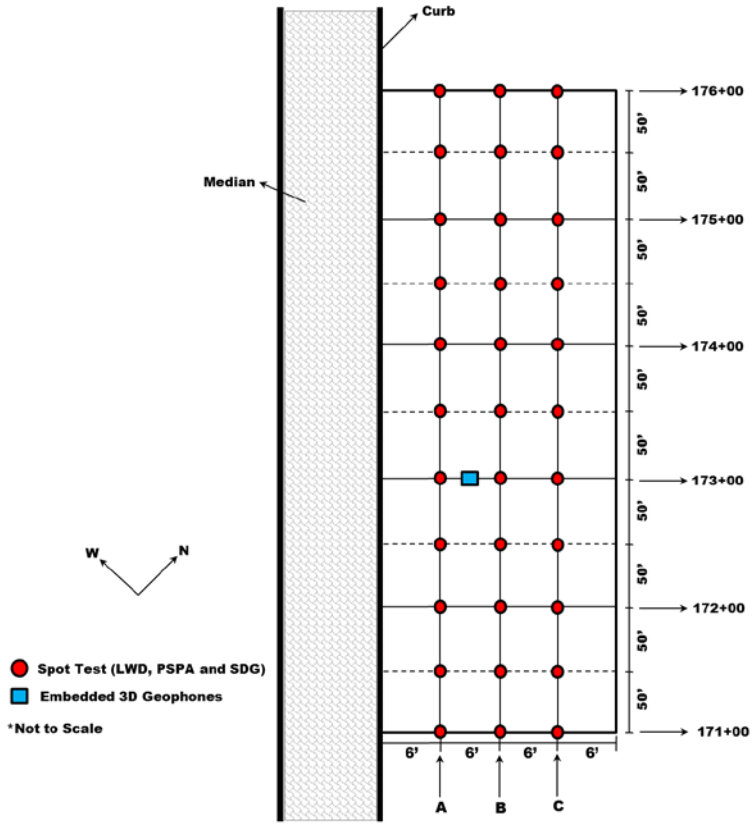

Figure A.1.4. Location of spot tests and geophones

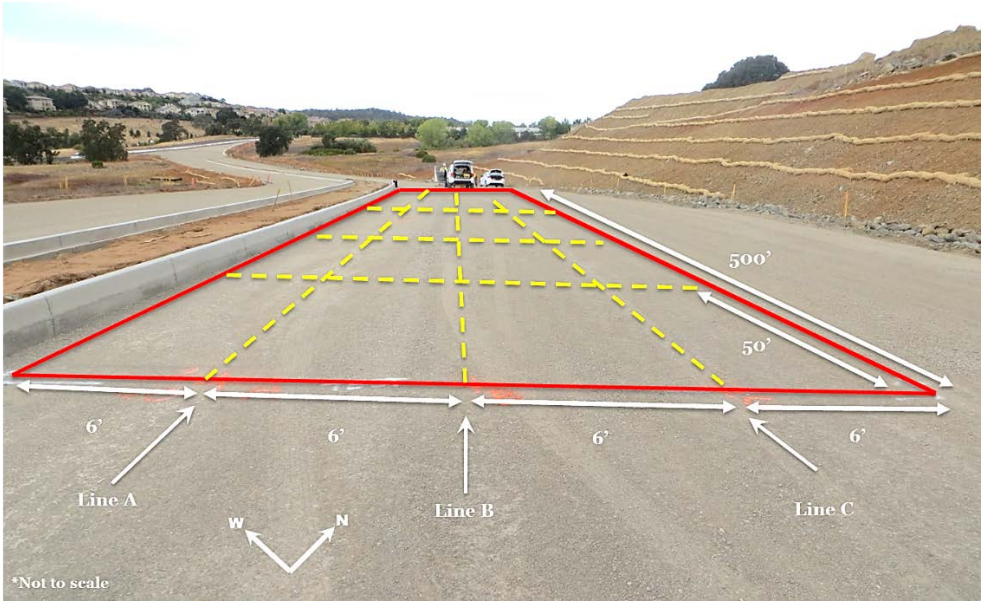

Figure A.1.5. Testing section and the test grid

To evaluate the data provided by the IC roller systems, a system-wide evaluation process was performed during field activities. As a part of this evaluation process, two 3-dimensional (3D) geophones were embedded at a specific location (see Figure A.1.4) at two different depths of 12 and 20 in. in the subgrade. A 30-ft-long trench was excavated to securely transfer the geophone cables through a PVC pipe to the shoulder.

Figures A.1.6 and A.1.7 illustrate the process of the LWD and PSPA spot tests on top of the compacted base layer.

Figure A.1.6. PSPA test

Figure A.1.7. LWD test

To facilitate the mapping of the test grid on the asphalt lifts, a Topcon local base station was setup to locate the coordinates of the test points (Figure A.1.8). Considering the geographical location of the job site, the Universal Transverse Mercator (UTM) zone 10 North (representing north hemisphere) was selected as the reference coordinates for the GPS data collection. Figure A.1.9 illustrates the location of the field testing site on the UTM map.

Figure A.1.8. Setting up the local base station

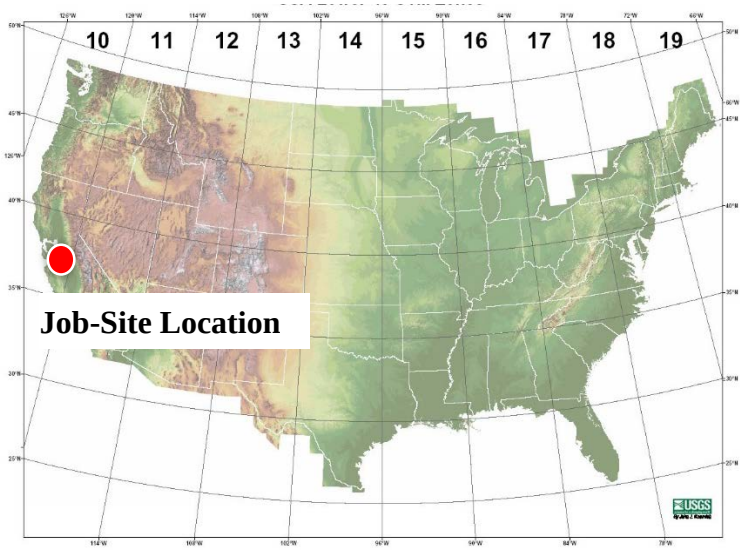

Figure A.1.9. The coordinate reference for the GPS devices

A.2. LABORATORY RESULTS

Index properties of the subgrade are summarized in Table A.2.1. The gradation curve of the subgrade materials is depicted in Figure A.2.1. This material was classified as GW as per USCS. The optimum moisture content and maximum dry unit weight obtained as per modified Proctor tests (AASHTO T99) are also reported in Table A.2.1.

Table A.2.1. Index Properties of Base Materials

Gradation %				USCS Class.	Specific Gravity	Moisture/Density	
Gravel	Coarse Sand	Fine Sand	Fines			Optimum Moisture Content, %	Maximum Dry Unit Weight, pcf
60	32	7	1	GW	2.65	9.0	129.8

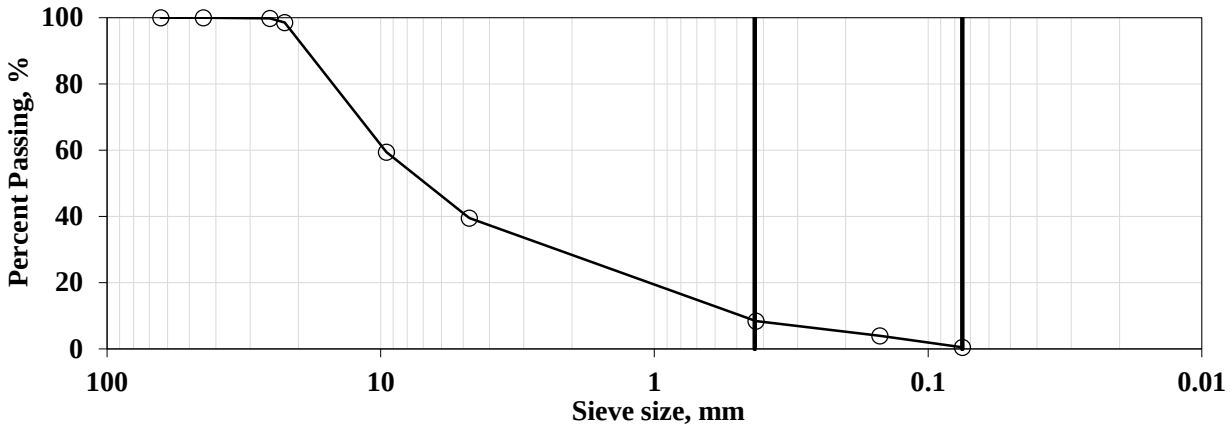

Figure A.2.1. Gradation curves of base geomaterials

Since the IC technology and modulus-based devices are based on measuring the stiffness of the layers, the resilient modulus (MR) and free-free resonant column (FFRC) tests were performed on laboratory specimens prepared at the optimum moisture content as summarized in Table A.2.2. It should be noted that the representative resilient modulus is calculated by replacing representative bulk stress and octahedral shear stress (recommended by NCHRP 1-28A) in the modified resilient modulus constitutive model (Nazarian et al. 2014).

Table A.2.2 - Laboratory Results of MR and FFRC Tests of Geomaterials

Site	Type	Target Moisture Content	Actual Moisture Content, %	Dry Density, pcf	FFRC Modulus, ksi	Representative Resilient Modulus, ksi
California	Base	9.0	8.8	130.0	60	23.1
California	Base	9.0	9.2	130.4	56	23.0

A.3. FIELD MODULUS/STIFFNESS MEASUREMENTS

Figures A.3.1 and A.3.2 summarize the results of the PSPA and LWD tests on the base layer. The reported modulus at each station is the average of three tests along lines A, B and C in Figure A.1.4. The error bars represent the spatial standard deviation among each three data points along lines A, B and C. LWD is a deflection-based device that imparts an impulse load to the surface of the compacted geomaterial and measures the surface deflection as a result of a composite stiffness of all layers. PSPA measures the low-strain elastic modulus of the surface layer through sending stress waves and colleting the response from the layer of interest. The LWD estimates a composite modulus of the layered system while PSPA gives the layer-specific stiffness properties. The depth of influence of the LWD is deeper than that of the PSPA. Due to the functional properties of the PSPA device, the standard deviation of the modulus measurements between test points is expectedly higher than the LWD. The overall trends of the modulus estimations show a fairly consistent base layer in terms of stiffness.

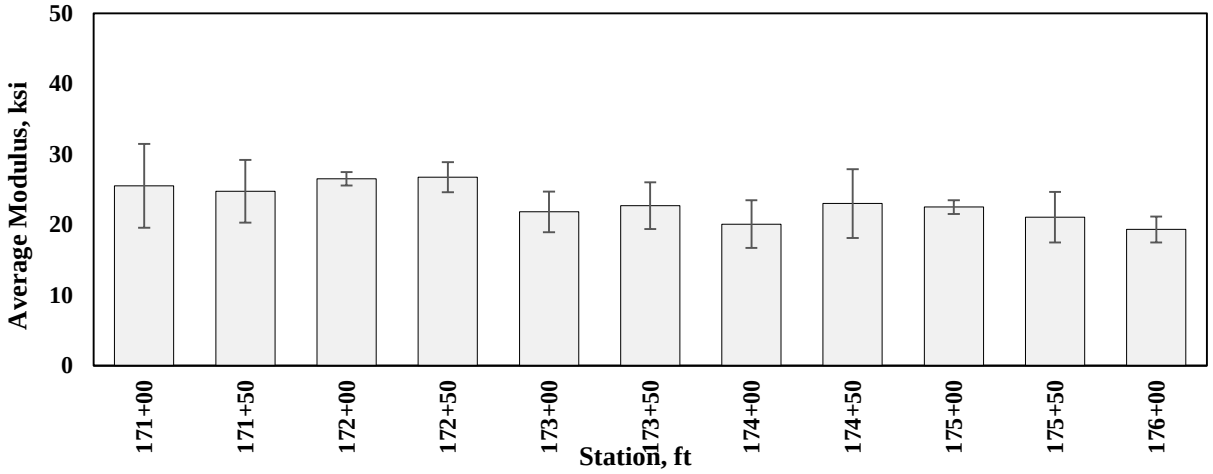

Figure A.3.1. Spatial variation of average LWD base modulus and standard deviation (as error bars)

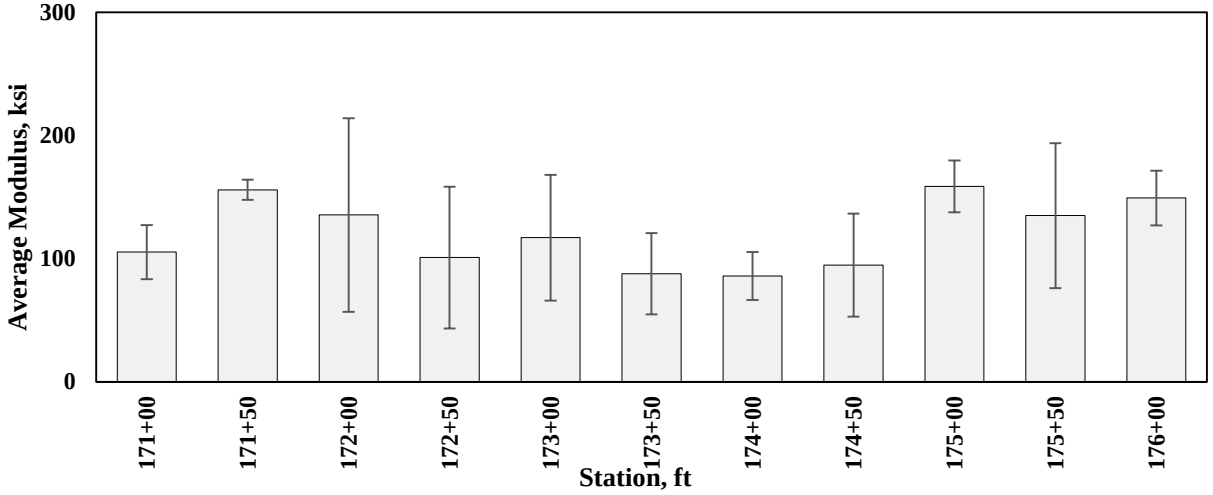

Figure A.3.2. Spatial variation of average PSPA base modulus and standard deviation (as error bars)

A.4. EVALUATION OF ASPHALT COMPACTION PROCESS

A nuclear density gauge (NDG) was employed to evaluate the density growth between the passes of the rollers. One test point within each lane-width was selected during the placement of HMA to monitor the density and temperature after each pass of the roller. For the first lift of the HMA, placed on Tuesday September 23, the HAMM, SAKAI and CAT rollers were selected for breakdown, intermediate and finishing processes, respectively. Figures A.4.1 through A.4.15 summarize the unit weight, compaction level and temperature between different passes of the rollers for each control point during the placement and compaction of the first and second HMA lifts. The unit weight and expectedly the compaction level increased as more passes of the rollers were applied. As a result of the cooling process, the temperature of the HMA lift decreased between the passes of the rollers.

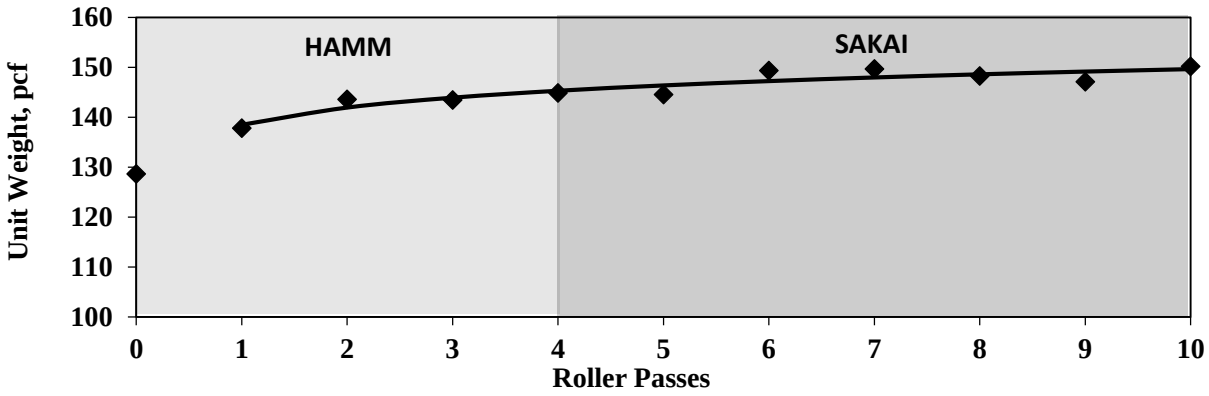

Figure A.4.1. Variation of unit weight between roller passes (first lift of HMA) – control point 1

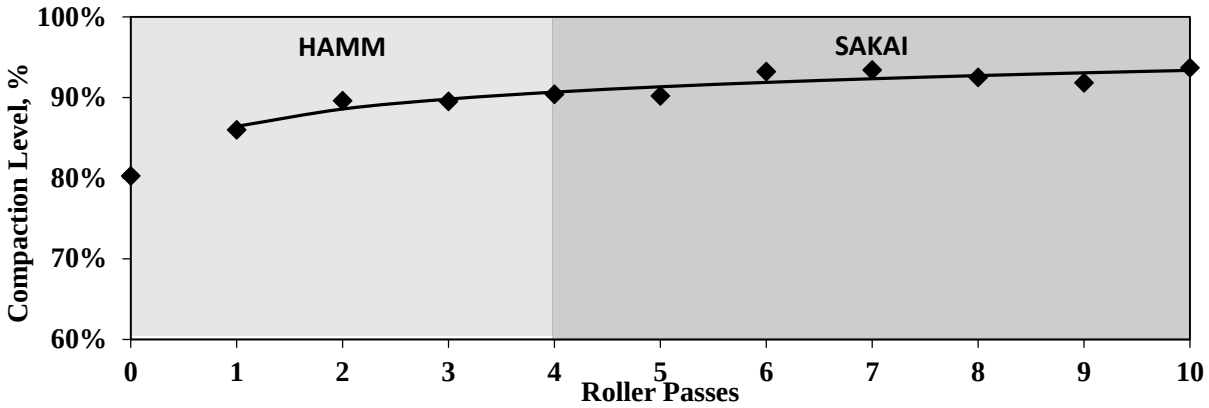

Figure A.4.2. Variation of compaction level between roller passes (first lift of HMA) – control point 1

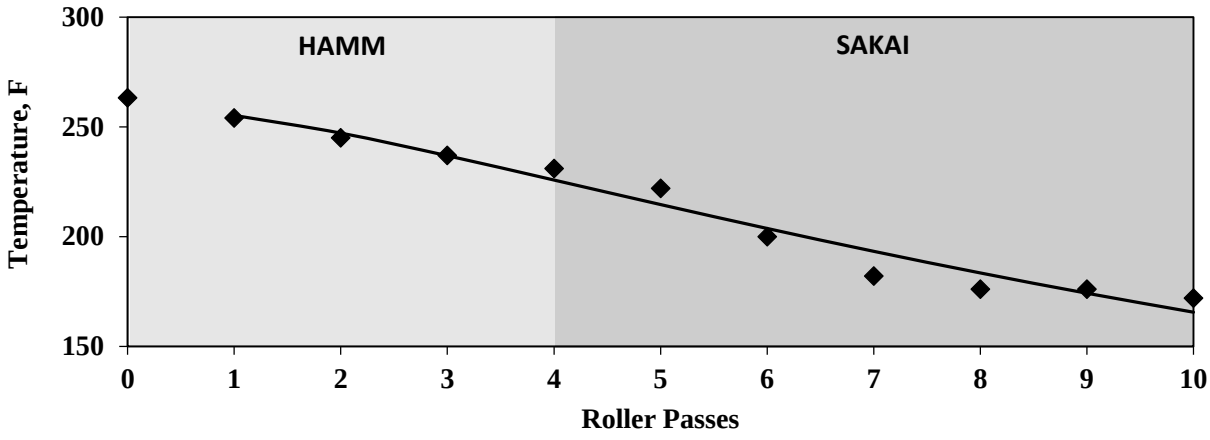

Figure A.4.3. Variation of temperature between roller passes (first lift of HMA) – control point 1

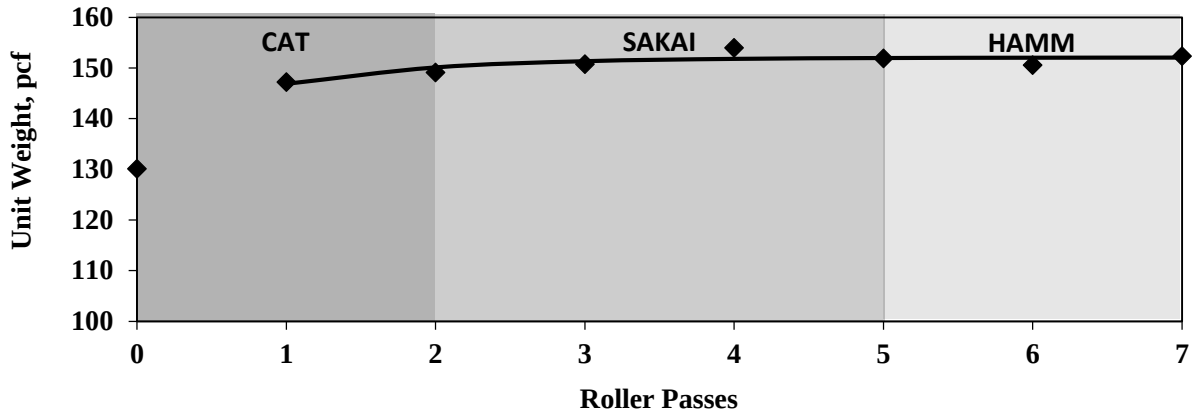

Figure A.4.4. Variation of unit weight between roller passes (second lift of HMA) – control point 1

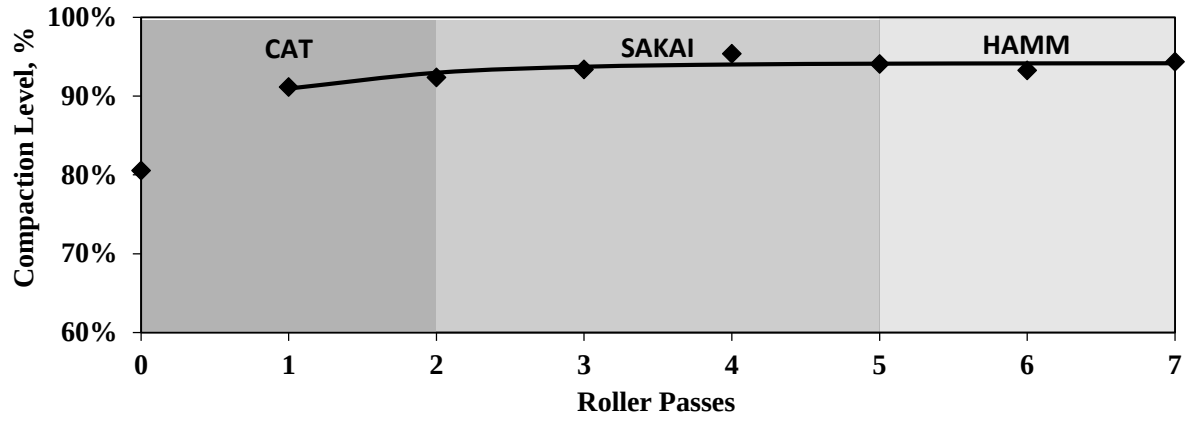

Figure A.4.5. Variation of compaction level between roller passes (second lift of HMA) – control point 1

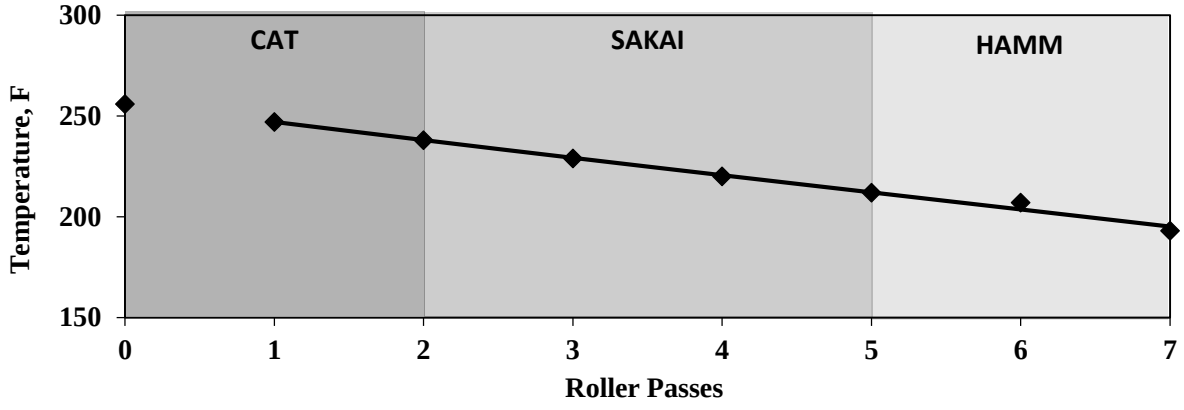

Figure A.4.6. Variation of temperature between roller passes (second lift of HMA) – control point 1

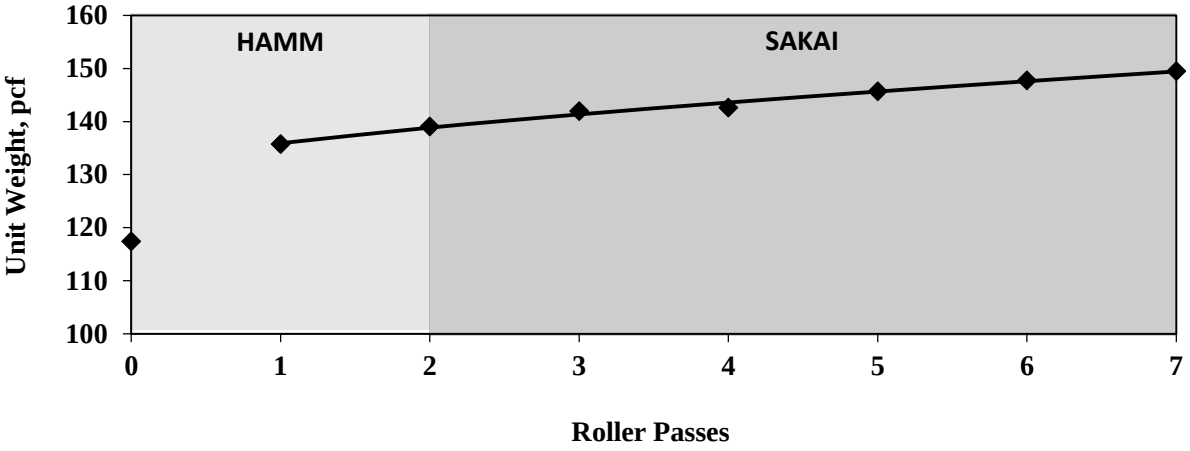

Figure A.4.7. Variation of unit weight between roller passes (first lift of HMA) – control point 2

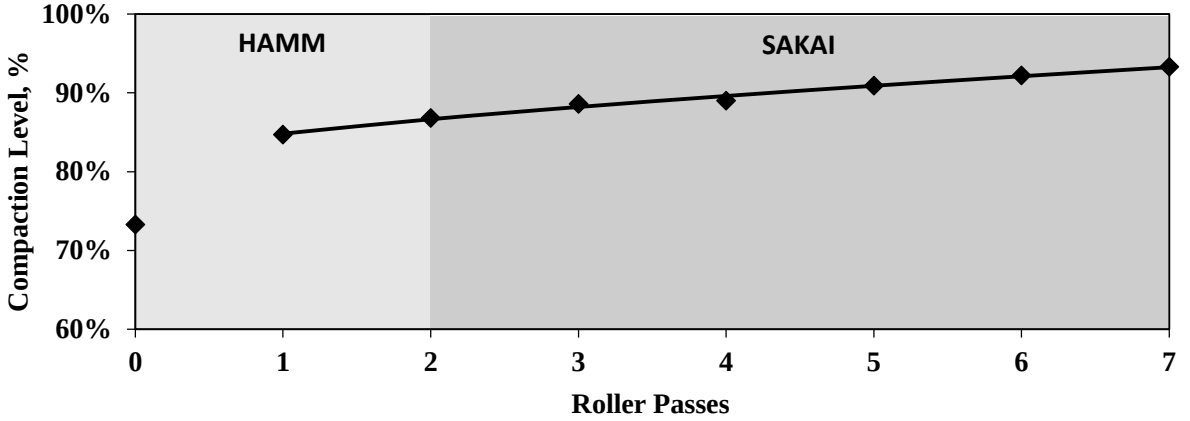

Figure A.4.8. Variation of compaction level between roller passes (first lift of HMA) – control point 2

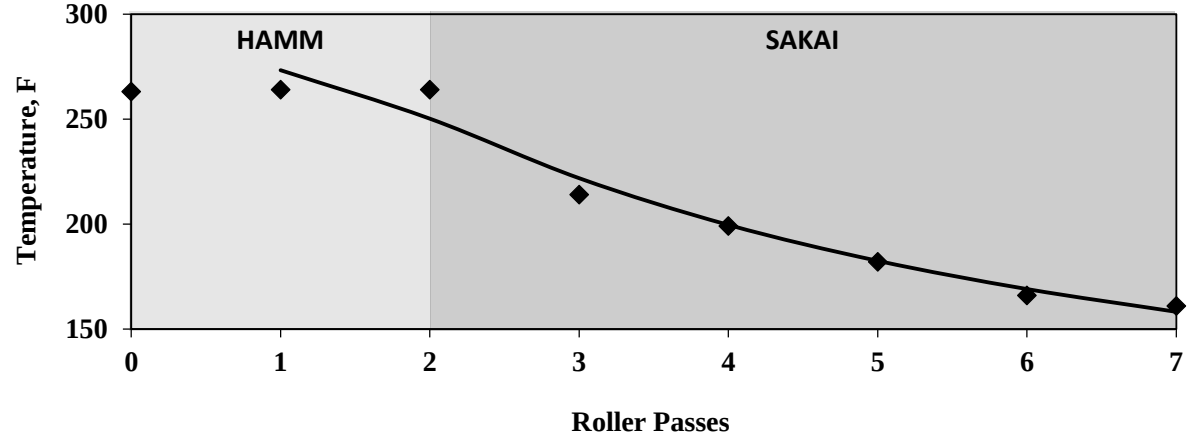

Figure A.4.9. Variation of temperature between roller passes (first lift of HMA) – control point 2

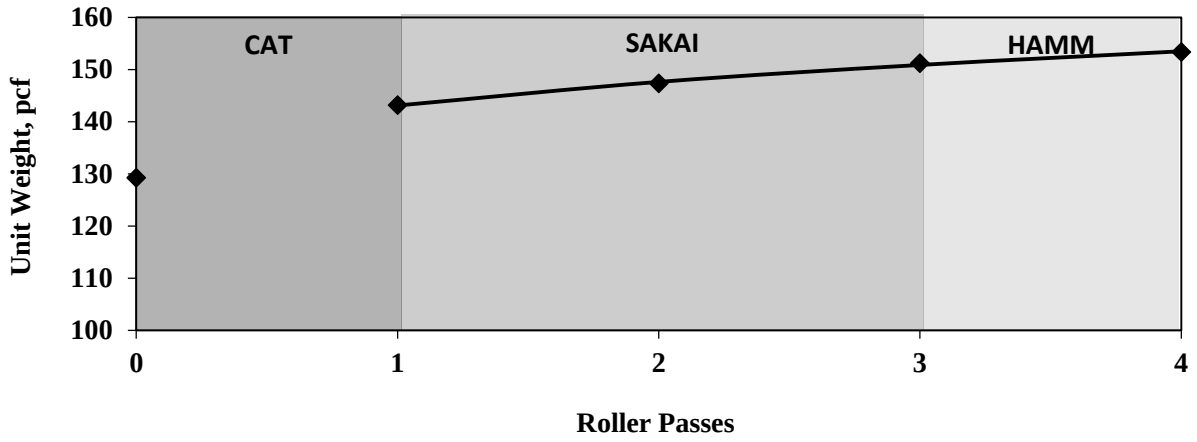

Figure A.4.10. Variation of unit weight between roller passes (second lift of HMA) – control point 2

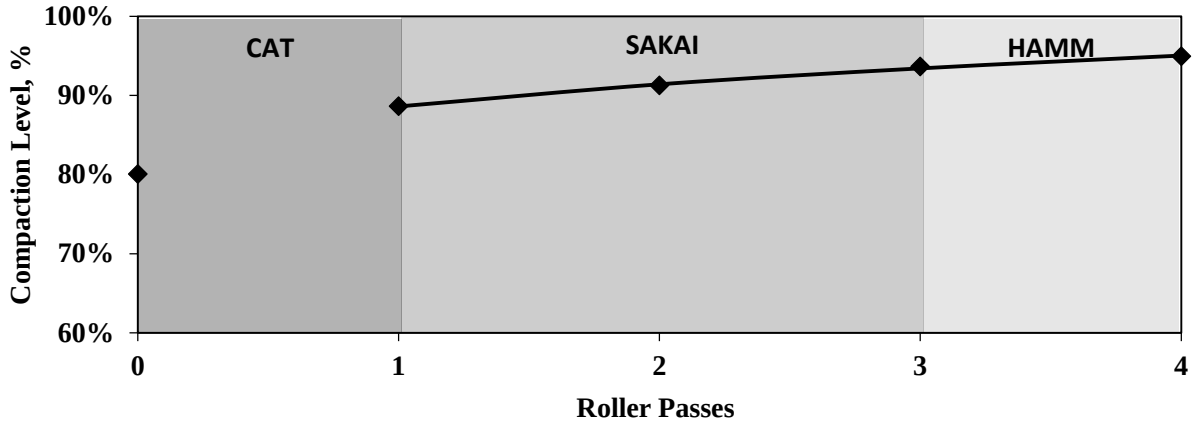

Figure A.4.11. Variation of compaction level between roller passes (second lift of HMA) – control point 2

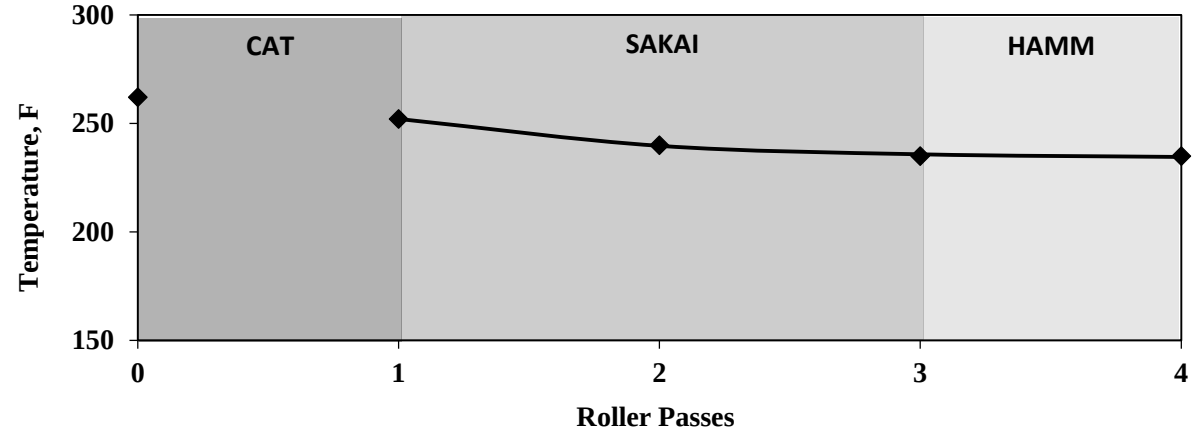

Figure A.4.12. Variation of temperature between roller passes (second lift of HMA) – control point 2

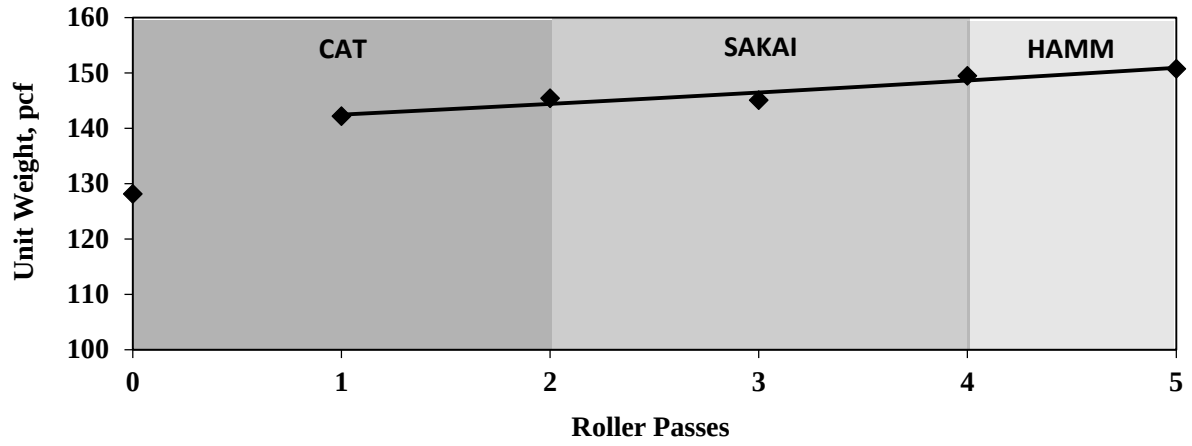

Figure A.4.13. Variation of unit weight between roller passes (second lift of HMA) – control point 3

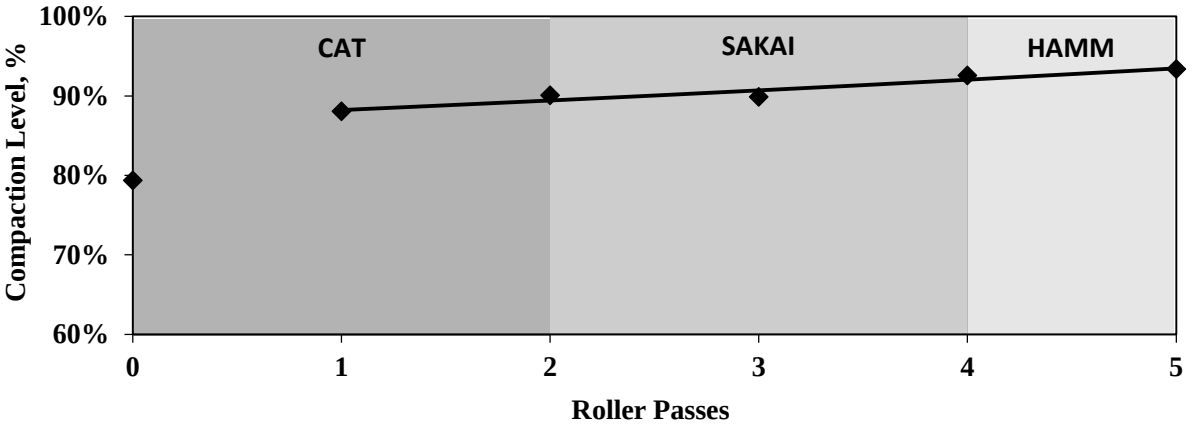

Figure A.4.14. Variation of compaction level between roller passes (second lift of HMA) – control point 3

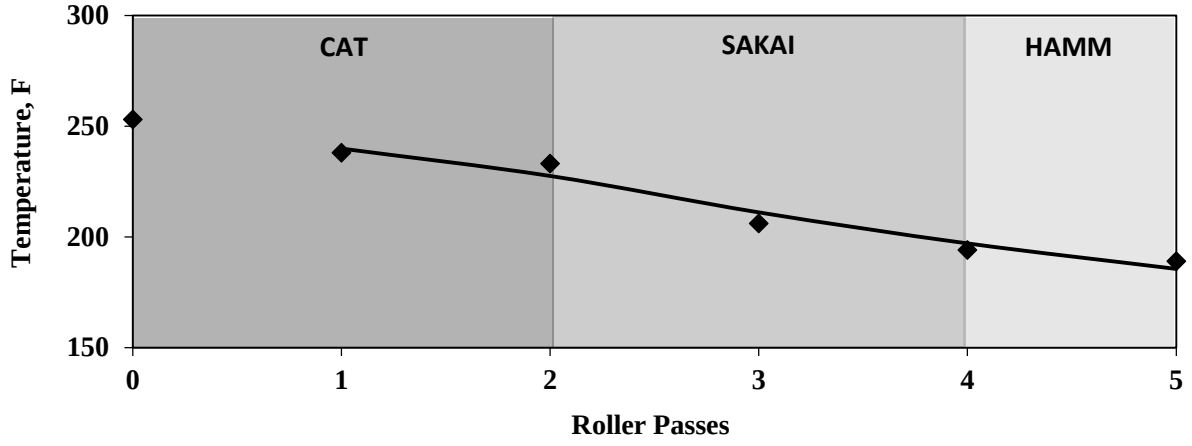

Figure A.4.15. Variation of temperature between roller passes (second lift of HMA) – control point 3

A.5. INTELLIGENT COMPACTION DATA COLLECTION AND ANALYSIS

Table A.5.1 summarizes the vibration settings that were used during the data collection process from the buried 3D geophones and accelerometers mounted on the rollers. Two sets of vibration tests were performed to collect the IC data with the three (retrofit, OEM and UTEP) systems on each roller. To study the effect of different vibration settings, the stationary vibration tests (Figure A.5.1) were carried out at different frequencies and amplitudes. The vibration response of the embedded geophones were collected as well as the vibration data from the mounted accelerometers to evaluate the performance of the retrofit system, to study the response of the soil layers, and to quantify the influence depth of the roller vibrations.

Table A.5.1. Different vibration settings used during mapping of the base layer (data collected both from buried 3D geophones and mounted accelerometers)

Roller	HAMM		CAT[2]		SAKAI	
	Frequency (vpm[1])	Amplitude	Frequency (vpm)	Amplitude	Frequency (vpm)	Amplitude
Stationary Vibration	1500	Low	Low	Low	2500	Low
	2500		High	Low	3000	
	4000		Low	High	4000	
	1500	High	High	High	2500	High
	2500				3000	
Moving Vibration	1500	Low	The research team were unable to mount the accelerometers on CAT roller		2500	Low
	4000				3000	
	1500	High			2500	High

[1]vibration per minute, [2]The CAT roller had two options (low and high) for frequency settings

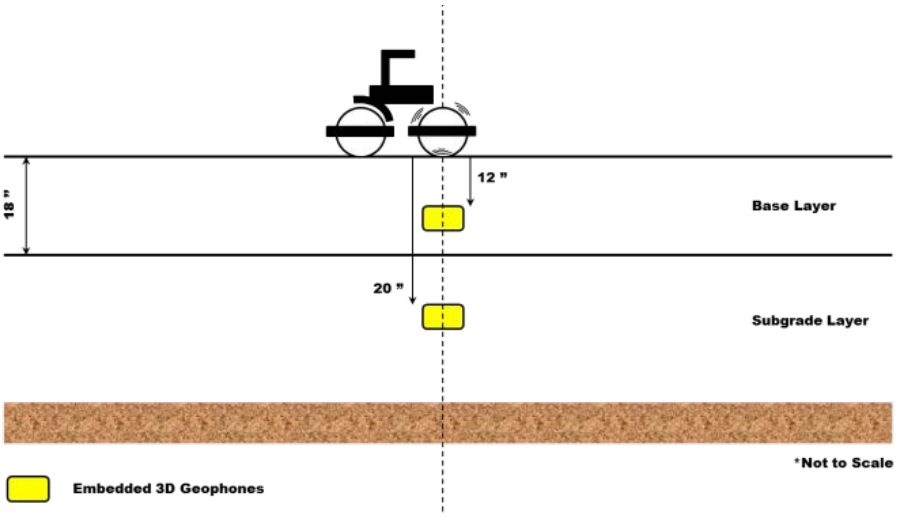

Figure A.5.1. Stationary vibration on top of embedded geophones at different vibration settings

Figure A.5.2 illustrates the second set of vibration tests (moving vibration) that resembles the actual compaction process. To study the impact of the roller position on the response of the materials, the roller started vibrating from 100 ft before to 100 ft after the location of the embedded sensors. Furthermore, the drum position was set at different transversal offsets from the position of ground sensors to study the transversal influence distance during stationary vibration (see Figure 3.2.4 of Chapter 3.

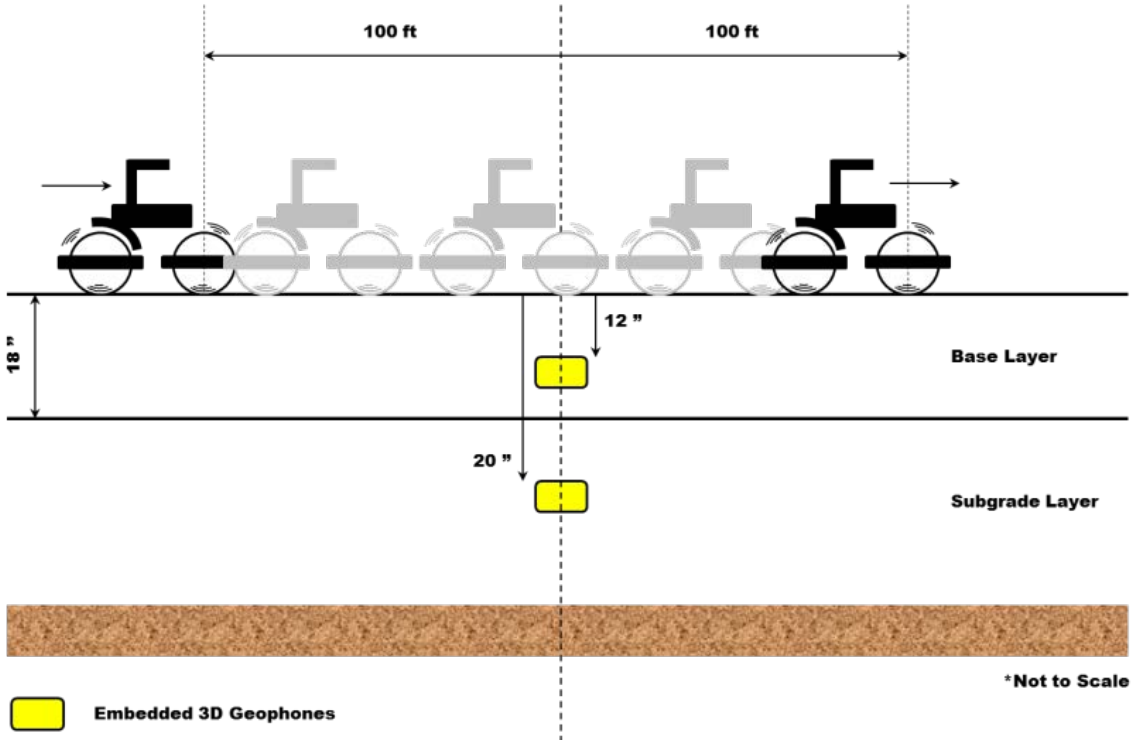

Figure A.5.2. Moving vibration along the designated section of the test pad

Figures A.5.3 to A.5.8 summarize the activities performed during IC data collection in this rodeo.

Figure A.5.3. Caterpillar roller

Figure A.5.4. HAMM roller

Figure A.5.5. SAKAI roller

Figure A.5.6. Data collection during stationary vibration

Figure A.5.7. Mounted accelerometer on the roller

Figure A.5.8. Pre-mapping of the base layer

A.6. PRESENTATION OF IC DATA

A.6.1. Pre-Mapping of Base Layer

The spatial variations of the IC measurement values (ICMVs) for the three rollers during the pre-mapping of the base layer were established first. To generate the colormaps, the IC data were selected within the boundaries of the test section as illustrated in Figure A.1.4. Any nonnumeric and zero values in the ICMV data were identified and removed from the data file. The Bayesian Empirical Krigging method was employed to interpolate the filtered IC data and generate the data for colormaps. The standard Quantile method (in which each class contains an equal number of features) was used to classify the valid ICMVs into three classes (red, yellow and green). The same classification method was used for all colormaps for ease in visual comparison.

The IC data from the two retrofit systems installed on the SAKAI and HAMM rollers are compared with the IC data collected by the CAT OEM system in Figures A.6.1 through A.6.3.

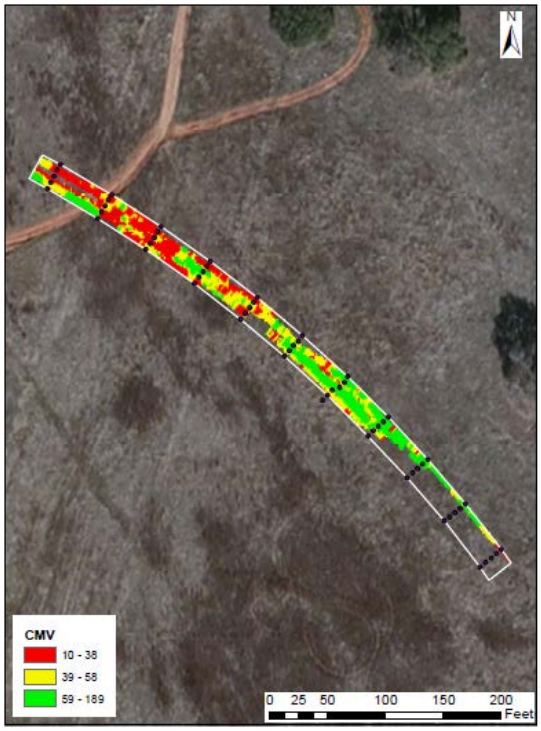

Figure A.6.1. Spatial variation of CMV data from HAMM retrofit system during pre-mapping

Figure A.6.2. Spatial variation of CMV data from SAKAI retrofit system during pre-mapping

Figure A.6.3. Spatial variation of CMV data from CAT system during pre-mapping

The distributions of the CMVs during pre-mapping from the three systems are summarized in Figures A.6.4 through A.6.6.

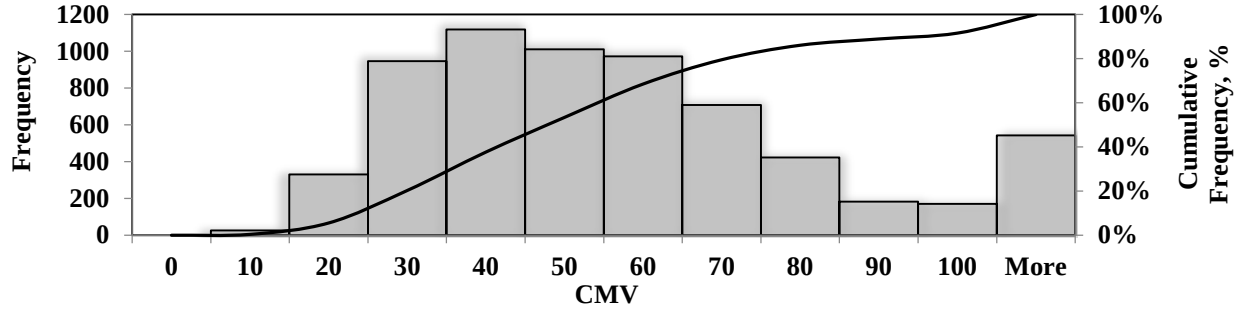

Figure A.6.4. Distribution of CMV data from HAMM retrofit system during pre-mapping of base layer

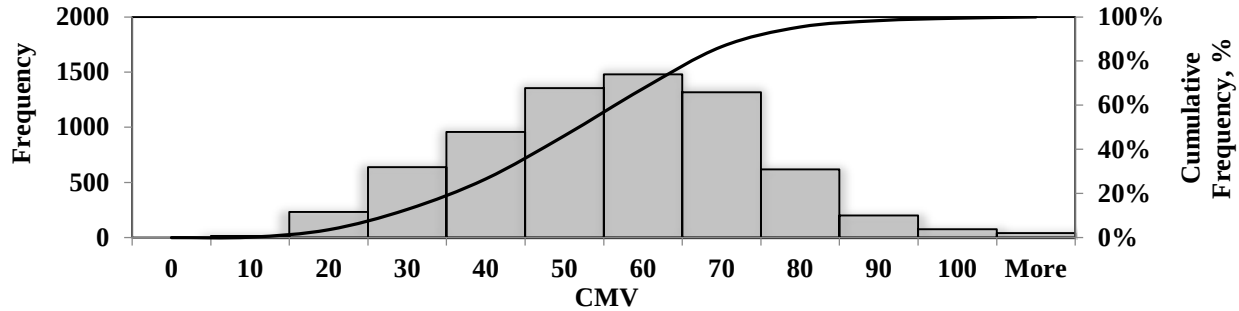

Figure A.6.5. Distribution of CMV data from SAKAI retrofit system during pre-mapping of base layer

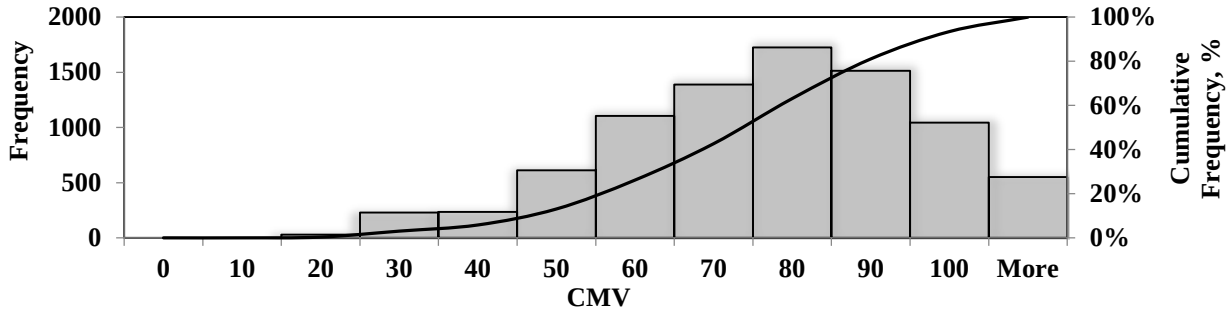

Figure A.6.6. Distribution of CMV data from CAT system during pre-mapping of base layer

The colormaps of the ICMVs from the OEM and retrofit systems on the HAMM roller are compared in Figures A.6.7 and A.6.8.

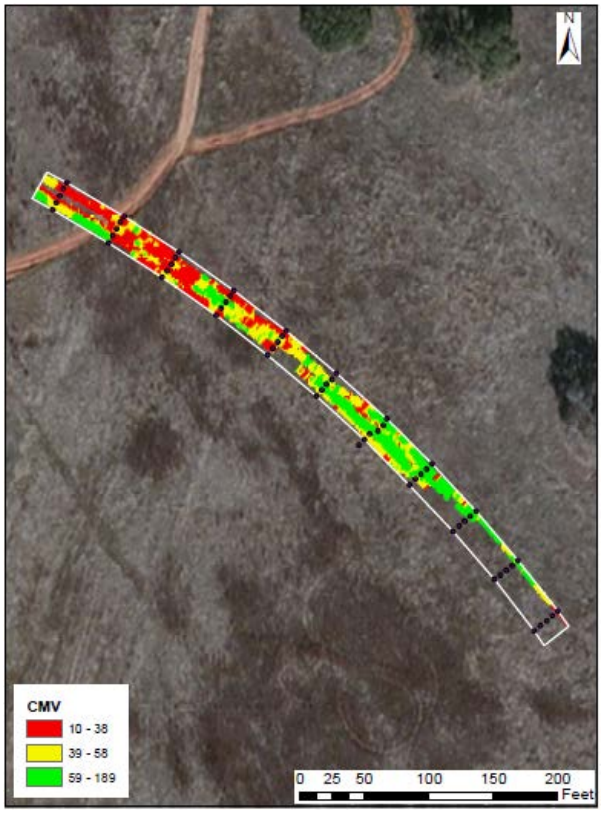

Figure A.6.7. Spatial variation of CMV data from HAMM retrofit system during pre-mapping

Figure A.6.8. Spatial variation of CMV data from HAMM OEM system during pre-mapping

Figures A.6.9 and A.6.10 further reflect the differences in the HMVs and CMVs from the HAMM roller during pre-mapping.

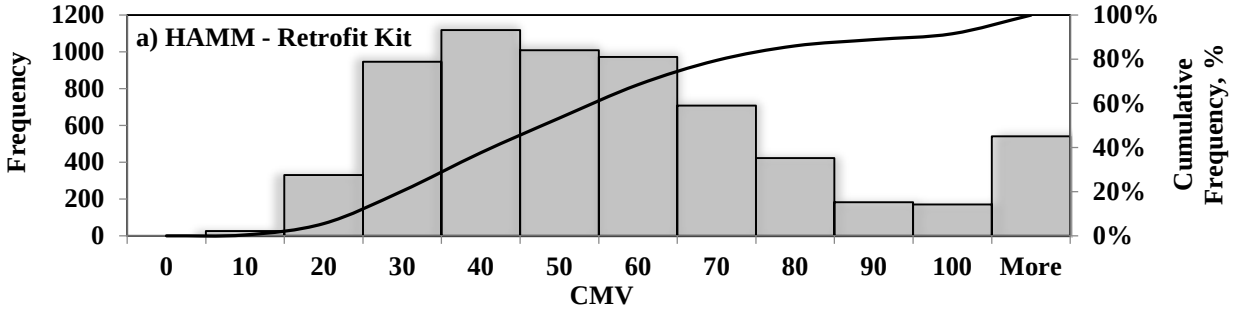

Figure A.6.9. Distribution of CMV data from HAMM retrofit system during pre-mapping

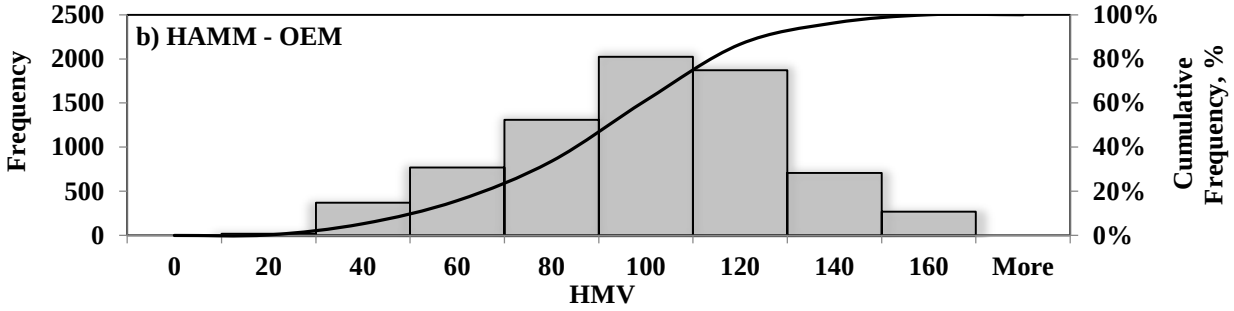

Figure A.6.10. Distribution of CMV data from HAMM OEM system during pre-mapping

As previously illustrated in Figures A.6.1 through A.6.3, the coverage areas by different systems were different. Therefore, the common coverage area among the three rollers is illustrated in Figure A.6.11.

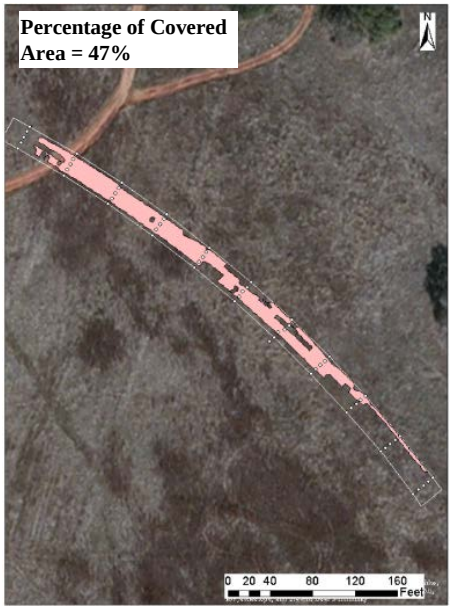

Figure A.6.11. Common coverage area among two retrofit systems on HAMM and SAKAI and CAT system during pre-mapping

Figures A.6.12 through A.6.14 compare the distributions of the CMVs between the two retrofit systems mounted on the SAKAI and HAMM rollers and the OEM system on the CAT roller within the common coverage area.

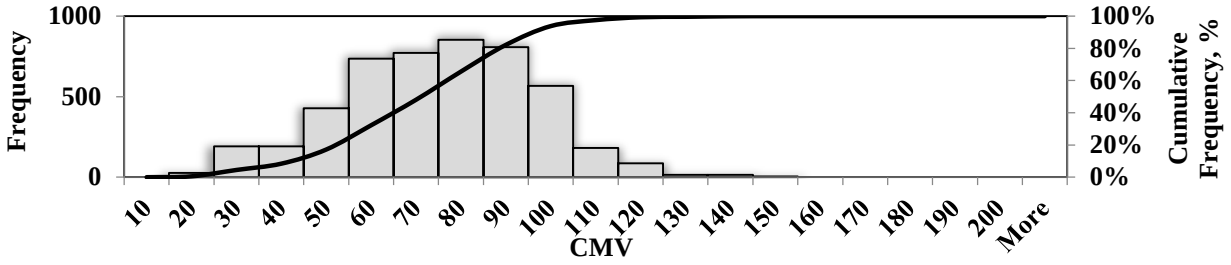

Figure A.6.12. Distribution of CMV data for the common coverage area between rollers during pre-mapping - CAT

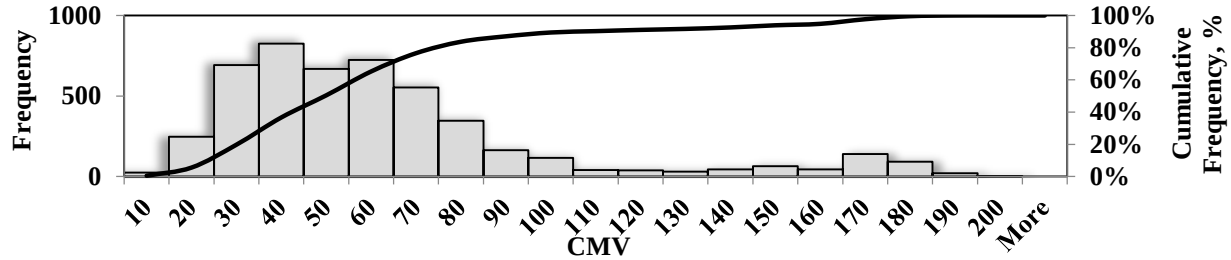

Figure A.6.13. Distribution of CMV data for the common coverage area between rollers during pre-mapping – retrofit system on HAMM

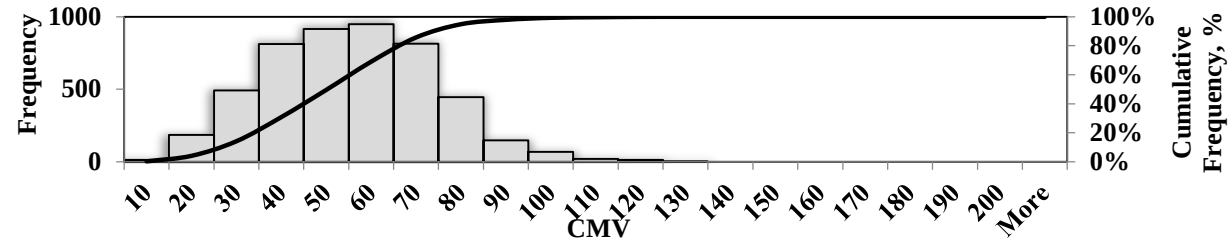

Figure A.6.14. Distribution of CMV data for the common coverage area between rollers during pre-mapping – retrofit system on SAKAI

Figures A.6.15 and A.6.16 compare the averages and coefficients of variation (COV) of the CMVs from the three systems during the pre-mapping of the base layer on the common coverage area.

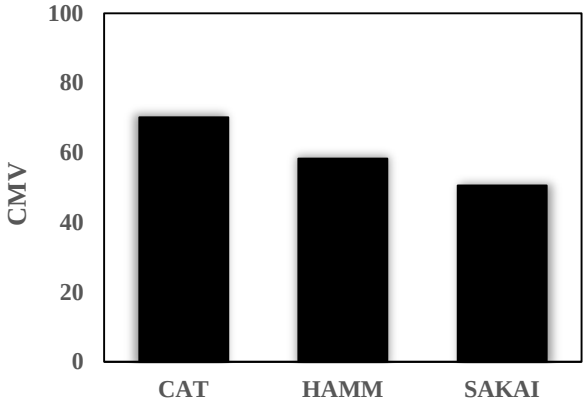

Figure A.6.15. Average CMV values of three rollers during pre-mapping

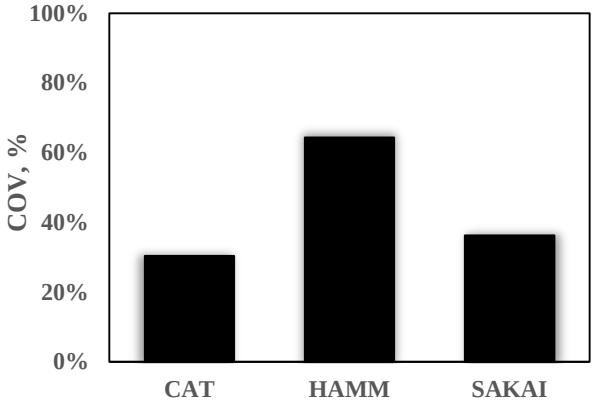

Figure A.6.16. Coefficients of variation of CMV values of three rollers during pre-mapping

The variations of the vibration frequency and amplitude of the rollers are summarized in Figures A.6.17 through A.6.20.

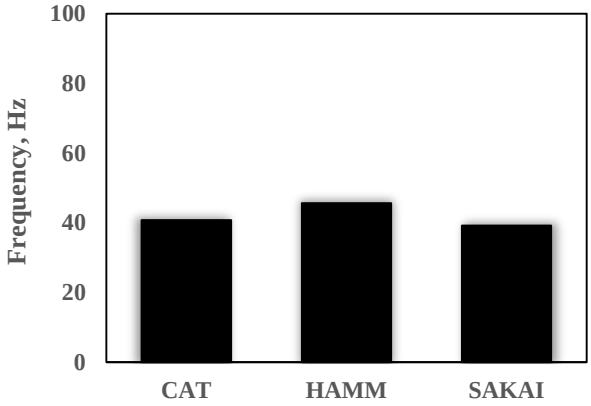

Figure A.6.17. Average of vibration frequency between three rollers during pre-mapping (for common coverage area)

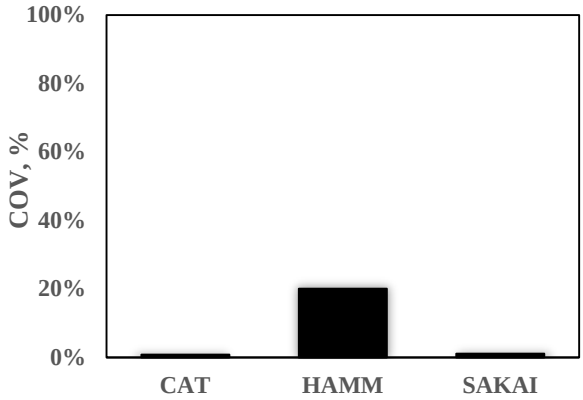

Figure A.6.18. Coefficient of variation of vibration frequency between three rollers during pre-mapping (for common coverage area)

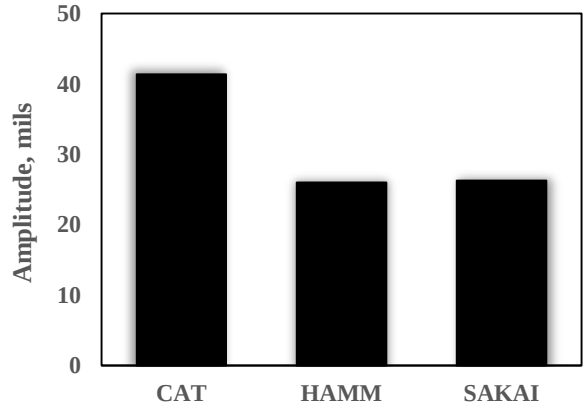

Figure A.6.19. Average of vibration amplitude between three rollers during pre-mapping (for common coverage area)

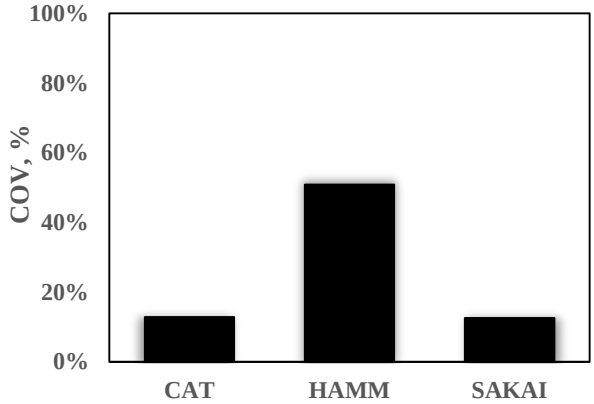

Figure A.6.20. Coefficient of variation of vibration amplitude between three rollers during pre-mapping (for common coverage area)

A.6.2. Compaction of First HMA Lift

As discussed in Section A.4, the HAMM and SAKAI rollers were selected as breakdown and intermediate rollers while the CAT roller was used as the finishing roller. Figures A.6.24 and A.6.25 illustrate the spatial distributions of the CMVs from the two retrofit systems on the HAMM and SAKAI rollers.

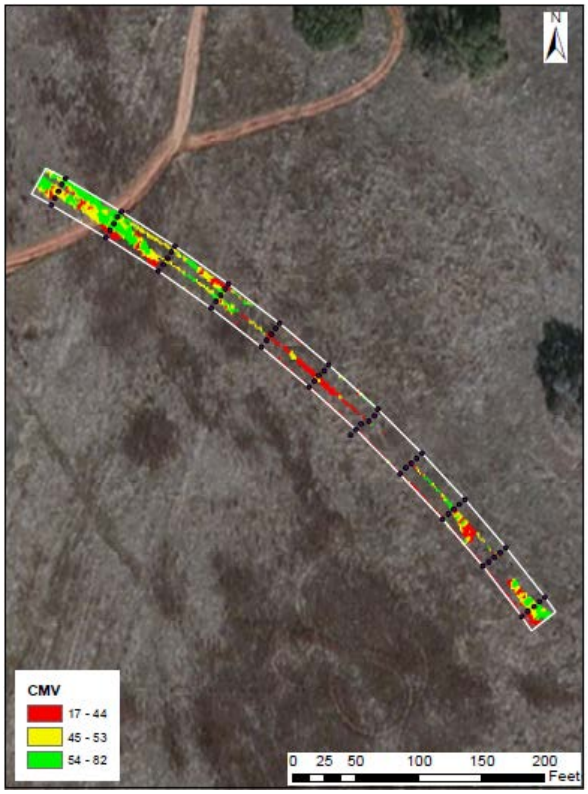

Figure A.6.24. Spatial variation of CMV data from HAMM retrofit system during compaction of first HMA lift

Figure A.6.25. Spatial variation of CMV data from SAKAI retrofit system during compaction of first HMA lift

Figures A.6.26 and A.6.27 compare the distributions of the CMVs from the two retrofit systems during the compaction process.

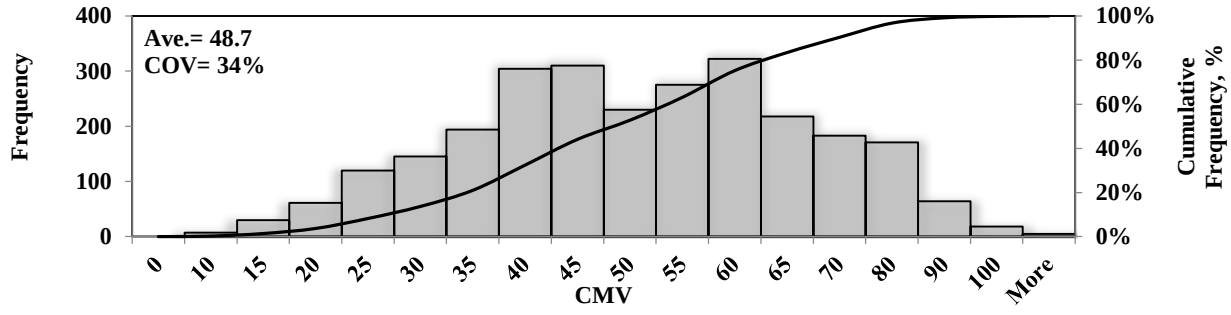

Figure A.6.26. Distribution of CMV data from retrofit system on HAMM during compaction of first HMA lift

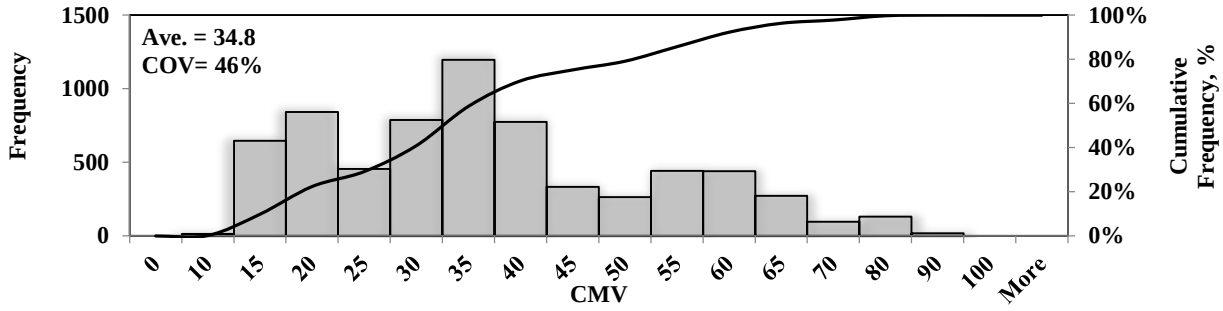

Figure A.6.27. Distribution of CMV data from retrofit system on SAKAI during compaction of first HMA lift

Figures A.6.28 and A.6.29 compare ICMVs from the retrofit and OEM systems on the HAMM roller. Due to some functional difficulties of the retrofit system, only partial data are available for that compaction process.

Figure A.6.28. Spatial variation of CMV data from retrofit system on HAMM during compaction of first HMA lift

Figure A.6.29. Spatial variation of HMV data from OEM system on HAMM during compaction of first HMA lift

Figures A.6.32 and A.6.33 summarize the comparison of the OEM and retrofit systems for the SAKAI roller during compaction of the first HMA lift. Figures A.6.34 and A.6.35 illustrate the distributions of the CMV and CCV data during the compaction of the first HMA lift.

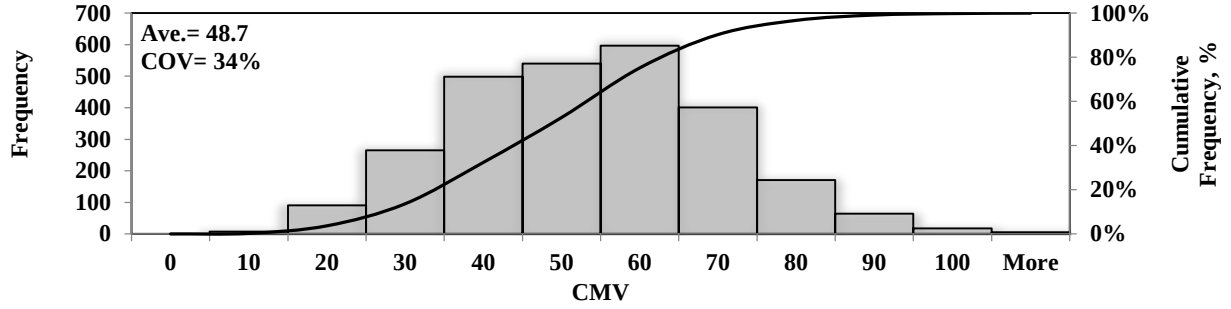

Figure A.6.30. Distribution CMV data from retrofit system on HAMM during compaction of first HMA lift

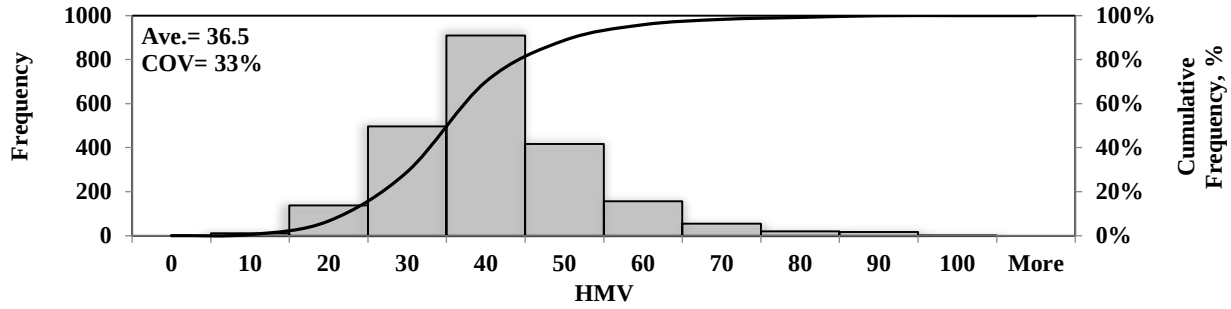

Figure A.6.31. Distribution HMV data from OEM system on HAMM during compaction of first HMA lift

Figure A.6.32. Spatial variation of CCV data from OEM system on SAKAI during compaction of first HMA lift

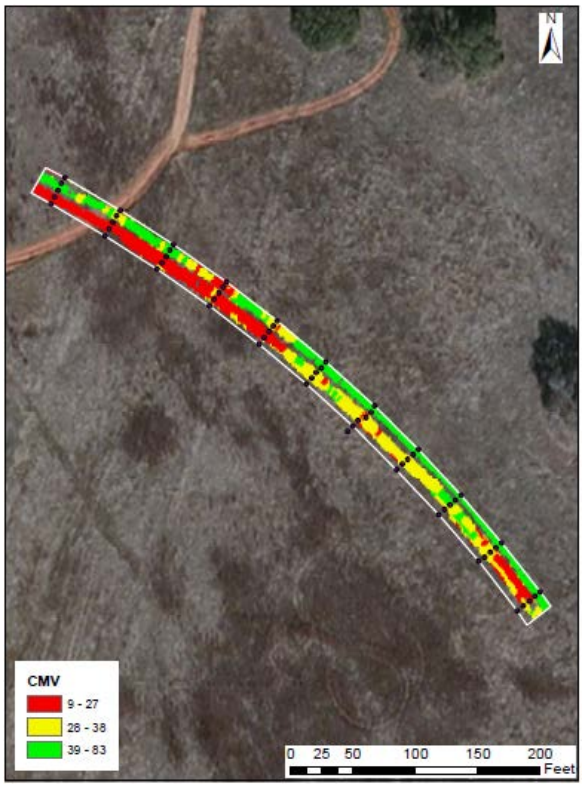

Figure A.6.33. Spatial variation of CMV data from retrofit system on SAKAI during compaction of first HMA lift

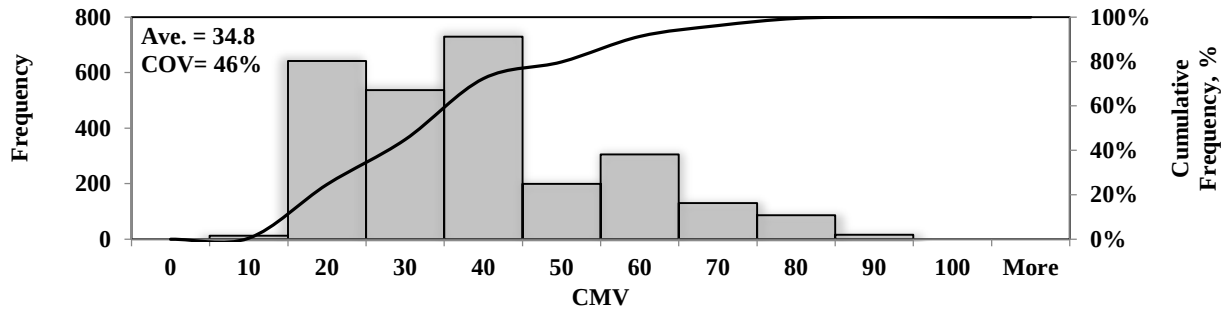

Figure A.6.34. Distribution CMV data from retrofit system on SAKAI during compaction of first HMA lift

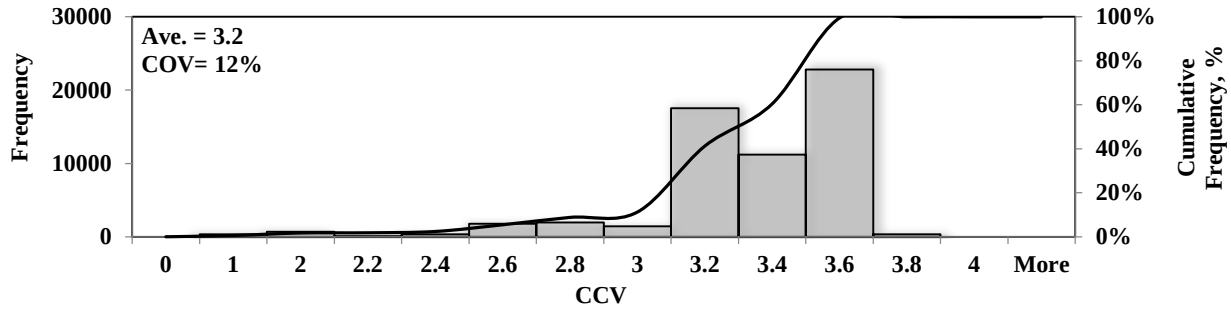

Figure A.6.35. Distribution CCV data from OEM system on SAKAI during compaction of first HMA lift

A.6.3. Compaction of Second HMA Lift

For the second HMA lift, the CAT roller was employed for the breakdown process and the SAKAI roller as the intermediate compactor. Figure A.6.36 and A.6.37 illustrate the spatial distributions of the CMV data from the CAT roller and the retrofit system on the SAKAI roller during the compaction of the second HMA lift.

Figure A.6.36. Spatial variation of CMV data from CAT roller during compaction of second HMA lift

Figure A.6.37. Spatial variation of CMV data from retrofit system on SAKAI during compaction of second HMA lift

The CMV data are summarized in Figures A.6.38 and A.6.39 in terms of the distributions of the CMVs.

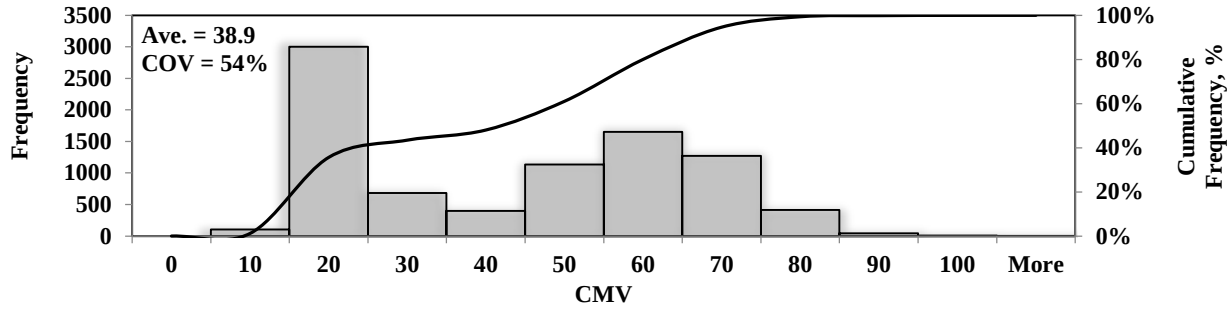

Figure A.6.38. Distribution of CMV data from CAT during compaction of second HMA lift

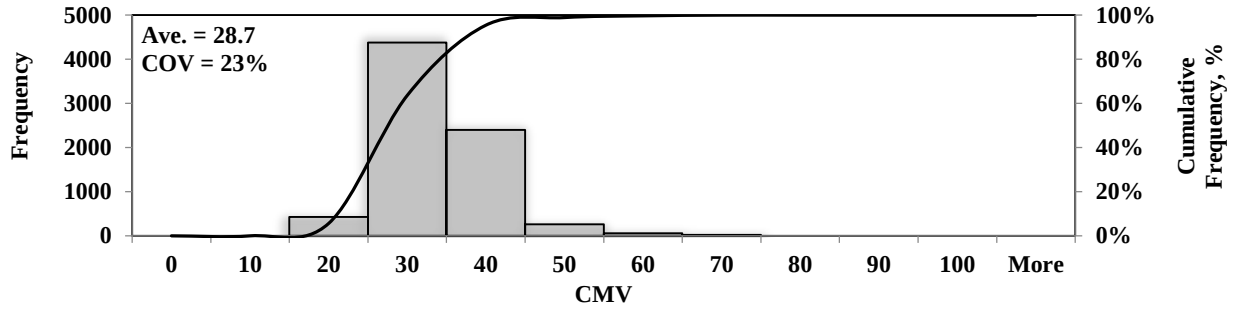

Figure A.6.39. Distribution of CMV data from retrofit system on SAKAI during compaction of second HMA lift

The IC data collected with the OEM and retrofit systems on the SAKAI roller during compaction of the second HMA lift are illustrated in Figures A.6.40 and A.6.41.

Figure A.6.40. Spatial variation of CMV data from retrofit system on SAKAI roller during compaction of second HMA lift

Figure A.6.41. Spatial variation of CMV data from OEM system on SAKAI during compaction of second HMA lift

Figures A.6.42 and A.6.43 reveal that the differences between the OEM and retrofit systems on the SAKAI roller during the compaction process.

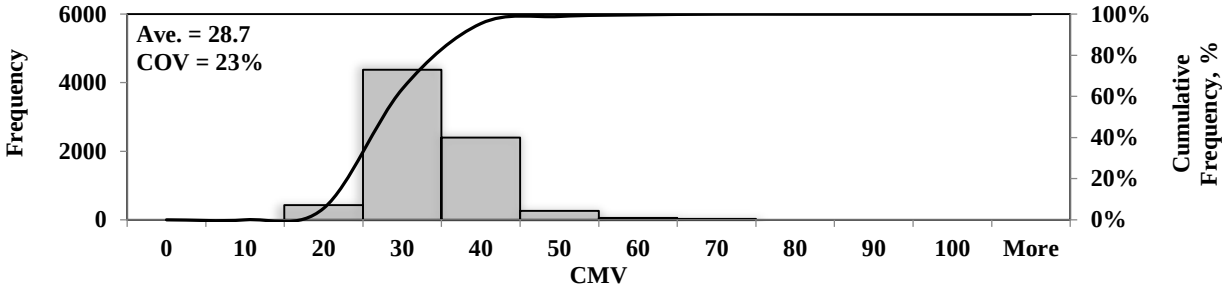

Figure A.6.42. Distribution of CMV data from retrofit system on SAKAI during compaction of second HMA lift

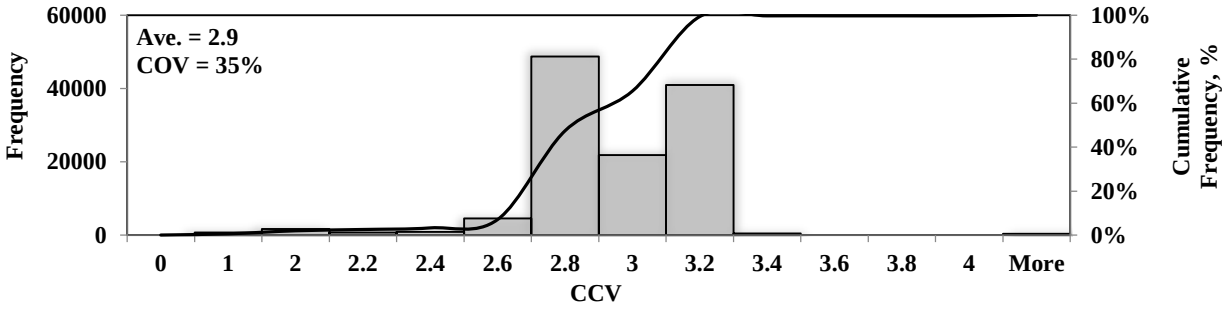

Figure A.6.43. Distribution of CCV data from SAKAI OEM system during compaction of second HMA lift

A.6.4. Analysis of IC Data using Veda®

Veda® is the software package for managing and interpreting IC data. Figures A.6.44 through A.6.47 show the distributions of the CMV data using Veda from the final coverage of the three rollers during the pre-mapping of the base layer. The SAKAI OEM data was not collected due to functional difficulties associated with that system on that day. Further statistical analyses are available through Veda as illustrated in Figures A.6.48 (the histogram of CMVs) and A.6.49 (the semivariogram of collected IC data).

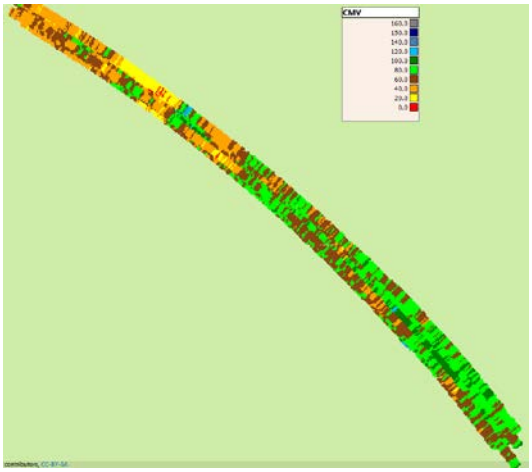

Figure A.6.44. Spatial variation of CMV data from CAT roller during pre-mapping of base layer

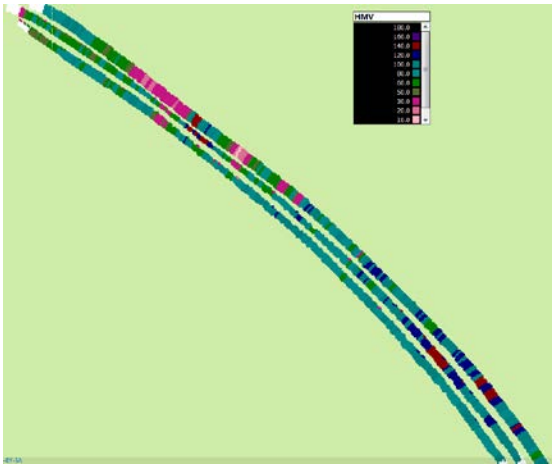

Figure A.6.45. Spatial variation of CMV data from OEM system on HAMM roller during pre-mapping of base layer

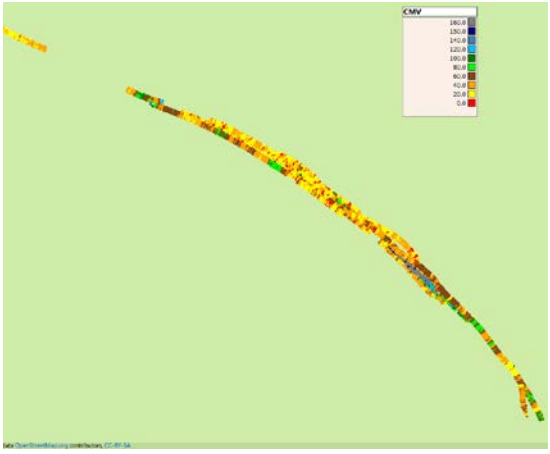

Figure A.6.46. Spatial variation of CMV data from retrofit system on HAMM roller during pre-mapping of base layer

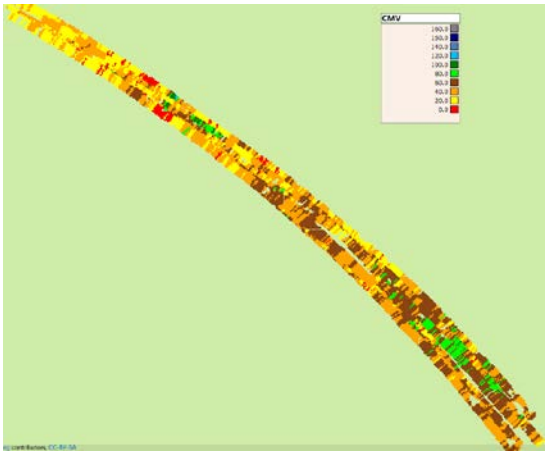

Figure A.6.47. Spatial variation of CMV data from retrofit system on SAKAI roller during pre-mapping of base layer

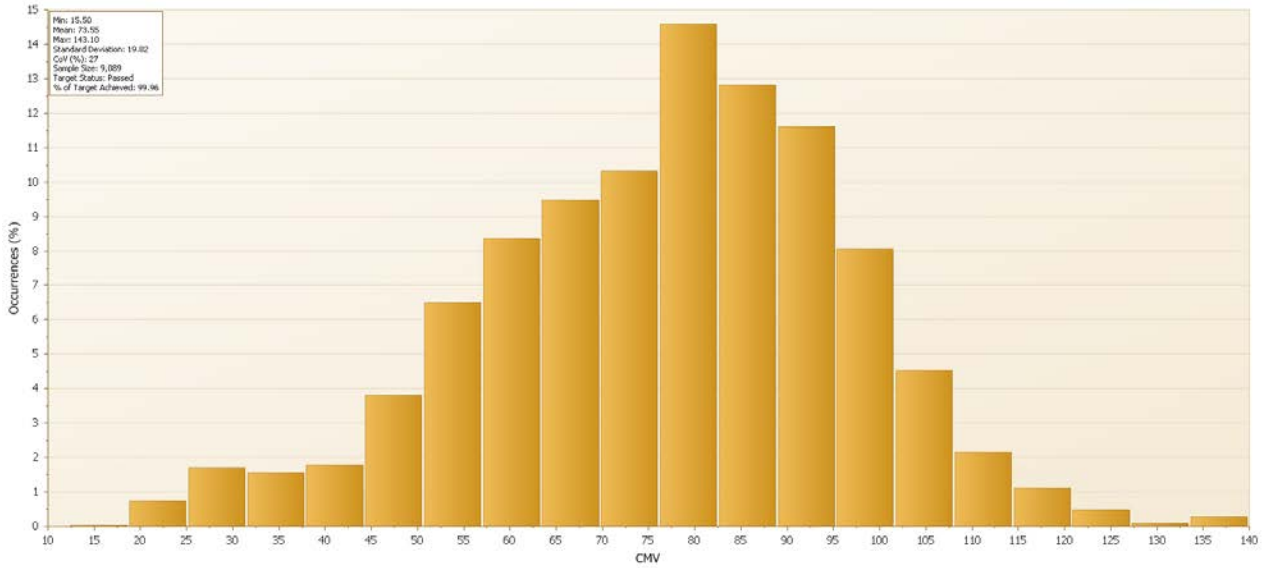

Figure A.6.48. Histogram of CMV data from Veda

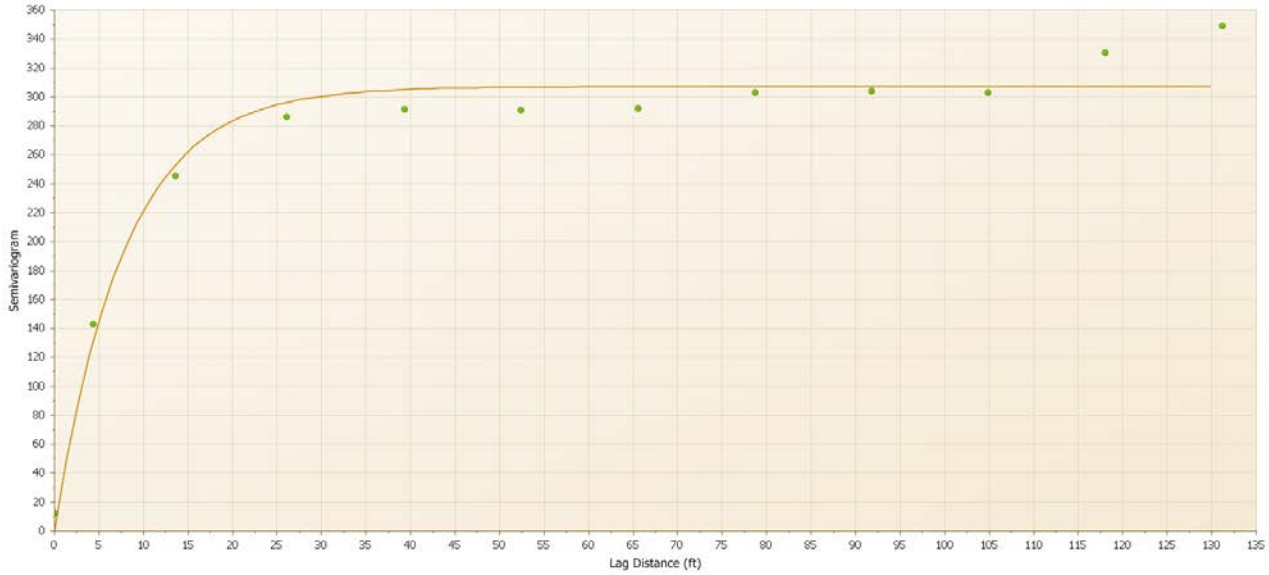

Figure A.6.49. Semivariogram of collected IC data from Veda

A.6.5. Correlation of IC Data and Spot Tests

Figures A.6.50 and A.6.51 summarize the CMV data from the CAT roller with the PSPA and LWD moduli.

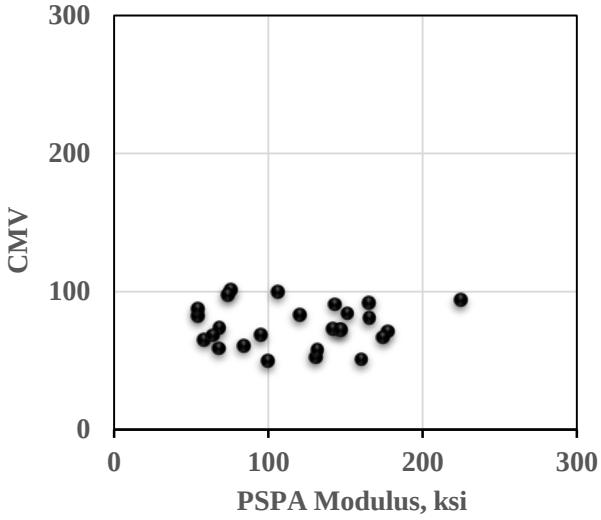

Figure A.6.50. Correlation of CMVs from CAT roller with PSPA moduli

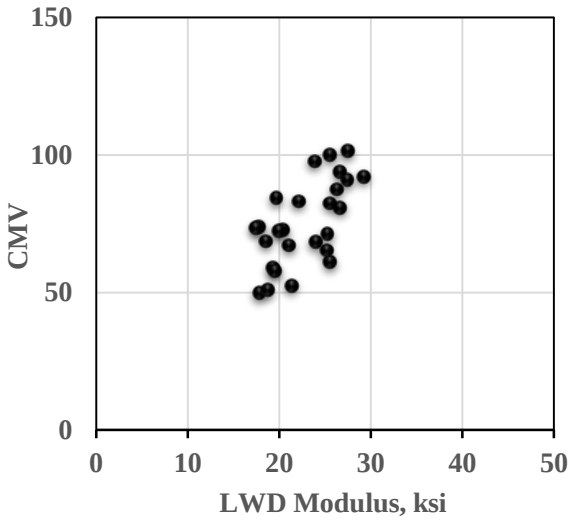

Figure A.6.51. Correlation of CMVs from CAT roller with LWD moduli

The CMVs from the retrofit systems on the HAMM and SAKAI rollers are compared with the spot test results in Figures A.6.52 through A.6.55.

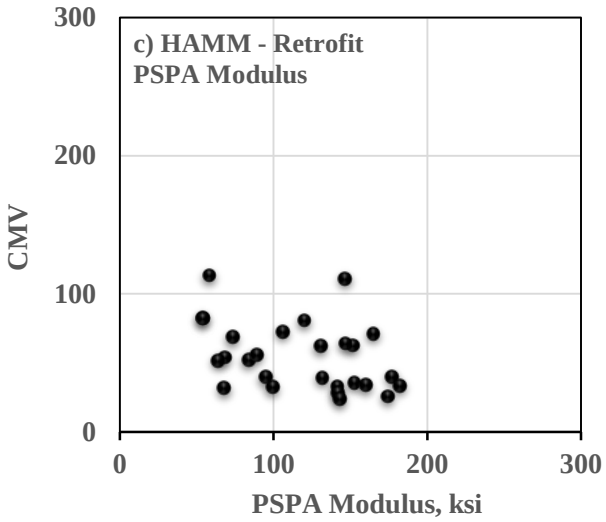

Figure A.6.52. Correlation of CMVs from retrofit system on HAMM roller with PSPA moduli

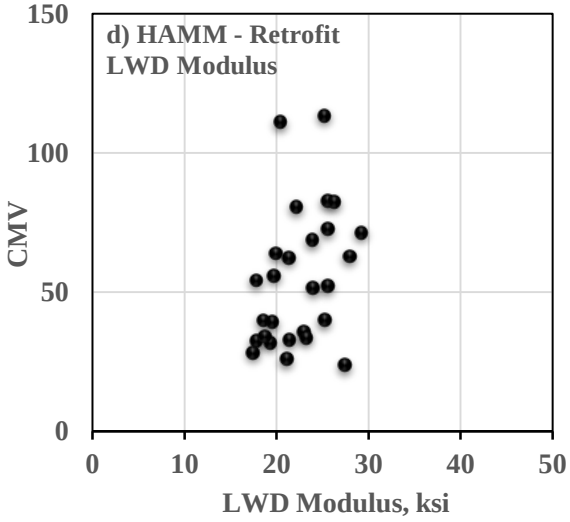

Figure A.6.53. Correlation of CMVs from retrofit system on HAMM roller with LWD moduli

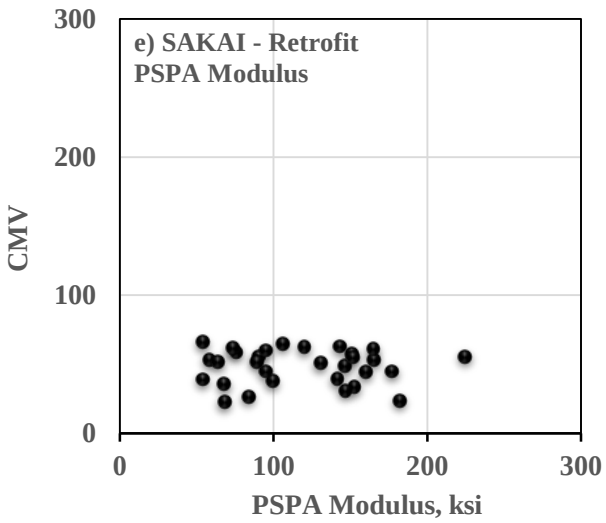

Figure A.6.54. Correlation of CMVs from retrofit system on SAKAI roller with PSPA moduli

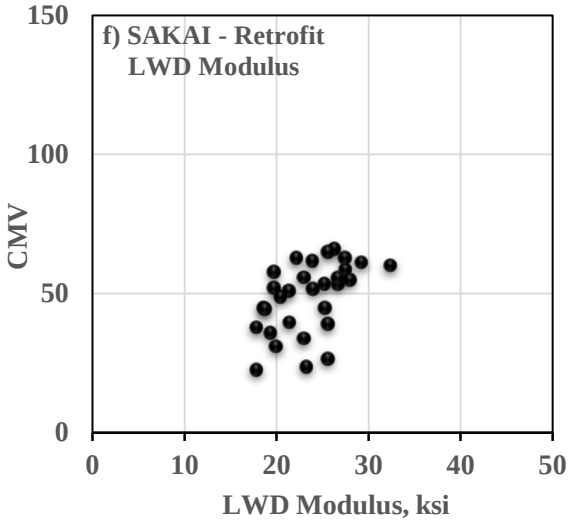

Figure A.6.55. Correlation of CMVs from retrofit system on SAKAI roller with LWD moduli

A.7. ANALYSIS OF INFORMATION FROM DATA ACQUISITION SYSTEM

A.7.1. Initial Evaluation

Figures A.7.1 through A.7.4 show the spectrogram of the vertical responses from the top embedded geophone during the stationary tests for the CAT roller.

Figures A.7.5 through A.7.8 summarize the spectrogram of the vertical response from the top embedded geophone during the stationary tests for the SAKAI roller. Figures A.7.9 through A.7.12 summarize the spectrogram of the vertical response from the top embedded geophone during the stationary tests for the HAMM roller.

Figure A.7.13 through A.7.24 summarize the spectrogram of vibration response from the mounted accelerometer on each roller during the stationary tests.

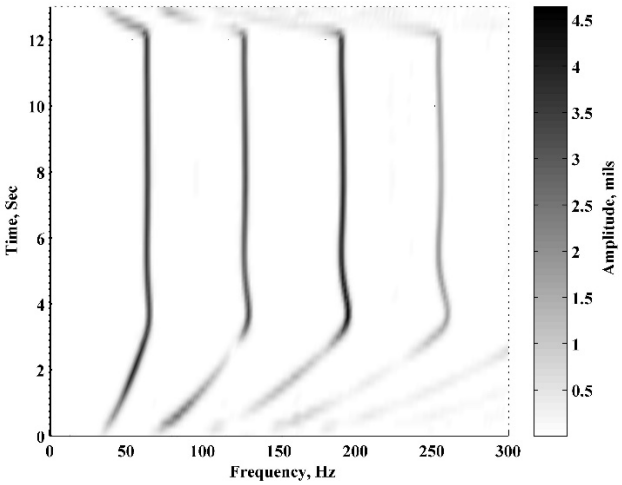

Figure A.7.1. Spectrogram of vertical response from the top geophone during stationary test (CAT roller) – high frequency and high amplitude

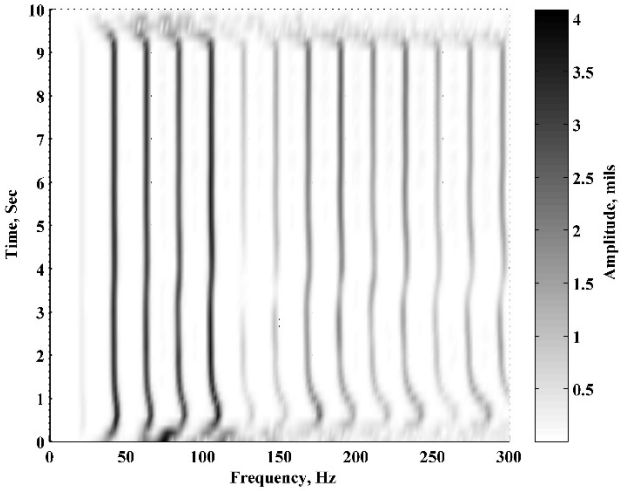

Figure A.7.3. Spectrogram of vertical response from the top geophone during stationary test (CAT roller) – low frequency and high amplitude

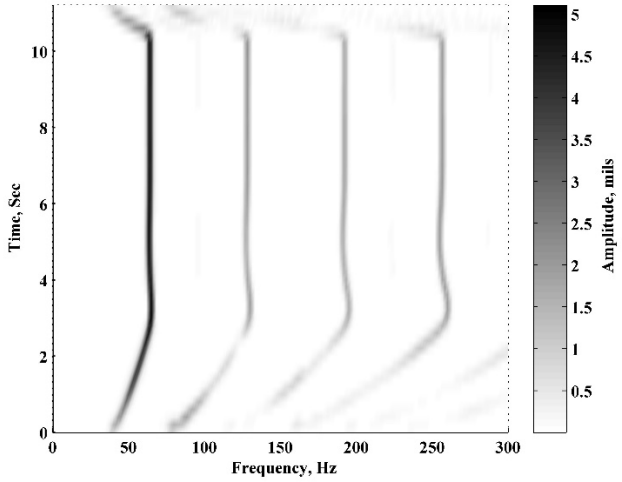

Figure A.7.2. Spectrogram of vertical response from the top geophone during stationary test (CAT roller) – high frequency and low amplitude

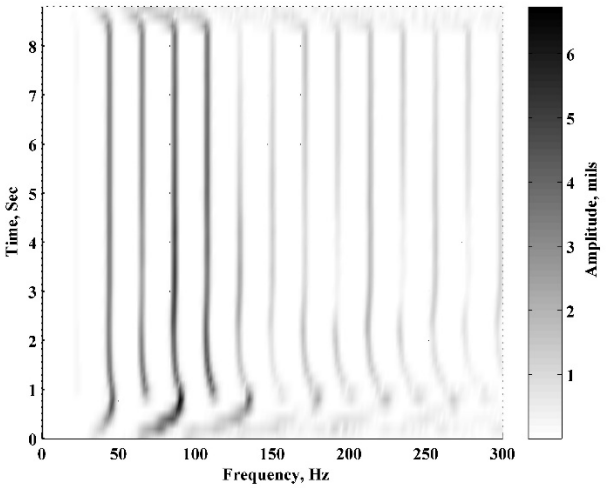

Figure A.7.4. Spectrogram of vertical response from the top geophone during stationary test (CAT roller) – low frequency and low amplitude

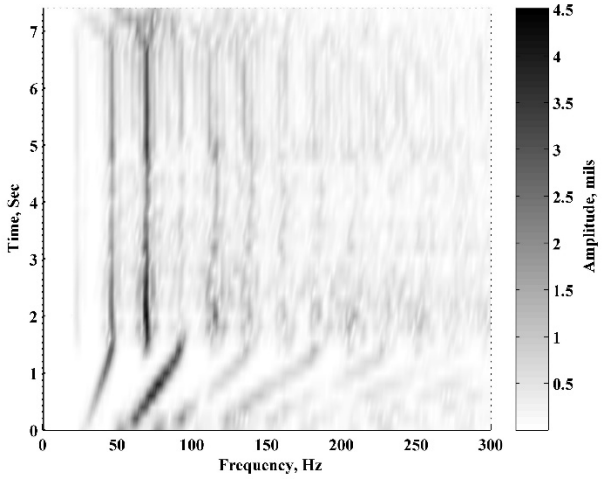

Figure A.7.5. Spectrogram of vertical response from the top geophone during stationary test (SAKAI roller) – high frequency and high amplitude

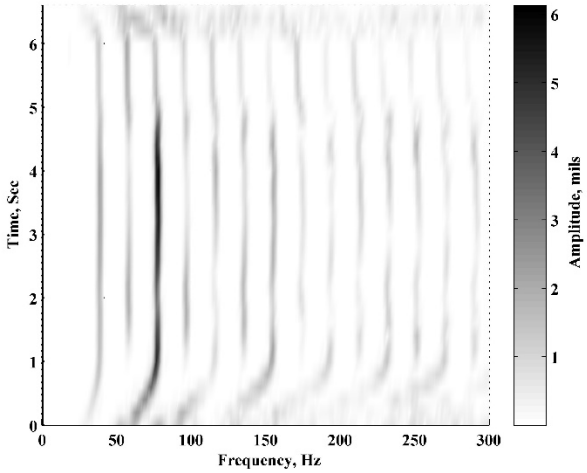

Figure A.7.7. Spectrogram of vertical response from the top geophone during stationary test (SAKAI roller) – low frequency and high amplitude

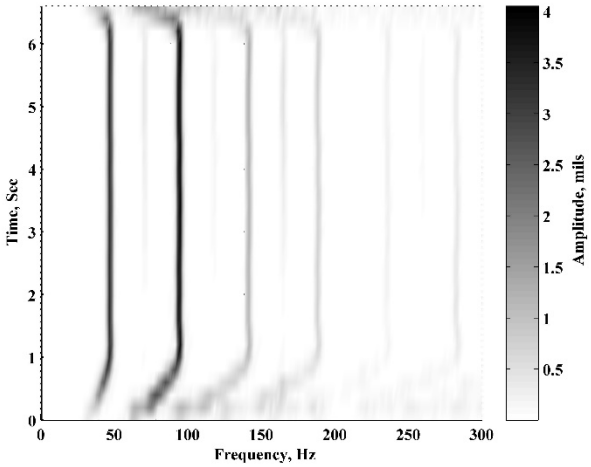

Figure A.7.6. Spectrogram of vertical response from the top geophone during stationary test (SAKAI roller) – high frequency and low amplitude

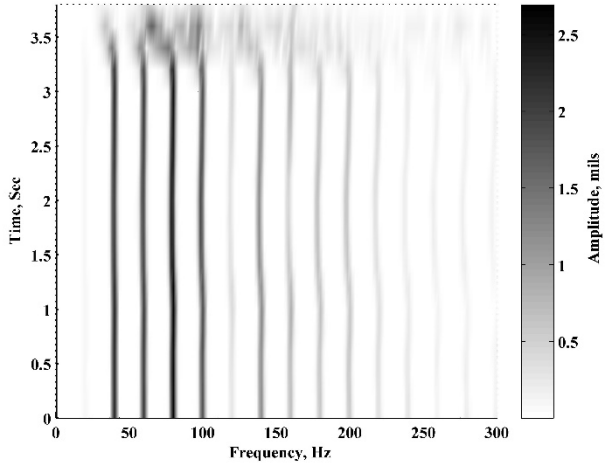

Figure A.7.8. Spectrogram of vertical response from the top geophone during stationary test (SAKAI roller) – low frequency and low amplitude

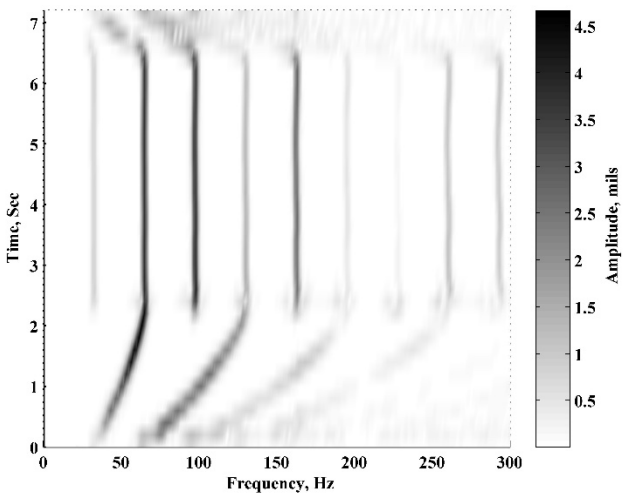

Figure A.7.9. Spectrogram of vertical response from the top geophone during stationary test (SAKAI roller) – super high frequency and high amplitude

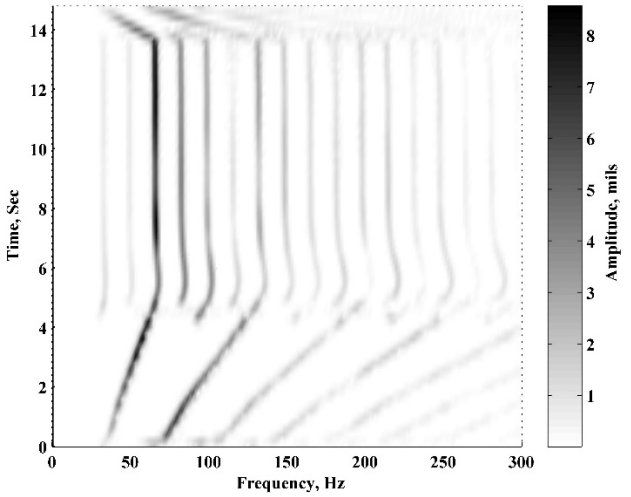

Figure A.7.10. Spectrogram of vertical response from the top geophone during stationary test (HAMM roller) – high frequency and low amplitude

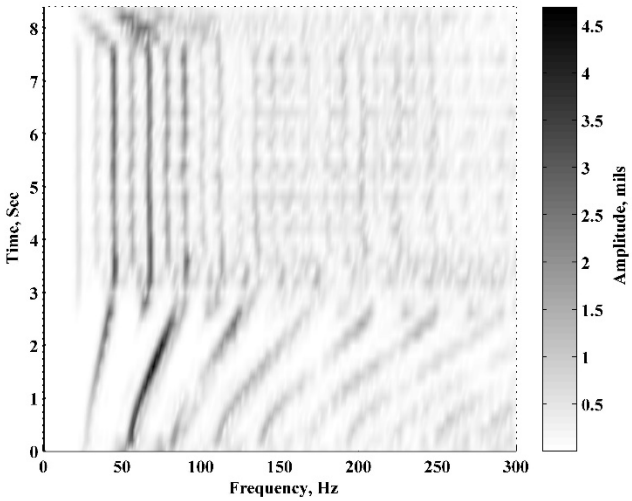

Figure A.7.11. Spectrogram of vertical response from the top geophone during stationary test (HAMM roller) – low frequency and high amplitude

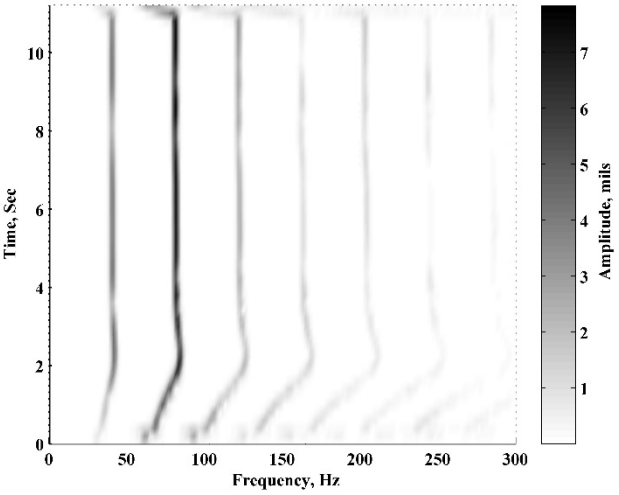

Figure A.7.12. Spectrogram of vertical response from the top geophone during stationary test (HAMM roller) – low frequency and low amplitude

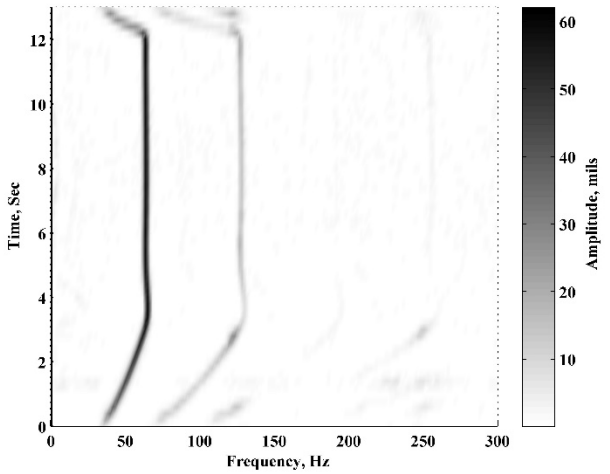

Figure A.7.13. Spectrogram of the response from mounted accelerometer during stationary test (CAT roller) – high frequency and high amplitude

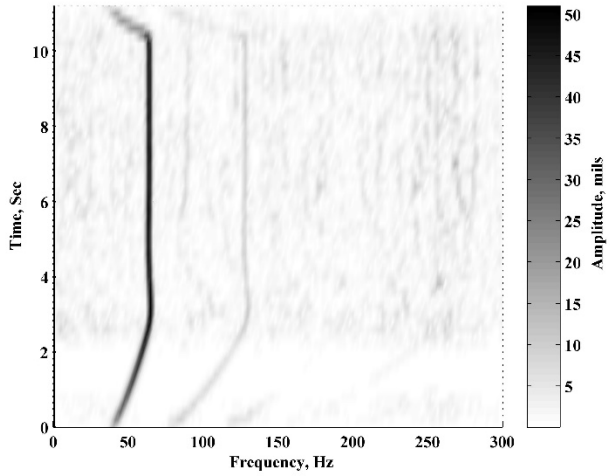

Figure A.7.14. Spectrogram of the response from mounted accelerometer during stationary test (CAT roller) – high frequency and low amplitude

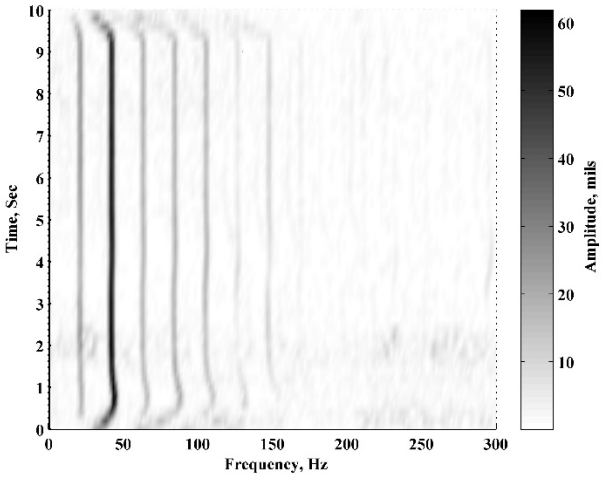

Figure A.7.15. Spectrogram of the response from mounted accelerometer during stationary test (CAT roller) – low frequency and high amplitude

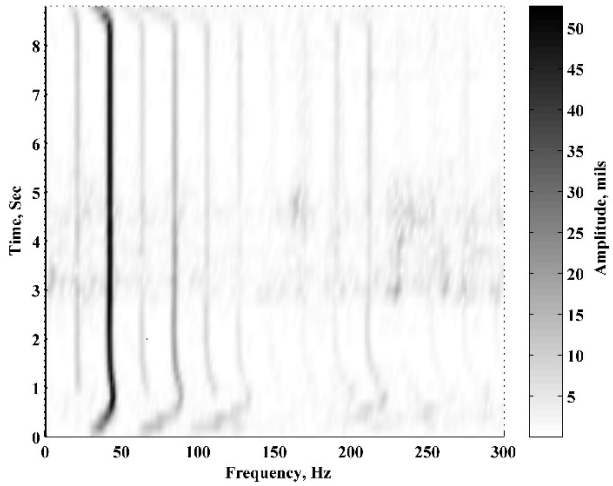

Figure A.7.16. Spectrogram of the response from mounted accelerometer during stationary test (CAT roller) – low frequency and low amplitude

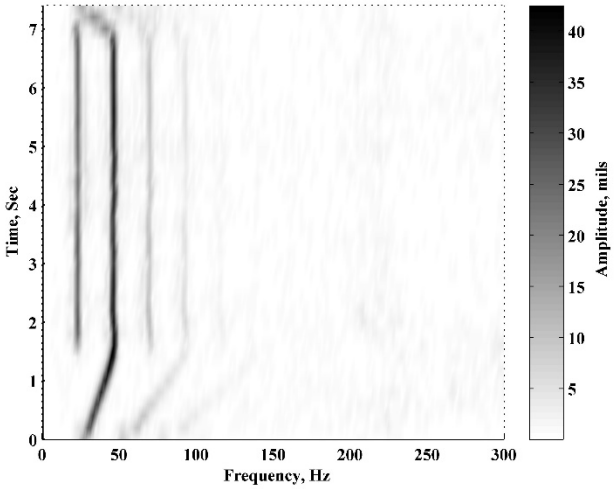

Figure A.7.17. Spectrogram of the response from mounted accelerometer during stationary test (SAKAI roller) – high frequency and high amplitude

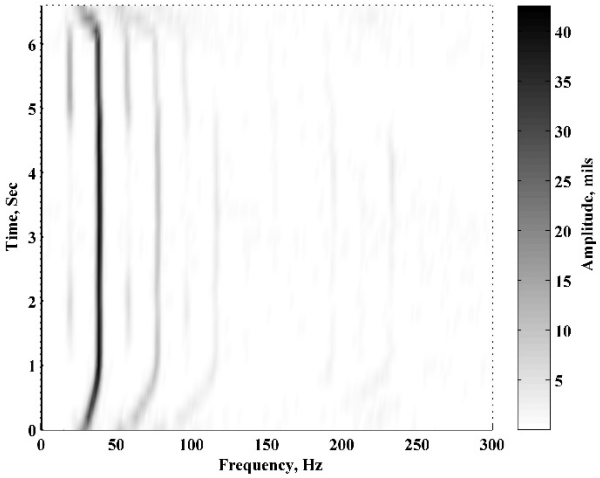

Figure A.7.19. Spectrogram of the response from mounted accelerometer during stationary test (SAKAI roller) – low frequency and high amplitude

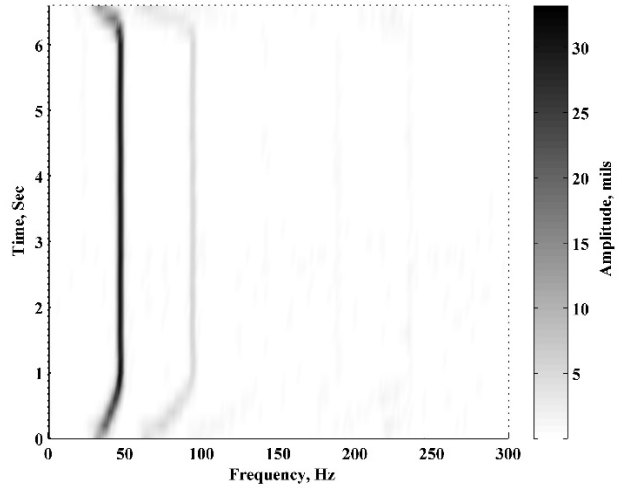

Figure A.7.18. Spectrogram of the response from mounted accelerometer during stationary test (SAKAI roller) – high frequency and low amplitude

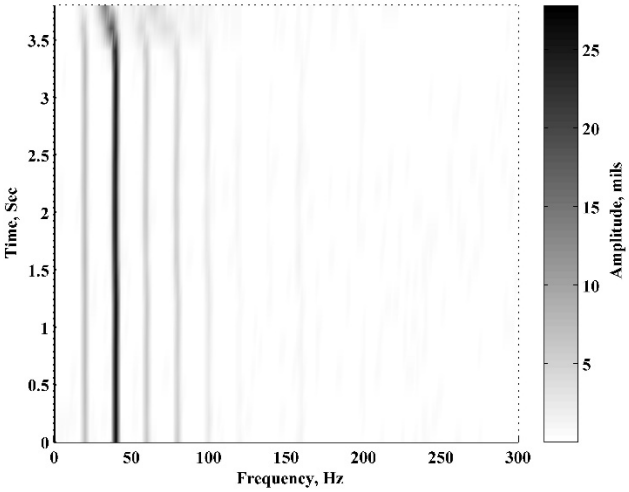

Figure A.7.20. Spectrogram of the response from mounted accelerometer during stationary test (SAKAI roller) – low frequency and low amplitude

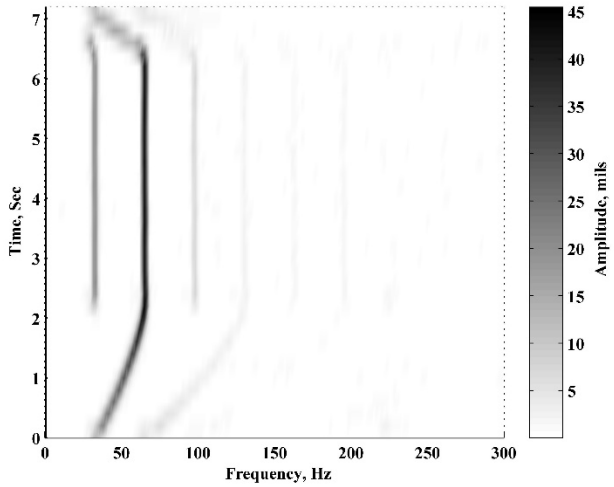

Figure A.7.21. Spectrogram of the response from mounted accelerometer during stationary test (SAKAI roller) – super high frequency and high amplitude

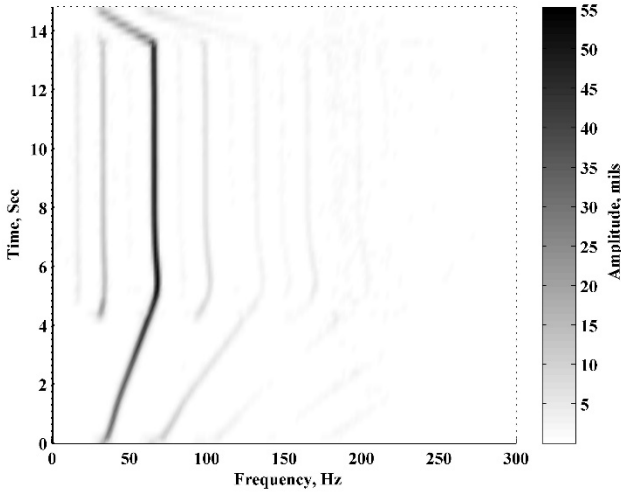

Figure A.7.22. Spectrogram of the response from mounted accelerometer during stationary test (HAMM roller) – high frequency and low amplitude

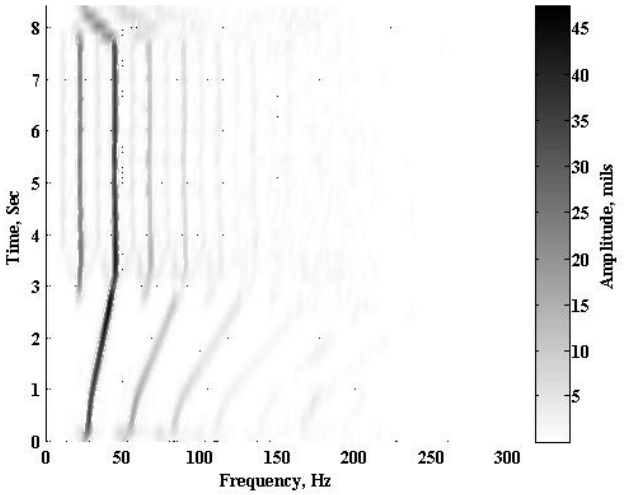

Figure A.7.23. Spectrogram of the response from mounted accelerometer during stationary test (HAMM roller) – low frequency and high amplitude

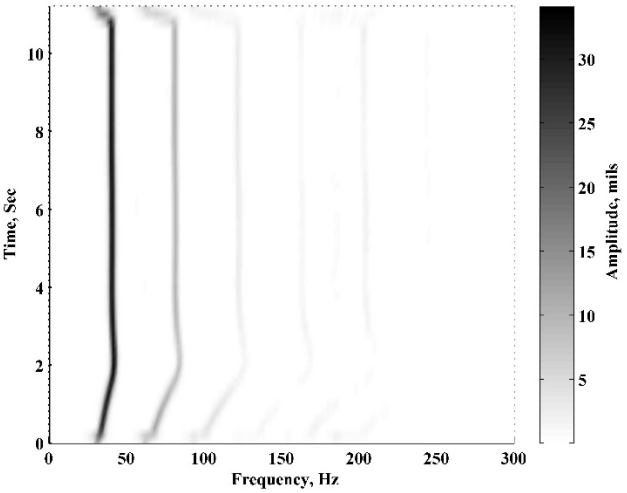

Figure A.7.24. Spectrogram of the response from mounted accelerometer during stationary test (HAMM roller) – low frequency and low amplitude

A.7.2. Vibration Evaluation

Figure A.7.25 illustrates the roller path with respect to the location of the embedded geophones within the test section during the moving vibration tests. The gridded area is compared with the measured GPS locations in Figure A.7.26.

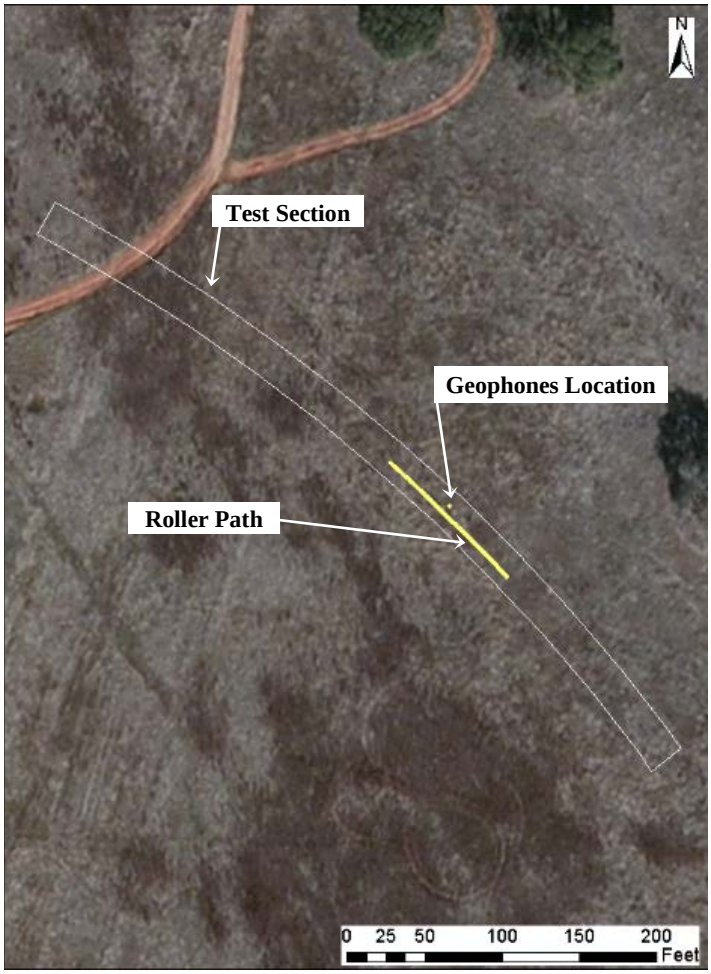

Figure A.7.25. Roller path with respect to geophones locations within the test section

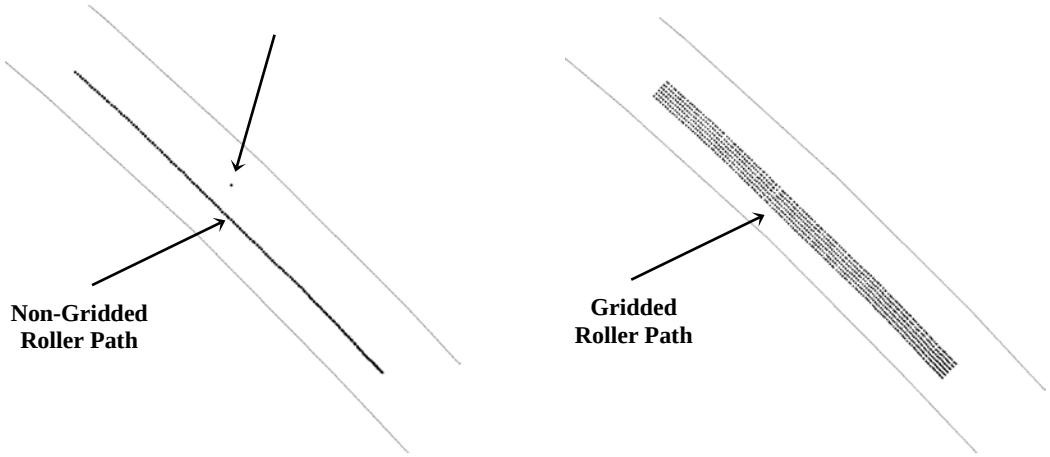

Figure A.7.26. Gridded data points compared to the original GPS locations

Figure A.7.27 summarizes the fundamental frequencies from the UTEP system and the retrofit kit. The peak amplitudes corresponding to the fundamental frequencies from the two systems are compared in Figure A.7.28. The calculated CMVs using the vibration data from the calibration system are compared with the reported CMVs by the retrofit kit in Figure A.7.29.

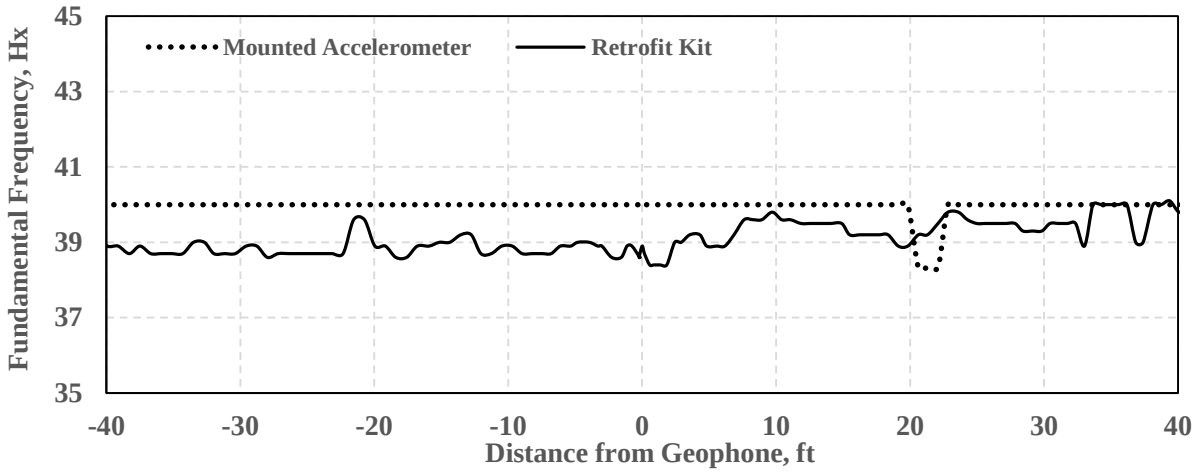

Figure A.7.27. Comparison of vibration frequency data from calibration system with retrofit kit for one roller pass (SAKAI roller)

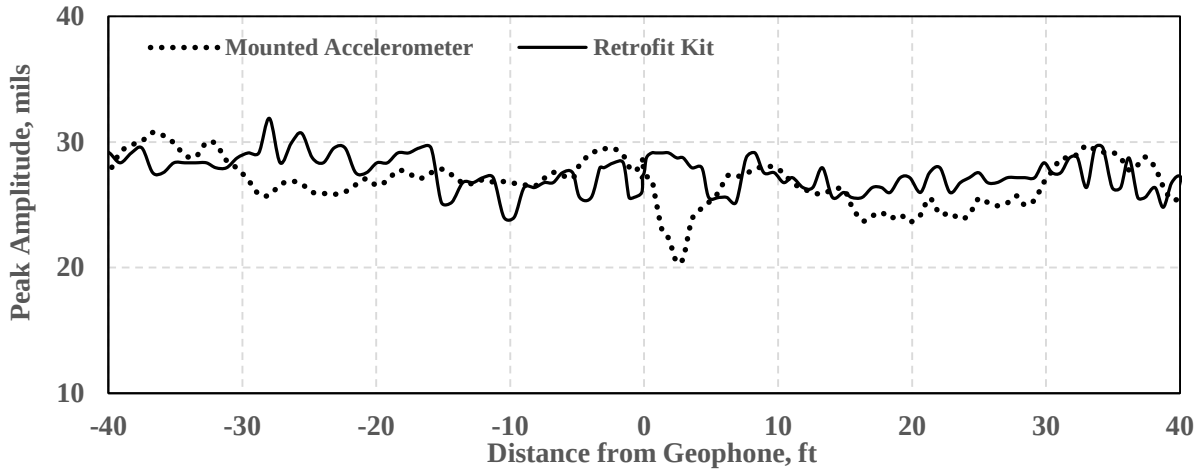

Figure A.7.28. Comparison of vibration amplitude data from calibration system with retrofit kit for one roller pass (SAKAI roller)

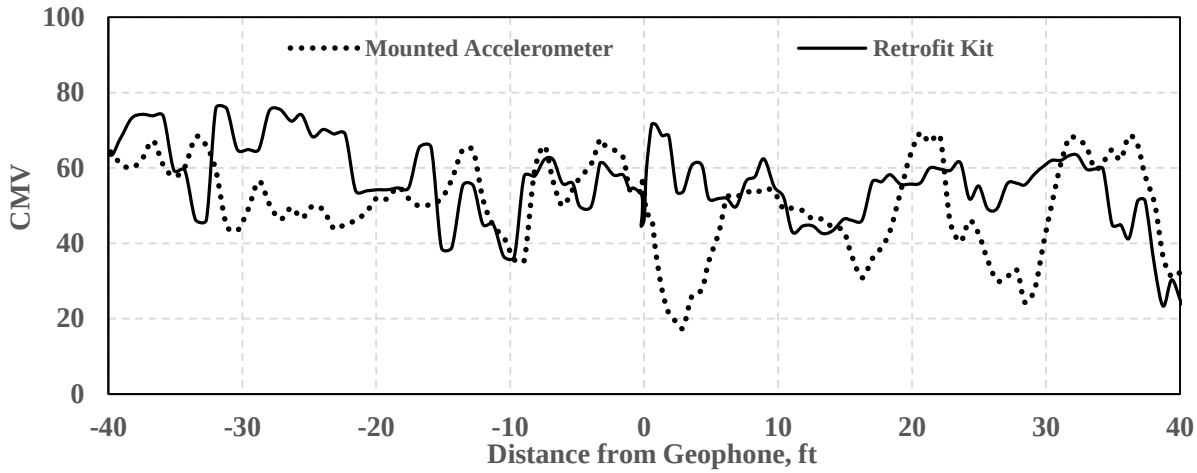

Figure A.7.29. Comparison of CMV data from calibration system, retrofit kit and spot tests for one roller pass (SAKAI roller)

The vertical accelerations of the fundamental mode of vibration from the two embedded geophones with respect to the distance of roller from the location of the geophones during the pre-mapping of the base layer are presented in Figure A.7.30. The transversal and longitudinal responses are summarized in Figures A.7.31 and A.7.32.

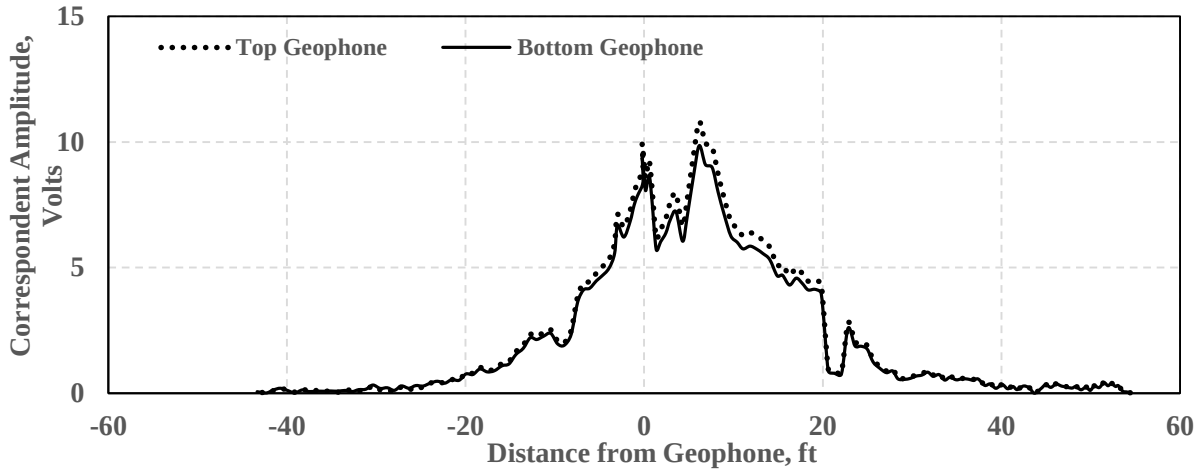

Figure A.7.30. Vertical response of geophones during one roller pass (SAKAI roller)

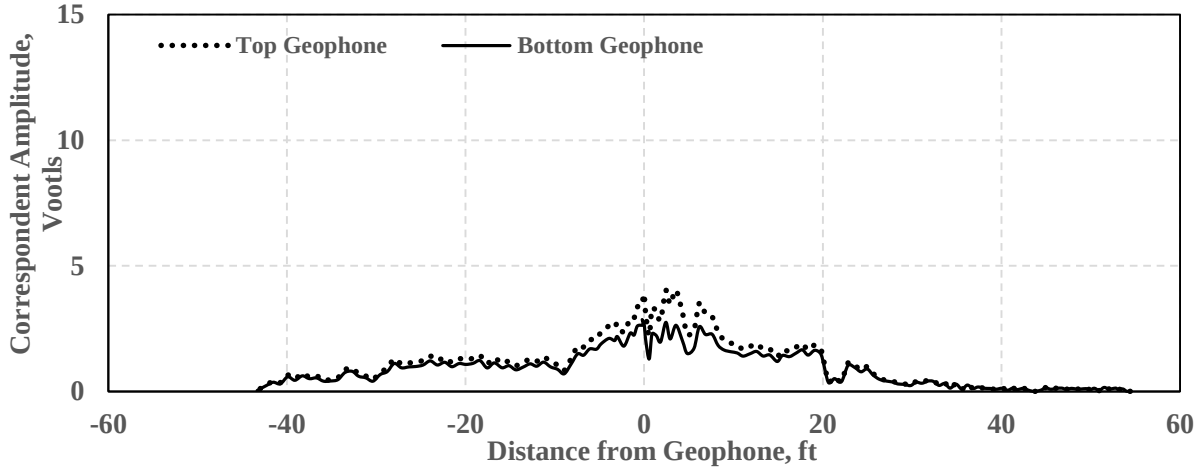

Figure A.7.31. Transversal response of geophones during one roller pass (SAKAI roller)

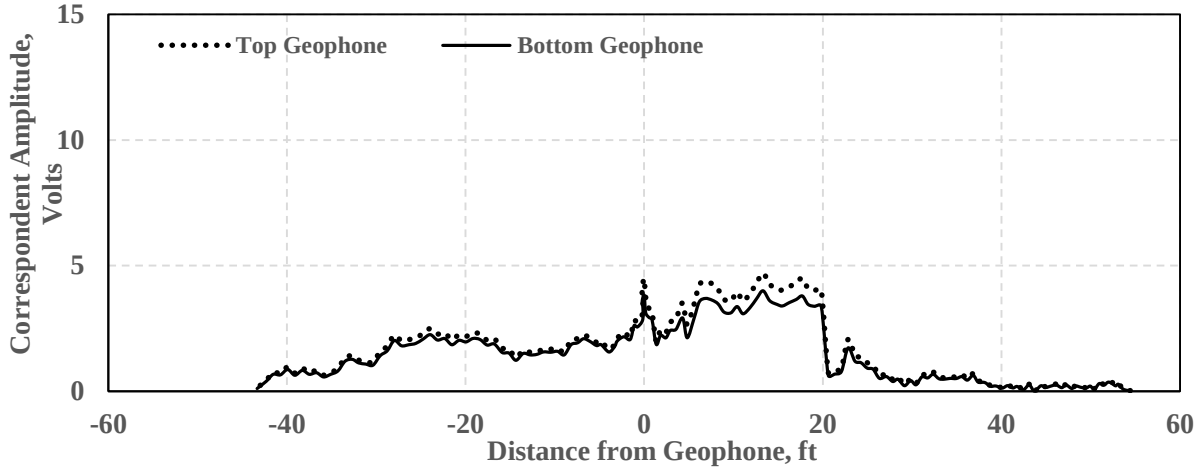

Figure A.7.32. Longitudinal response of geophones during one roller pass (SAKAI roller)

Figures A.7.33 and A.7.34 represent the spectrogram of the mounted accelerometer and top embedded geophone during the low frequency and high amplitude vibration of the SAKAI roller on the base layer during pre-mapping. Figures A.7.35 and A.7.36 illustrate the spectrogram of vibration responses from the accelerometers and geophones during another vibration setting of the SAKAI roller on the base layer. Figures A.7.37 and A.7.38 summarize the spectrogram of the response from the accelerometer and geophone during the pre-mapping of the base layer with the HAMM roller for the low frequency and high amplitude vibration setting. Furthermore, Figures A.7.39 and A.7.40 represent the spectrograms of vibration responses for the HAMM roller during the low frequency and low amplitude vibration.

.

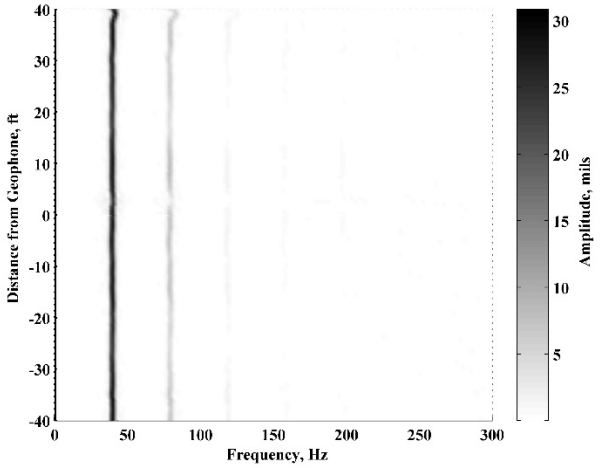

Figure A.7.33. Spectrogram of the response from mounted accelerometer during moving test (SAKAI roller) – low frequency and high amplitude

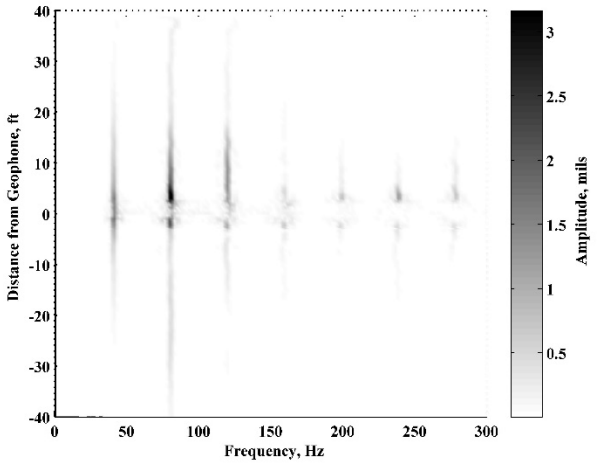

Figure A.7.34. Spectrogram of vertical response from the top geophone during moving test (SAKAI roller) – low frequency and high amplitude

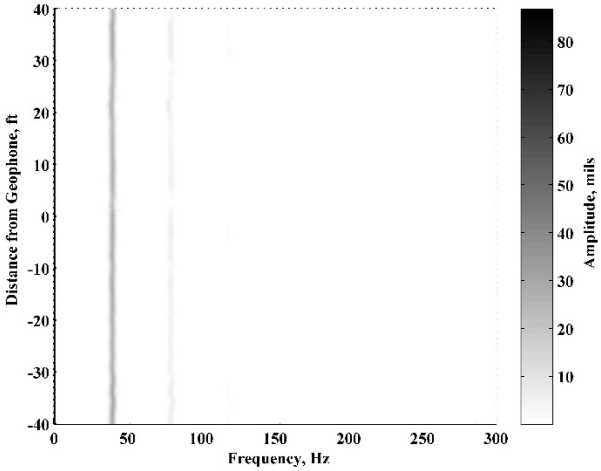

Figure A.7.35. Spectrogram of the response from mounted accelerometer during moving test (SAKAI roller) – low frequency and low amplitude

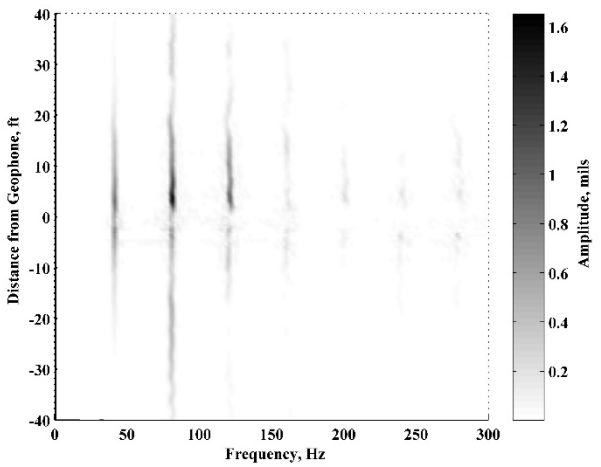

Figure A.7.36. Spectrogram of vertical response from the top geophone during moving test (SAKAI roller) – low frequency and low amplitude

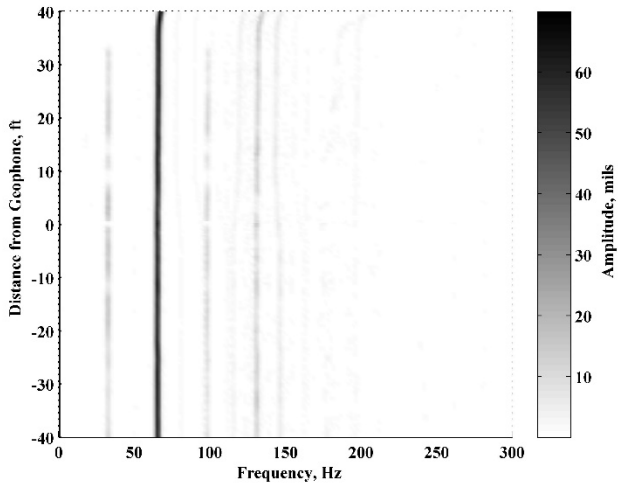

Figure A.7.37. Spectrogram of the response from mounted accelerometer during moving test (HAMM roller) – high frequency and high amplitude

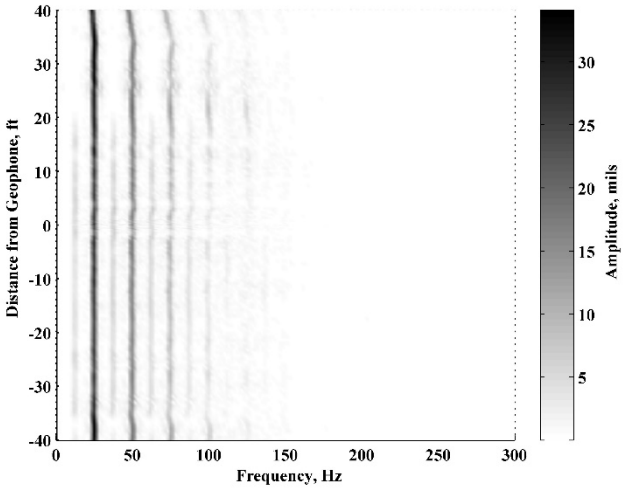

Figure A.7.39. Spectrogram of the response from mounted accelerometer during moving test (HAMM roller) – low frequency and low amplitude

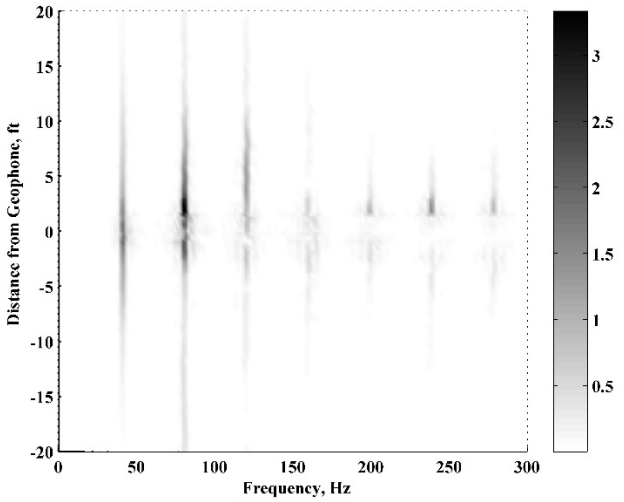

Figure A.7.38. Spectrogram of vertical response from the top geophone during moving test (HAMM roller) – high frequency and high amplitude

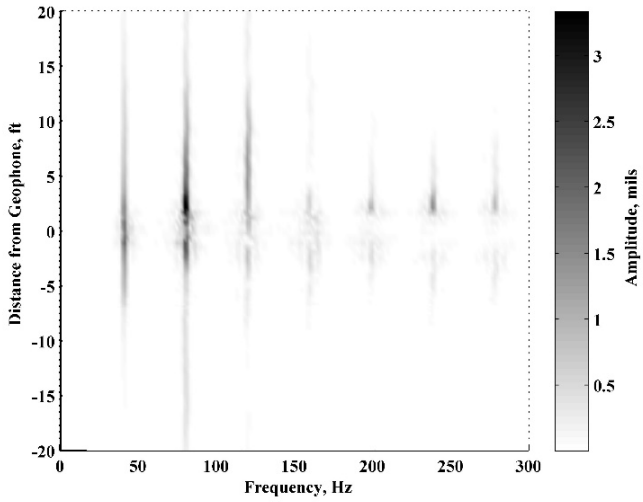

Figure A.7.40. Spectrogram of vertical response from the top geophone during moving test (HAMM roller) – low frequency and low amplitude

A.7.2. Compaction of First HMA Layer

Figure A.7.2.1 summarizes the fundamental vibration frequency of the two accelerometers mounted on opposite sides of the front drum and the vibration frequency from the OEM and retrofit systems. Figure A.7.2.2 summarizes the peak amplitudes that correspond to the fundamental frequency of vibration. Figure A.7.2.3 compares the calculated CMVs from the retrofit system with those from the mounted accelerometers. Figure A.7.2.4 compares the CCV values from the SAKAI OEM system and the CCVs calculated from the UTEP system.

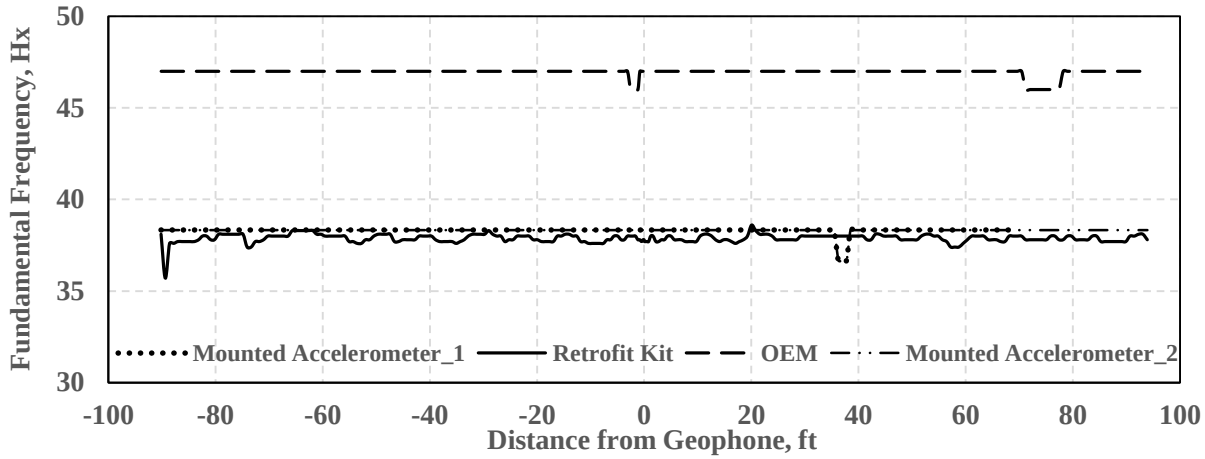

Figure A.7.2.1. Vibration frequency of mounted accelerometers compared to the OEM and retrofit systems during compaction of first HMA layer (SAKAI roller)

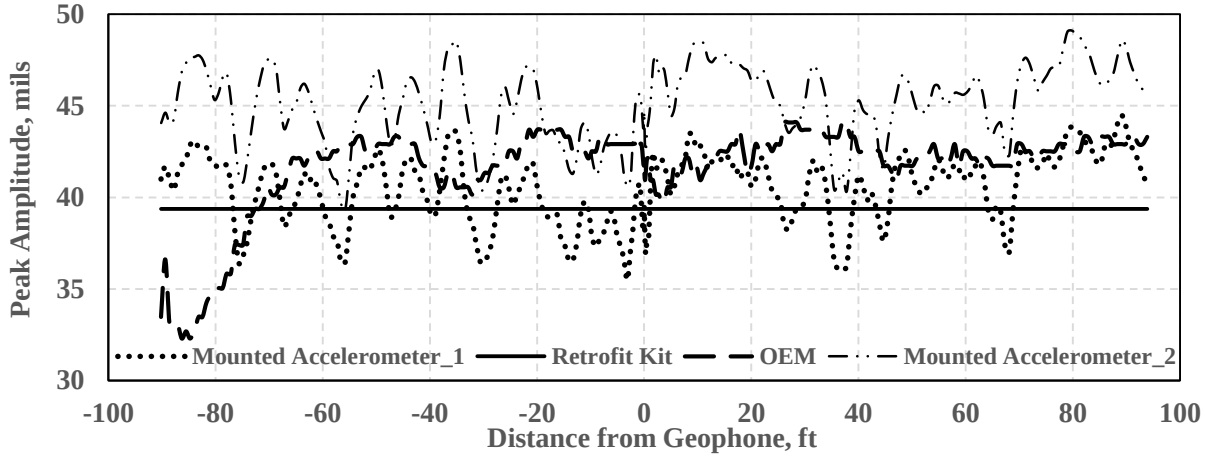

Figure A.7.2.2. Vibration amplitude of mounted accelerometers compared to the OEM and retrofit systems during compaction of first HMA layer (SAKAI roller)

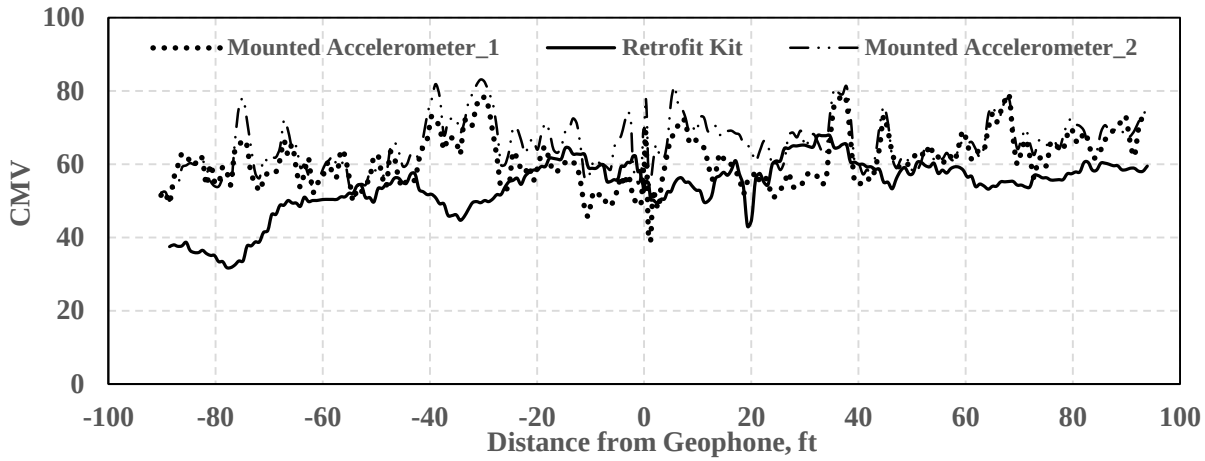

Figure A.7.2.3. CMVs calculated from mounted accelerometers compared to the retrofit system during compaction of first HMA layer (SAKAI roller)

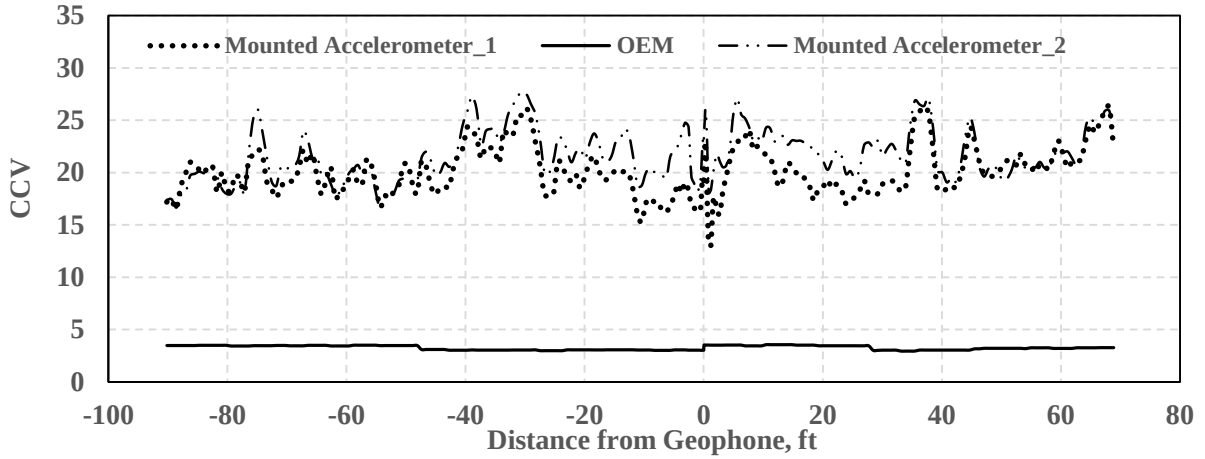

Figure A.7.2.4. CCVs calculated from mounted accelerometers compared to the OEM system during compaction of first HMA layer (SAKAI roller)

Figures A.7.2.5 and A.7.2.6 summarize the spectrograms of the vibration response from the mounted accelerometer and the embedded geophone during the low frequency and high amplitude vibration setting of the SAKAI roller for compaction of the first HMA layer. Furthermore, Figures A.7.2.7 and A.7.2.8 summarize the same responses during the high frequency and low amplitude settings.

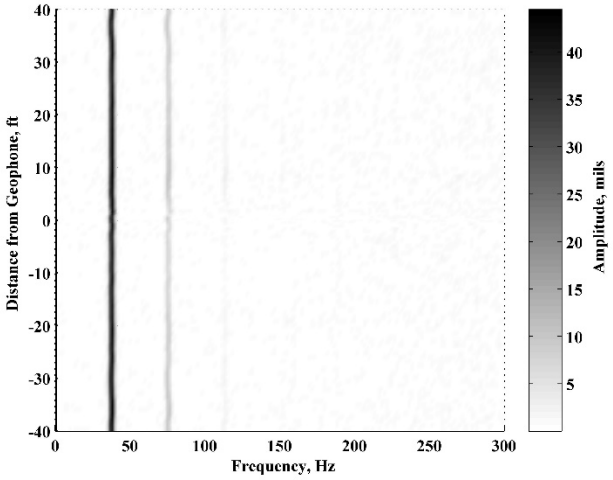

Figure A.7.2.5 Spectrogram of the response from mounted accelerometer during moving test (SAKAI roller) – low frequency and high amplitude – first HMA layer

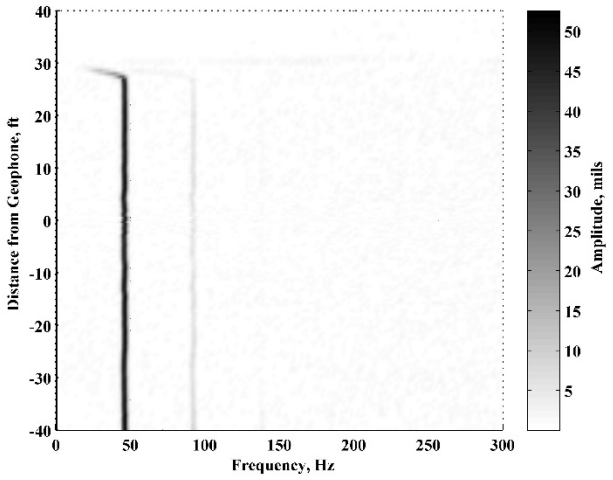

Figure A.7.2.7. Spectrogram of the response from mounted accelerometer during moving test (SAKAI roller) – high frequency and low amplitude – first HMA layer

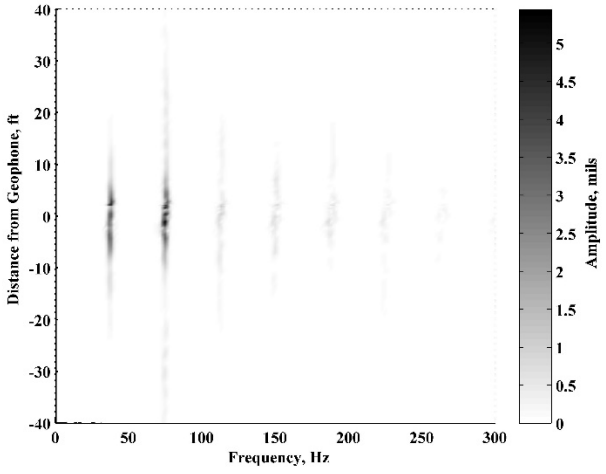

Figure A.7.2.6. Spectrogram of vertical response from the top geophone during moving test (SAKAI roller) – low frequency and high amplitude – first HMA layer

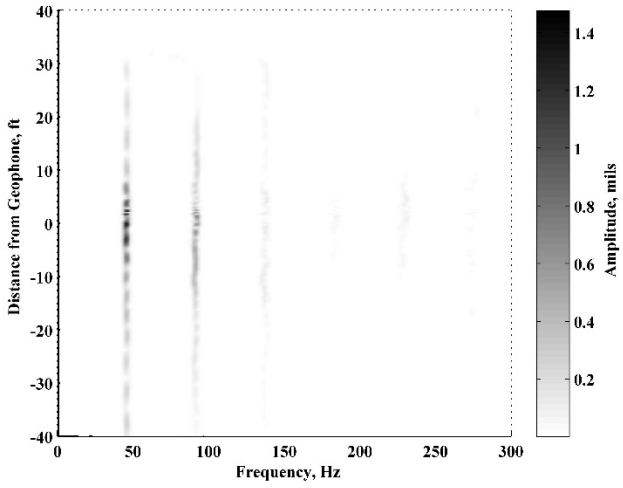

Figure A.7.2.8. Spectrogram of vertical response from the top geophone during moving test (SAKAI roller) – high frequency and low amplitude – first HMA layer

A.7.3. Compaction of Second HMA Layer

Figure A.7.3.1 shows the vibration frequency captured from the UTEP system as well as the OEM and retrofit systems again mounted on the Sakai roller. Figure A.7.3.2 compares the amplitudes at the fundamental frequencies from the UTEP system compared to the OEM and retrofit systems. Figure A.7.3.3 compares the CMVs reported from the retrofit kit with those calculated from the UTEP system.

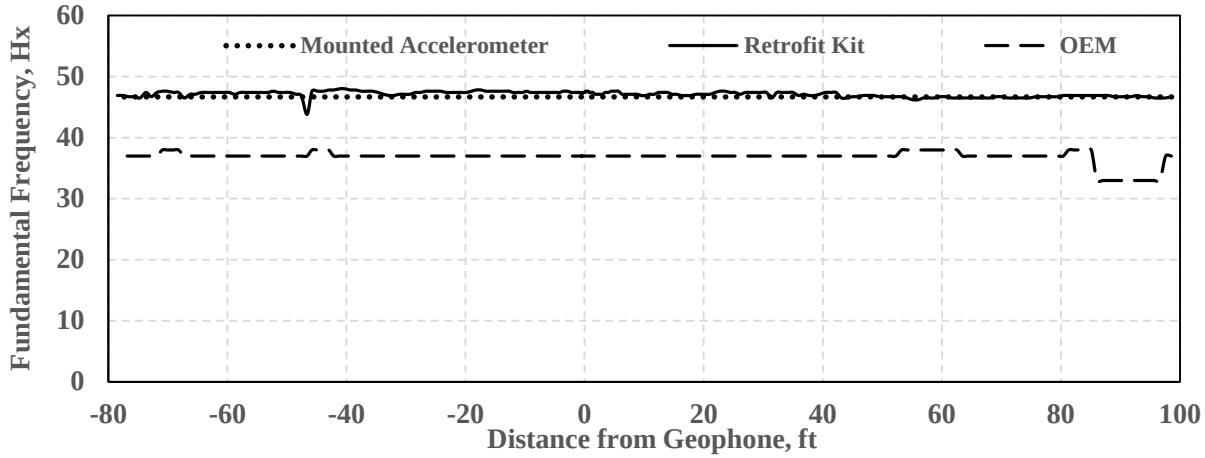

Figure A.7.3.1. Vibration frequency of mounted accelerometer compared to the OEM and retrofit systems during compaction of second HMA layer (SAKAI roller)

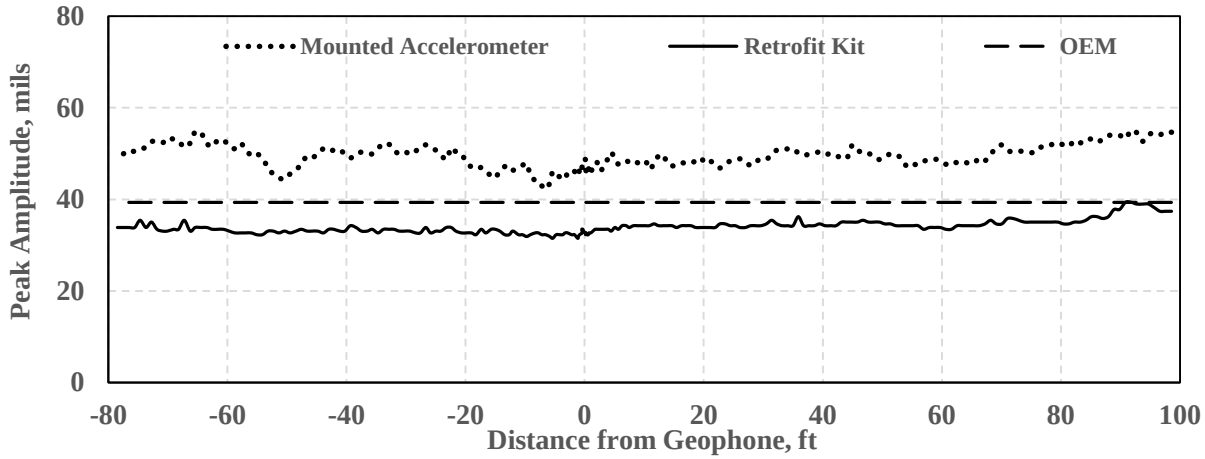

Figure A.7.3.2. Vibration amplitude of mounted accelerometers compared to the OEM and retrofit systems during compaction of second HMA layer (SAKAI roller)

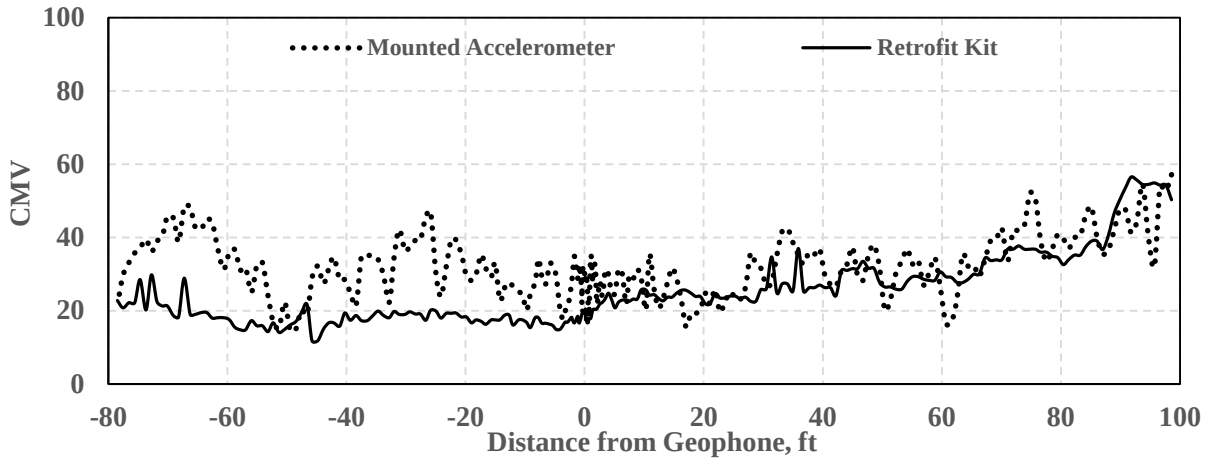

Figure A.7.3.3. CMVs calculated from mounted accelerometers compared to the retrofit system during compaction of second HMA layer (SAKAI roller)

Figure A.7.3.4 compares the CCVs calculated from calibration system with those reported from SAKAI OEM system.

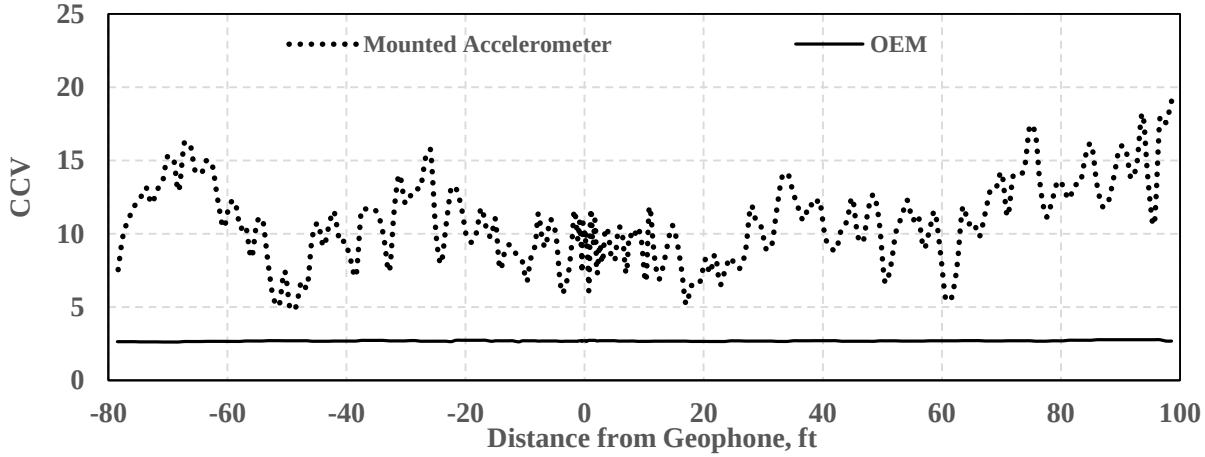

Figure A.7.3.4. CCVs calculated from mounted accelerometers compared to the OEM system during compaction of second HMA layer (SAKAI roller)

Figures A.7.3.5 and A.7.3.6 represent the spectrograms of vibration response from the accelerometer and geophone during the final pass on the second HMA lift.

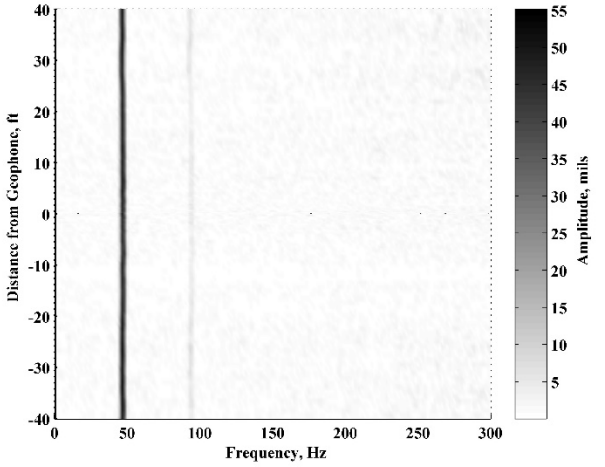

Figure A.7.3.5. Spectrogram of the response from mounted accelerometer during moving test (SAKAI roller) – high frequency and high amplitude – second HMA lift – final pass

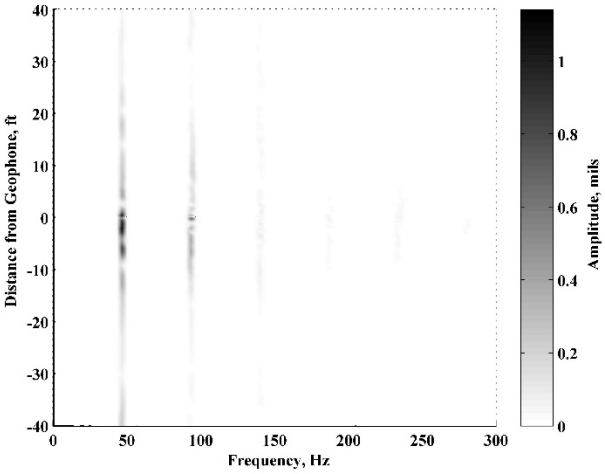

Figure A.7.3.6. Spectrogram of vertical response from the top geophone during moving test (SAKAI roller) – high frequency and high amplitude – second HMA lift – final pass

A.7.4. Investigating the Surface and Ground Deflections

The surface and ground deflections during the stationary vibrations from the CAT, HAMM and SAKAI rollers are summarized in Figures A.7.4.1 through A.7.4.3 for various vibration settings. Figures A.7.4.4 and A.7.4.5 summarize the deflections of the surface and ground layers during the pre-mapping of base layer with the SAKAI and HAMM rollers.

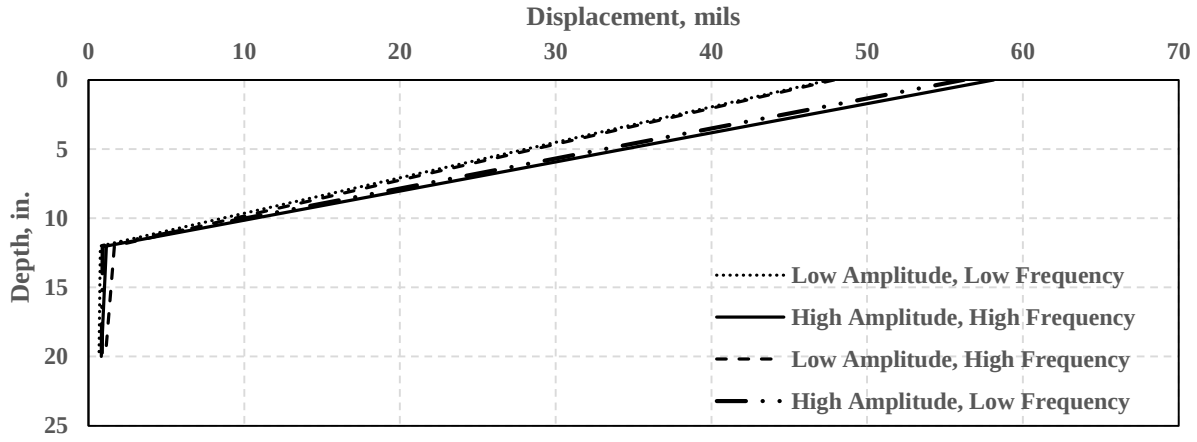

Figure A.7.4.1. Comparing surface and ground deflections during the stationary vibration tests (CAT roller)

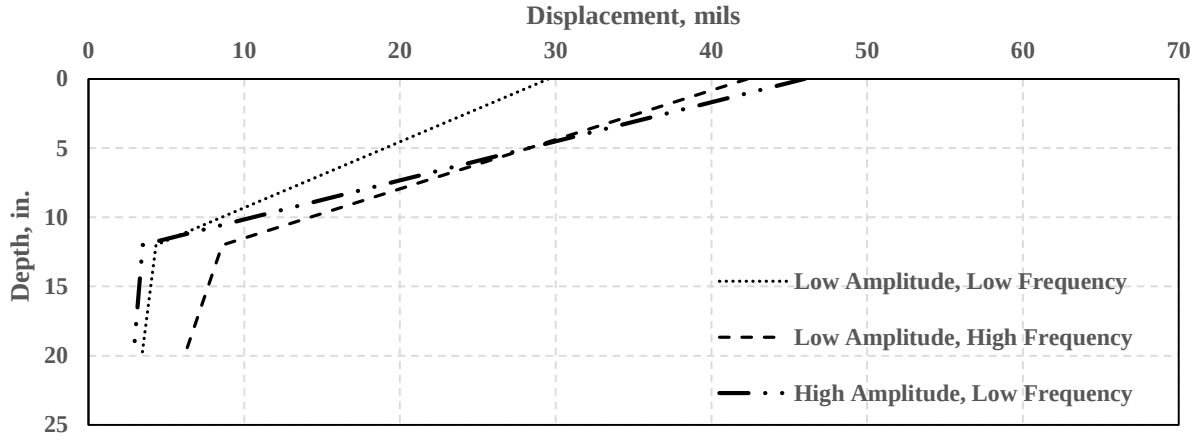

Figure A.7.4.2. Comparing surface and ground deflections during the stationary vibration tests (HAMM roller)

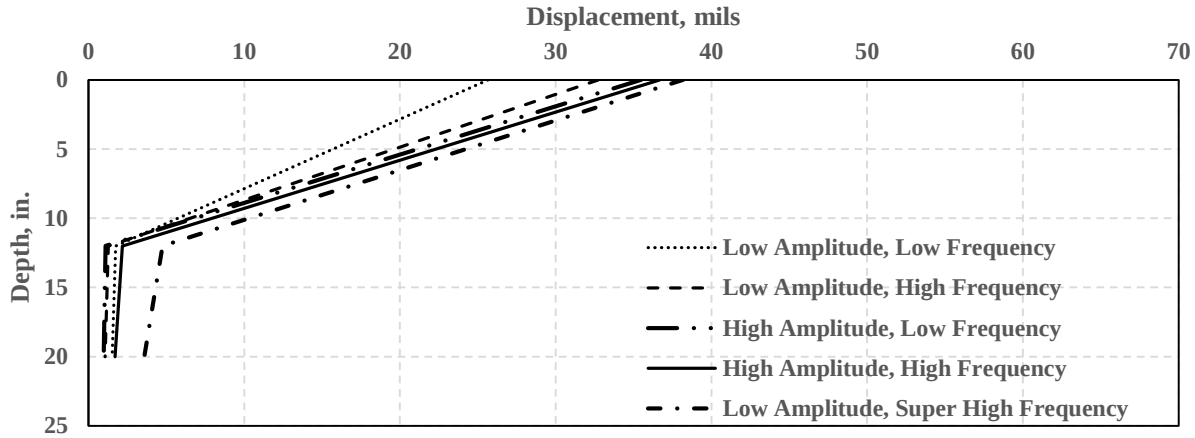

Figure A.7.4.3. Comparing surface and ground deflections during the stationary vibration tests (SAKAI roller)

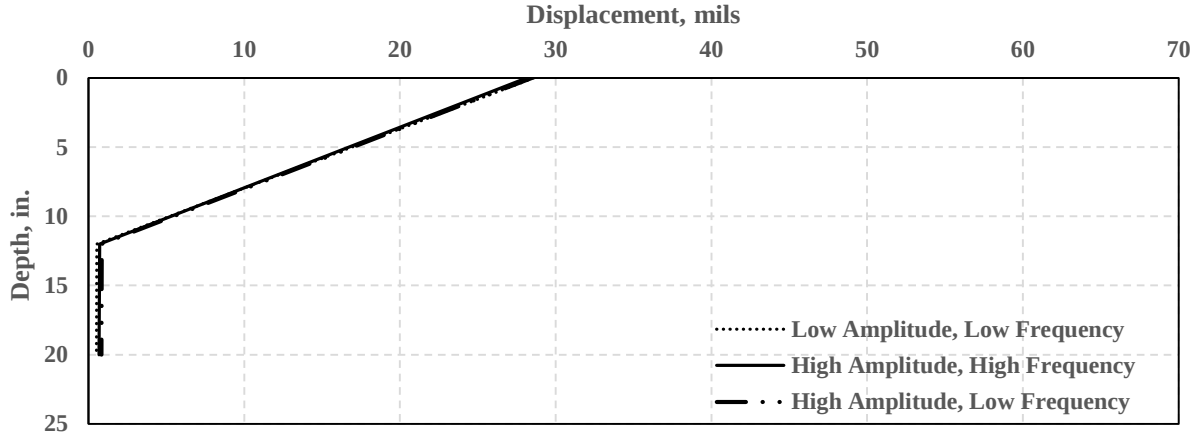

Figure A.7.4.4. Comparing surface and ground deflections during the moving vibration tests (SAKAI roller)

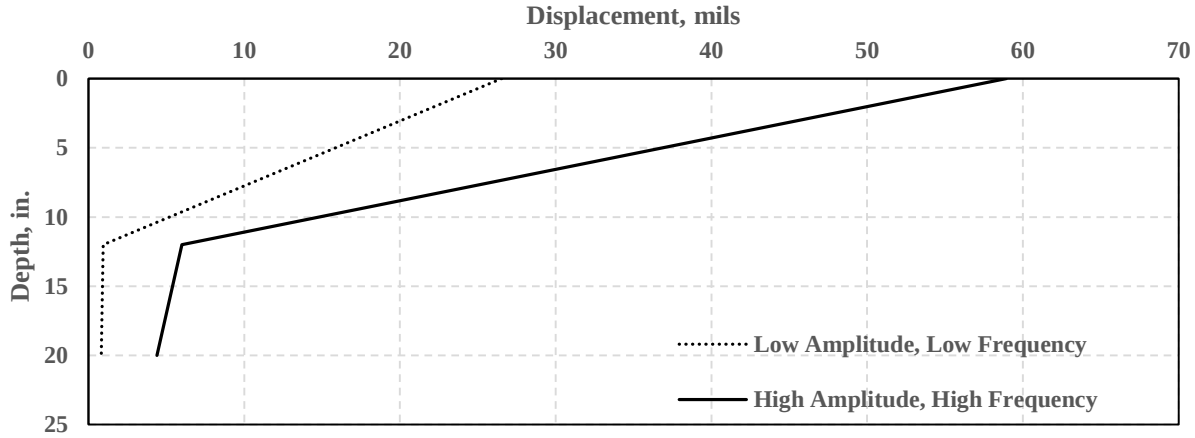

Figure A.7.4.5. Comparing surface and ground deflections during the moving vibration tests (HAMM roller)

Figures A.7.4.6 and A.7.4.7 illustrate the roller deflections on the surface and the corresponding geophone deflections during the compaction of the first and second HMA lifts.

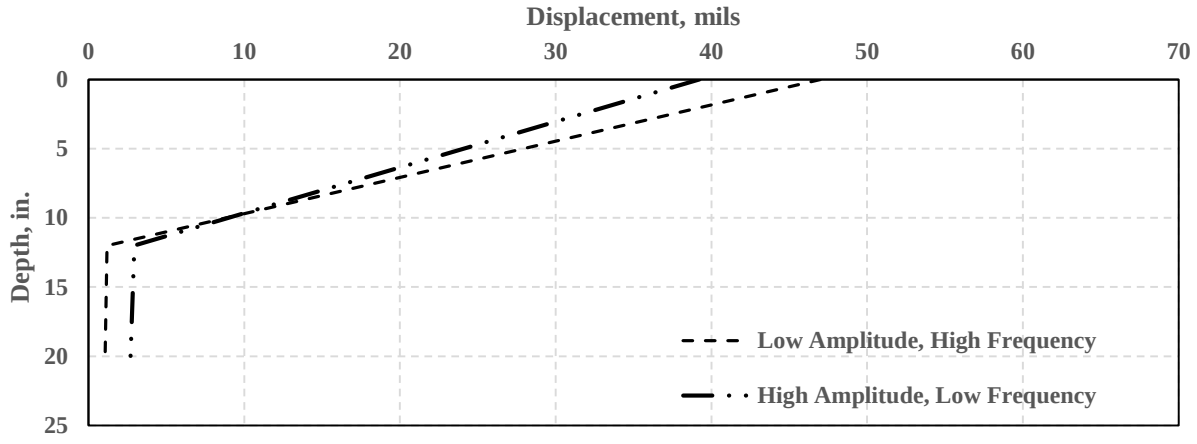

Figure A.7.4.6. Comparing surface and ground deflections during the moving vibration tests (SAKAI roller) – first HMA lift

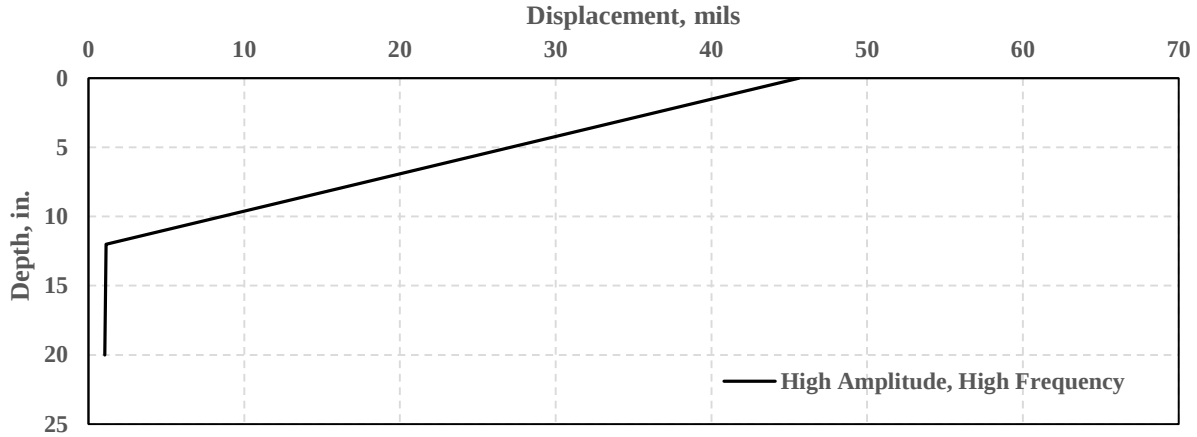

Figure A.7.4.7. Comparing surface and ground deflections during the moving vibration tests (SAKAI roller) – second HMA lift

APPENDIX B – EQUIPMENT RODEO ON SOIL

B.1. INTRODUCTION

The project location selected for the soils rodeo was at the junction of US 67 Business and County Road 801B near Cleburne, TX. Figure B.1.1 illustrates the aerial view of the test section. This test section was a part of the US 67 widening which included embankment as well as placement and compaction of 12 in. of clayey subgrade layer. Figure B.1.2 illustrates the location of this test section on the drawings of the project. The typical cross sections are depicted in Figure B.1.3. A 500 ft long and 25 ft wide test section was selected on the east bound frontage road to perform the IC data collection. Figure B.1.4 illustrates the schematic of test section and the testing grid to perform the spot tests and taking soil samples.

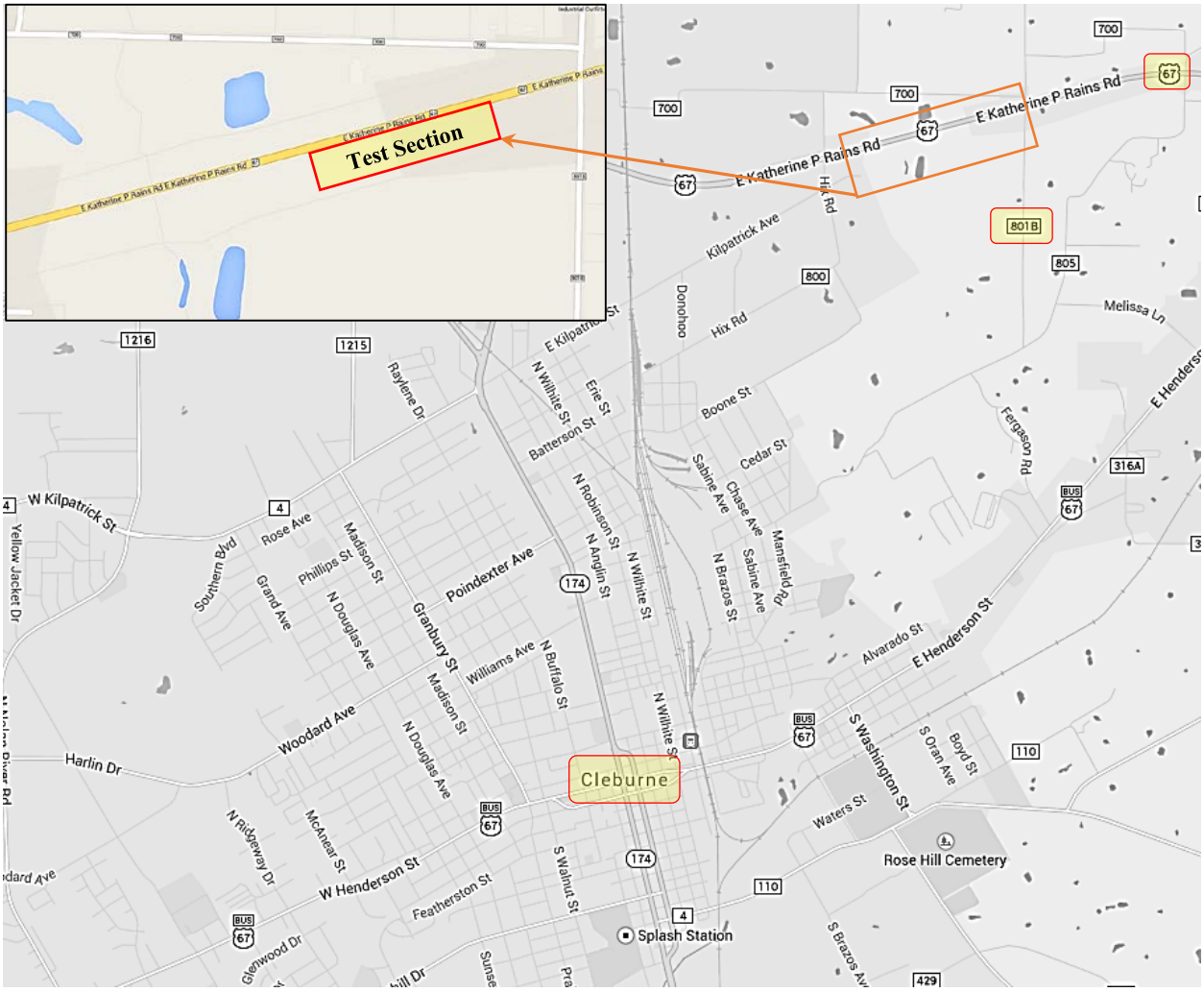

Figure B.1.1. Aerial view of the test section

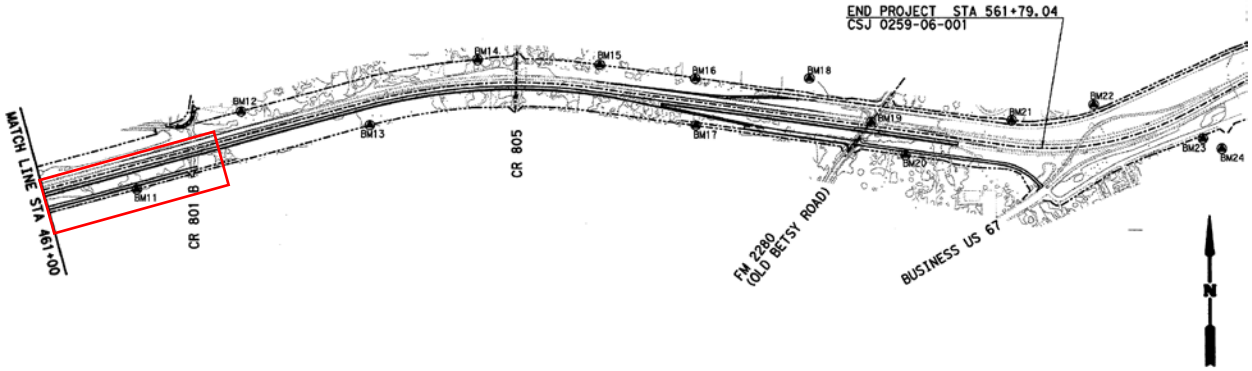

Figure B.1.2. Location of construction site

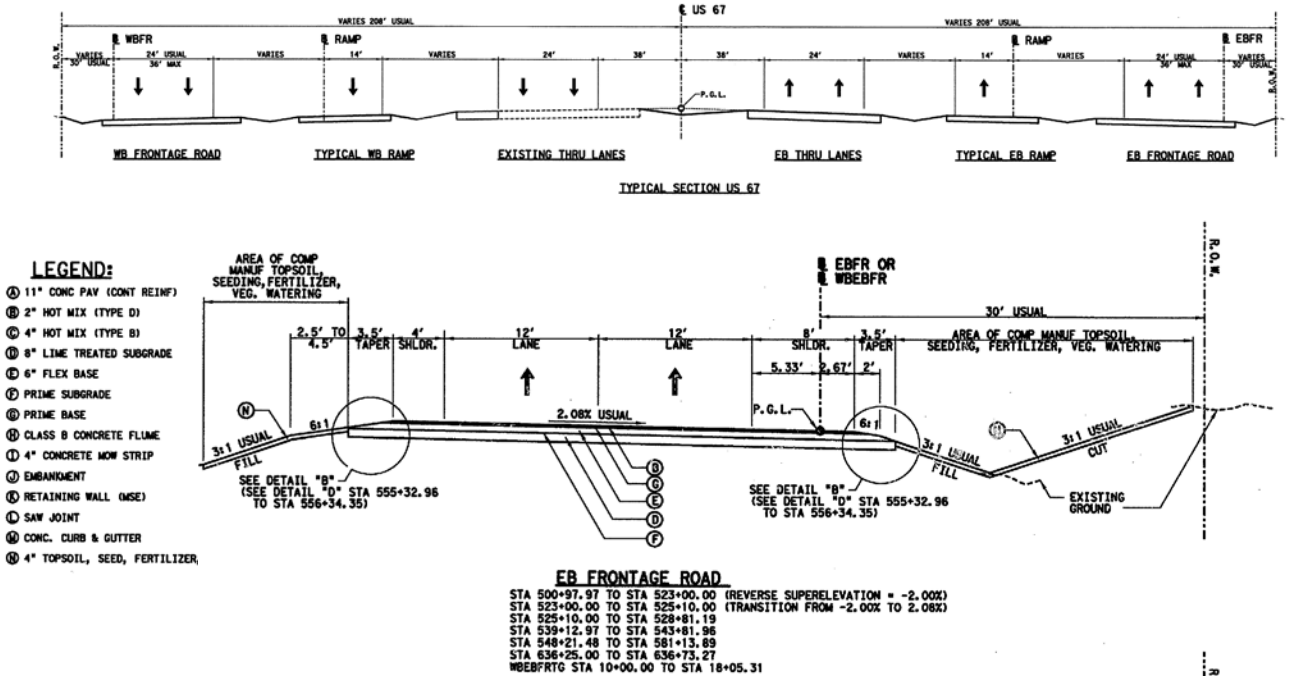

Figure B.1.3. Typical cross section of the designated road

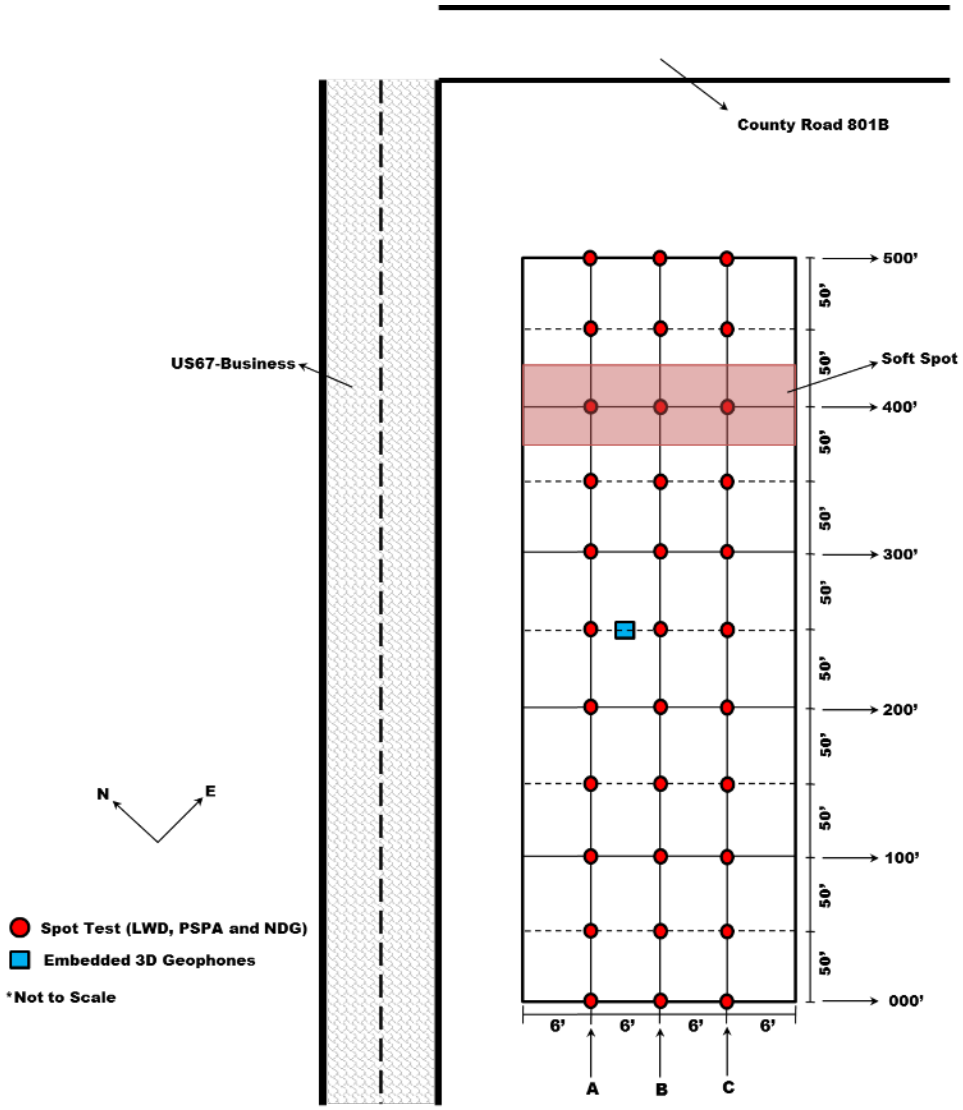

Figure B.1.4. Location of spot tests and geophones

The following spot tests were performed on the testing grid to evaluate the stiffness/modulus of the test section and further establish possible correlations with the IC data:

- Light Weight Deflectometer (LWD) as per ASTM E2583
- Portable Seismic Property Analyzer (PSPA)
- Dynamic Cone Penetrometer (DCP) as per ASTM D6951
- Falling Weight Deflectometer (FWD)

To estimate the moisture content and density of the compacted soil layers, the following spot tests were undertaken:

- Nuclear Density Gauge (NDG) as per ASTM D6938
- Field samples of base materials for estimation of index properties and oven dry tests (as per ASTM D2216)

Figures B.1.5 and B.1.6 illustrate the location of the test section as well as spot tests on the compacted soil layer.

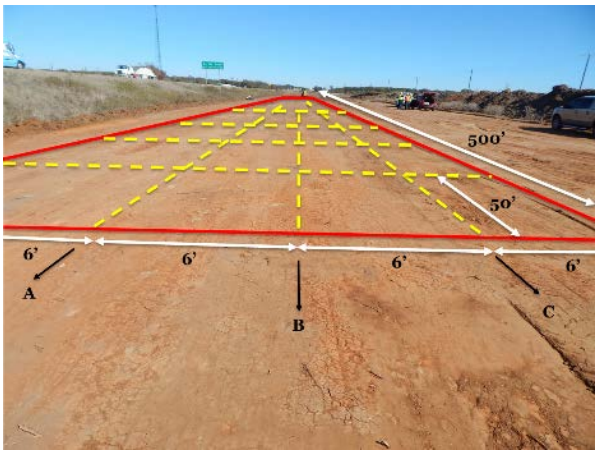

Figure B.1.5. Location of test section on compacted soil layer

Figure B.1.6. Performing spot tests on testing section

To estimate the precise coordinates of the testing points and the test section, a local TOPCON GPS base station was set up next to the test section. A GPS rover was then employed to locate the test spots and later map the test grid after the compaction of the subgrade layer. The UTM coordinate system was selected as the reference for this test section. However, the State Plane System and Texas North Central Virtual Reference Station (VRS) were utilized to map the IC data which will be further discussed in Section B.4. Figure B.1.7 illustrates the reference UTM zone that was selected for this section. Mapping of the test grid with a handheld GPS rover is depicted in Figure B.1.8.

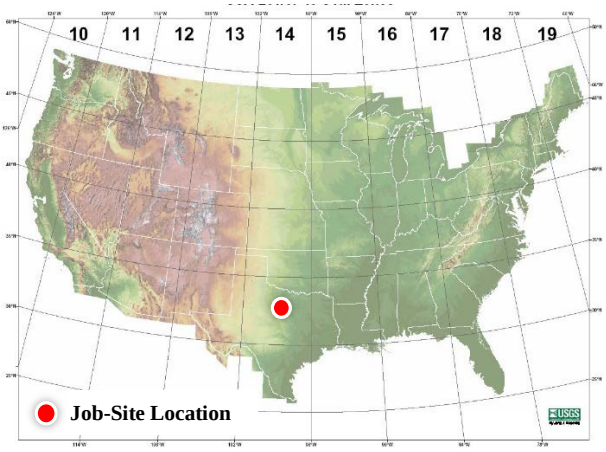

Figure B.1.7. The coordinate reference system for GPS devices

Figure B.1.8. Mapping the test section on compacted soil layer using a local base station

B.2. LABORATORY RESULTS

Index properties of the embankment and subgrade materials are summarized in Table B.2.1. Gradation curves of these geomaterials are depicted in Figure B.2.1. The embankment and subgrade material were classified as low-plasticity clay as per USCS. The optimum moisture content and maximum dry unit weight obtained as per modified Proctor tests (AASHTO T99) are also reported in Table B.2.1.

Table B.2.1. Index properties of embankment and subgrade materials

Gradation %				USCS Class.	Specific Gravity	Atterberg Limits			Moisture/Density	
Gravel	Coarse Sand	Fine Sand	Fines			LL	PL	PI	OMC, %	MDUW,** pcf
4	8	17	71	CL	2.74	34	10	24	18.3	109.2

*OMC = Optimum Moisture Content, **MDUW = Maximum Dry Unit Weight

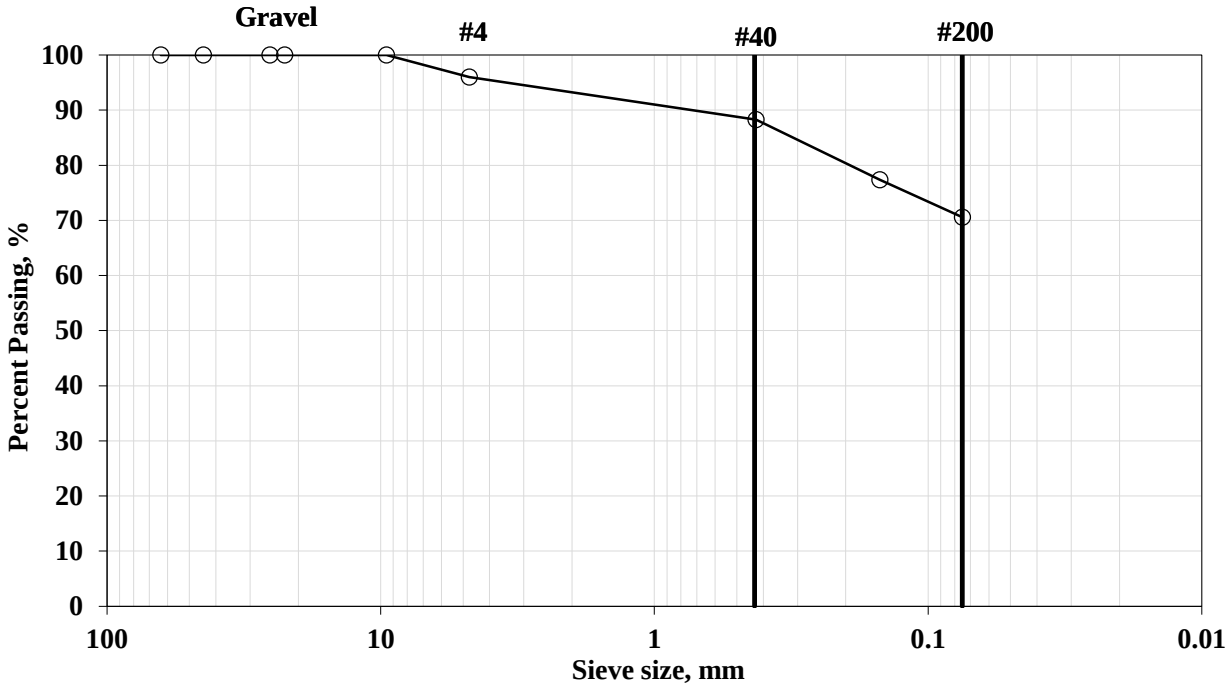

Figure B.2.1. Gradation curves of embankment and subgrade geomaterials

The resilient modulus (MR) and free-free resonant column (FFRC) tests were performed on laboratory specimens prepared at the optimum moisture content as summarized in Table B.2.2.

Table A.2.2 - Laboratory Results of MR and FFRC Tests of Geomaterials

Site	Type	Target Moisture Content	Actual Moisture Content, %	Dry Density, pcf	FFRC Modulus, ksi	Representative Resilient Modulus, ksi
Texas	Subgrade	18.3	18.1	109.1	13.7	2.49
Texas	Subgrade	18.3	18.7	110.3	15.8	3.73

B.3. EVALUATION OF MODULUS/STIFFNESS DEVICES

As noted earlier, three modulus-based devices (PSPA, LWD and DCP) were primarily used to estimate the modulus/stiffness of the test grid. The variation of moduli along the test section for different devices are summarized in Figure B.3.1. The modulus at each station in this figure represents the average of the spot tests on the three lines (A, B and C). The standard deviation of the moduli at each station are also depicted as error bars.

The spatial distribution of the moduli from the spot tests on the embankment layer are summarized in Figure B.3.2. PSPA and DCP are layer-specific devices and they reflect the properties of the layer of interest instead of a composite modulus. However, the range of estimated moduli are different since PSPA measures the linear elastic low-strain modulus of the underlying layer while DCP results are based on penetration of a cone and relates the penetration index to CBR (as per ASTM D6951) to further estimate the modulus utilizing experimental relationships (in this study, the equation recommend by TRRL was used to correlate CBR and modulus). Comparing Figures B.3.1 and B.3.3, both demonstrate a less stiff area in the middle of the section. The Quantile method was employed to classify the moduli into three classes represented as red, yellow and green colors. The results of the spot tests will be correlated with the collected IC data in the following sections.

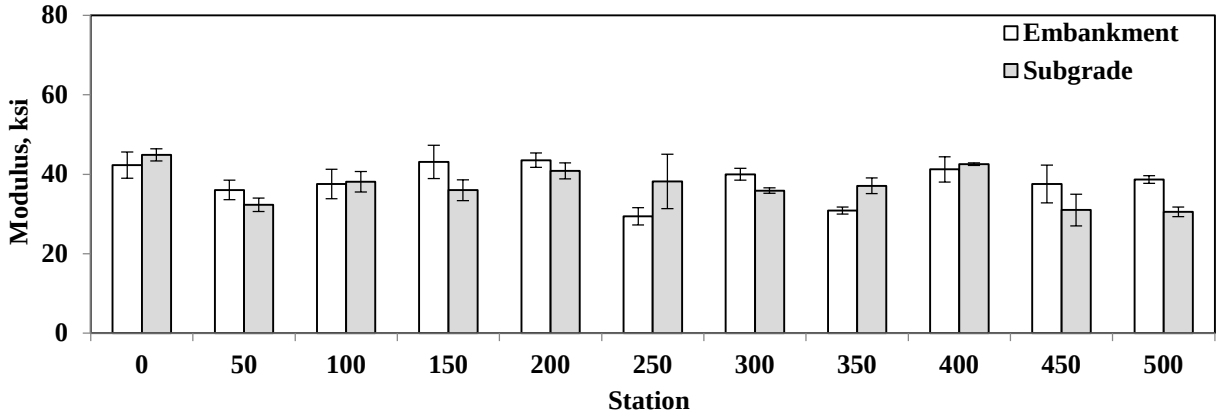

Figure B.3.1. Variation of PSPA modulus along the test section

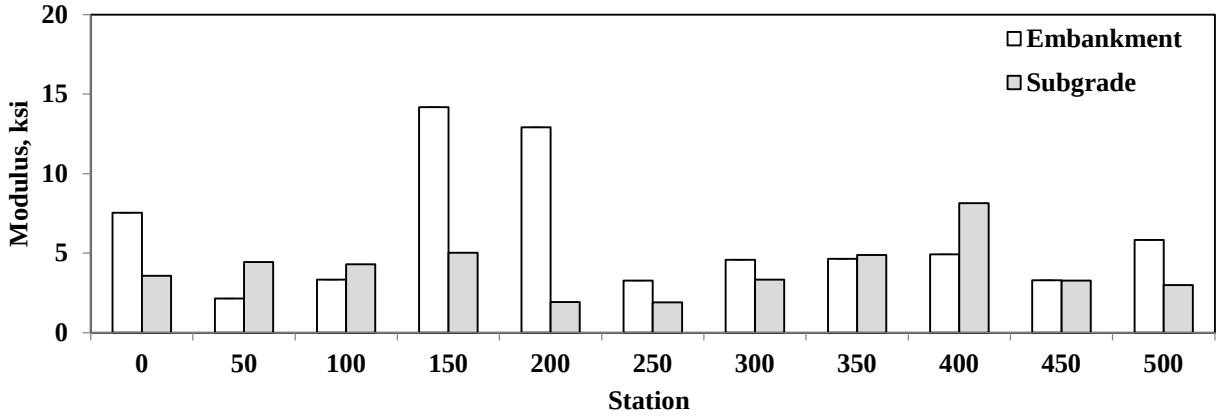

Figure B.3.2. Variation of Zorn LWD modulus along the test section

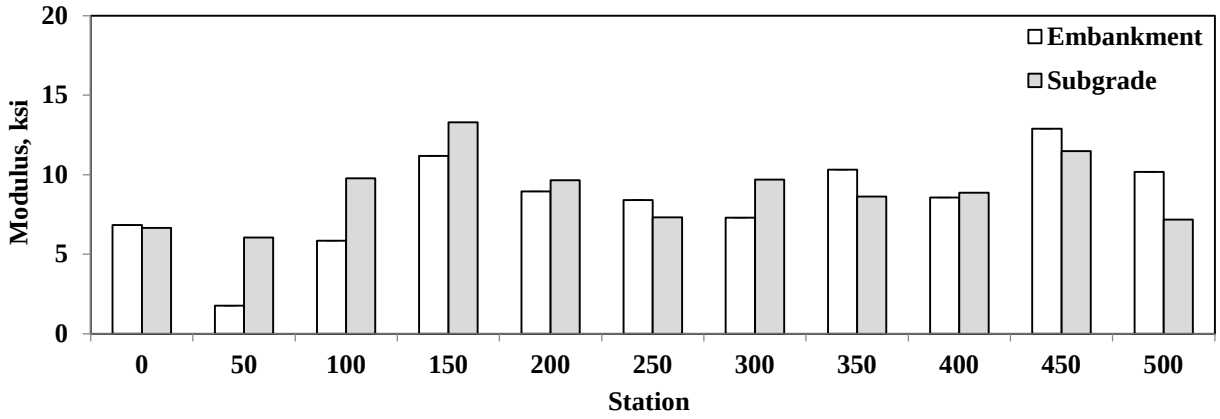

Figure B.3.3. Variation of DCP modulus along the test section

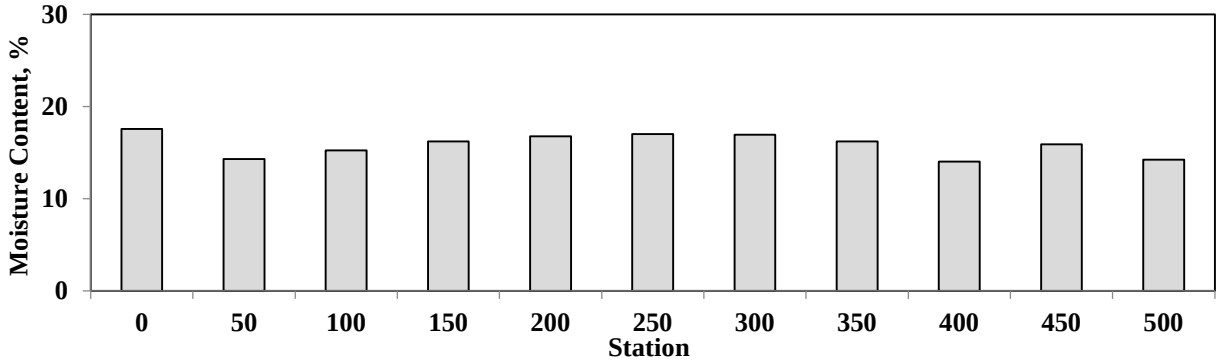

Figure B.3.4. Variation of oven-dry moisture content along the test section (subgrade layer)

Figure B.3.5. Spatial variation of PSPA modulus on embankment layer

Figure B.3.6. Spatial variation of LWD modulus on embankment layer

Figure B.3.7. Spatial variation of DCP modulus on embankment layer

Figure B.3.8. Spatial variation of PSPA modulus on subgrade layer

Figure B.3.9. Spatial variation of LWD modulus on subgrade layer

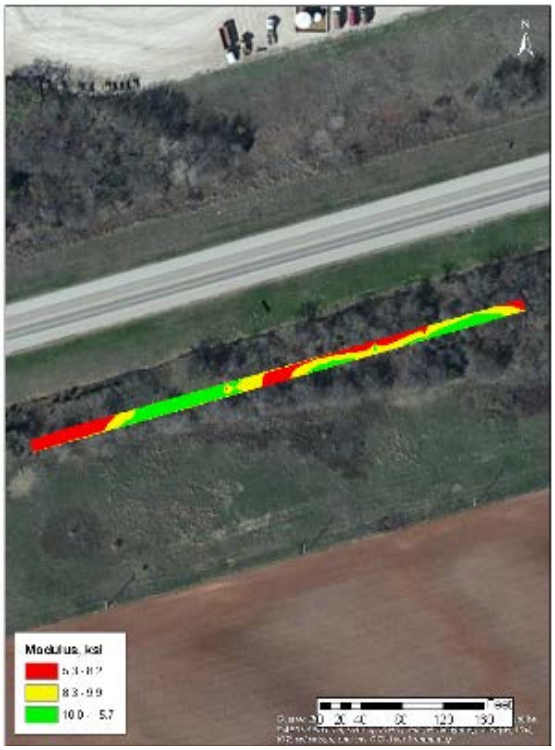

Figure B.3.10. Spatial variation of DCP modulus on subgrade layer

B.4. INTELLIGENT COMPACTION DATA COLLECTION

Three roller vendors (CAT, HAMM and SAKAI) were participated in this equipment rodeo. Texas virtual reference system (VRS) was used as the reference station to calibrate all the GPS devices used by the OEM and retrofit systems. As a part of the data acquisition system, two 3D geophones were embedded at depths of 24 in. and 48 in. from the existing embankment surface. The existing embankment section was pre-mapped with the three rollers prior to placement and compaction of the subgrade layer. The following sections include the results of the pre-mapping process as well as the data collected from the validation system during the stationary and moving vibration tests.

B.4.1. Pre-Mapping of Existing Embankment Layer

Partial coverage of the test section during the pre-mapping process was performed on the first day of operation by the CAT roller. Figures B.4.1 illustrates the spatial distribution of CMVs from the smooth drum CAT roller during the partial pre-mapping process with respect to the test section and location of the spot tests. Figure B.4.2 shows the distribution of the CMVs during the same operation. The average CMV was 27 with a COV of 48%.

The pre-mapping of the existing layer was continued during the second day of field operation. Figures B.4.3 through B.4.5 illustrate the spatial distribution of the CMVs from the retrofit systems installed on the HAMM and SAKAI rollers as well as the CMVs collected with the CAT smooth drum roller. The histograms of the CMVs are summarized in Figures B.4.6 through B.4.8.

Figures B.4.9 and B.4.10 illustrate the spatial distributions of the stiffness data from the retrofit and OEM systems on the HAMM roller. Due to some technical issues with the OEM system, only partial IC data was collected from the HAMM OEM system (see Figure B.4.10). Therefore, a comprehensive comparison of these two systems is not available for this compaction process. Figures B.4.11 and B.4.12 summarize the distributions of the CMV and HMV data for the HAMM roller during the second day of pre-mapping.

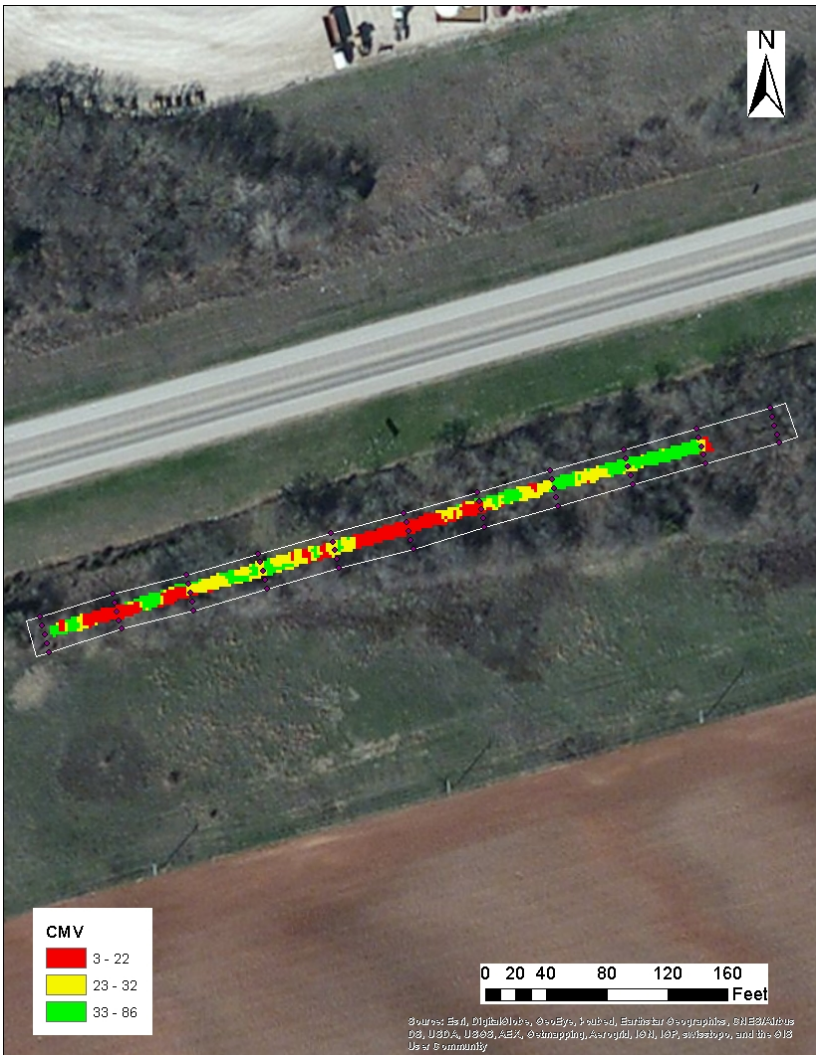

Figure B.4.1. Spatial distribution of CMV data from CAT smooth drum roller during pre-mapping (day 1)

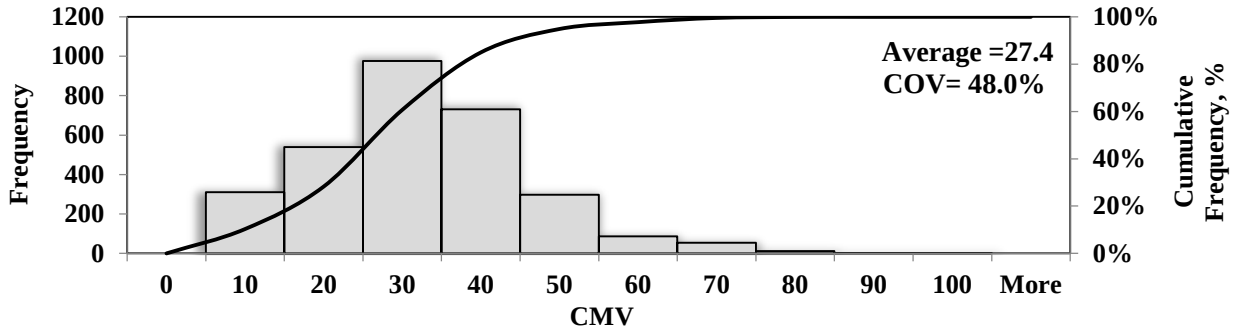

Figure B.4.2. Distribution of CMV data from CAT smooth drum during pre-mapping (day 1)

Figure B.4.3. Spatial variation of CMV data from HAMM Retrofit system during pre-mapping (day 2)

Figure B.4.4. Spatial variation of CMV data from SAKAI Retrofit system during pre-mapping (day 2)

Figure B.4.5. Spatial variation of CMV data from CAT smooth drum roller during pre-mapping (day 2)

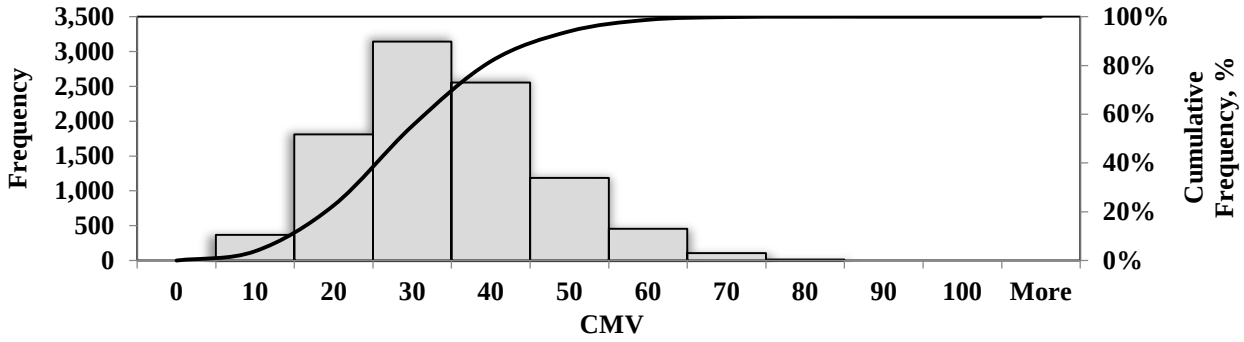

Figure B.4.6. Distribution of CMV data from HAMM retrofit system during pre-mapping (day2)

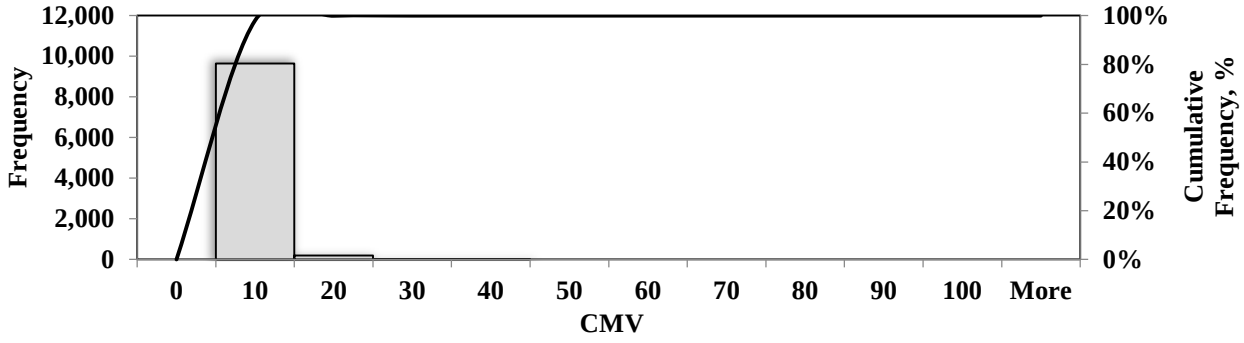

Figure B.4.7. Distribution of CMV data from SAKAI retrofit system during pre-mapping (day2)

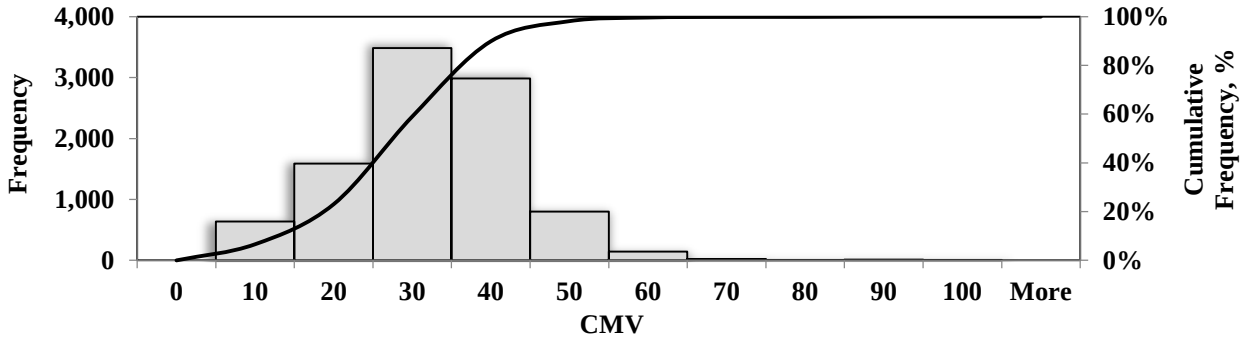

Figure B.4.8. Distribution of CMV data from CAT smooth drum roller during pre-mapping (day2)

The same comparison process was performed for the SAKAI roller in Figures B.4.13 through B.4.16. Figures B.4.17 through B.4.22 summarize the averages and coefficients of variation of the CMV data from the two retrofit systems on the SAKAI and HAMM rollers and the CMVs from the CAT roller.

Figure B.4.9. Spatial variation of CMV data from HAMM retrofit system during pre-mapping (day2)

Figure B.4.10. Spatial variation of HMV data from HAMM OEM system during pre-mapping (day 2)

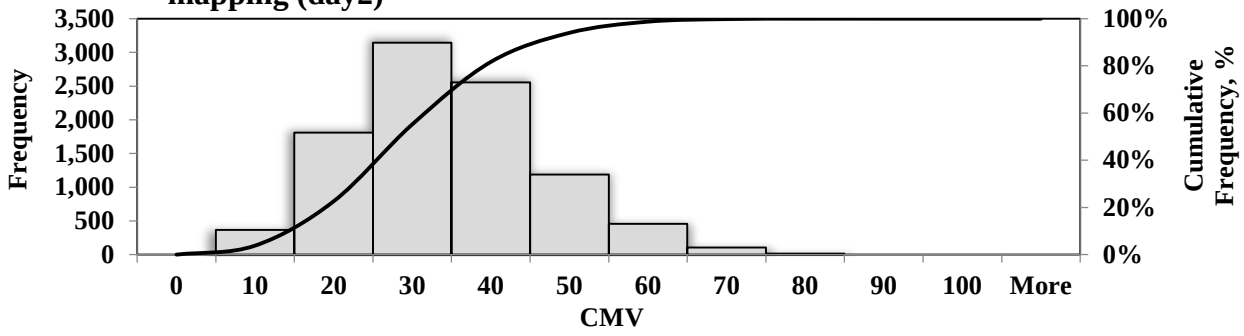

Figure B.4.11. Distribution of CMV data from HAMM retrofit system during pre-mapping (day 2)

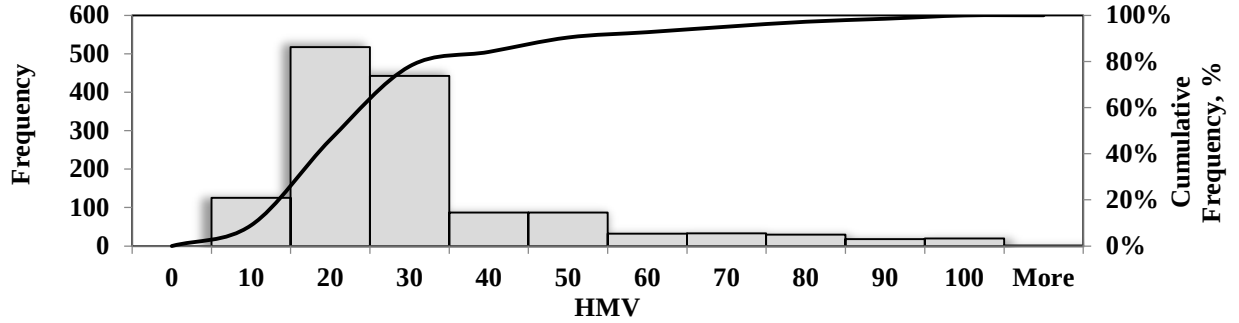

Figure B.4.12. Distribution of HMV data from HAMM OEM system during pre-mapping (day 2)

Figure B.4.13. Spatial variation of CMV data from SAKAI retrofit system during pre-mapping (day 2)

Figure B.4.14. Spatial variation of CCV data from SAKAI OEM system during pre-mapping (day 2)

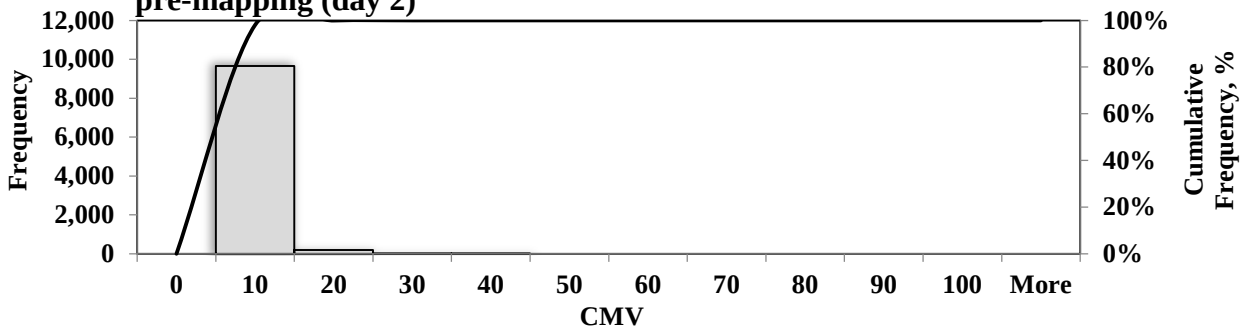

Figure B.4.15. Distribution of CMV data from SAKAI retrofit system during pre-mapping (day 2)

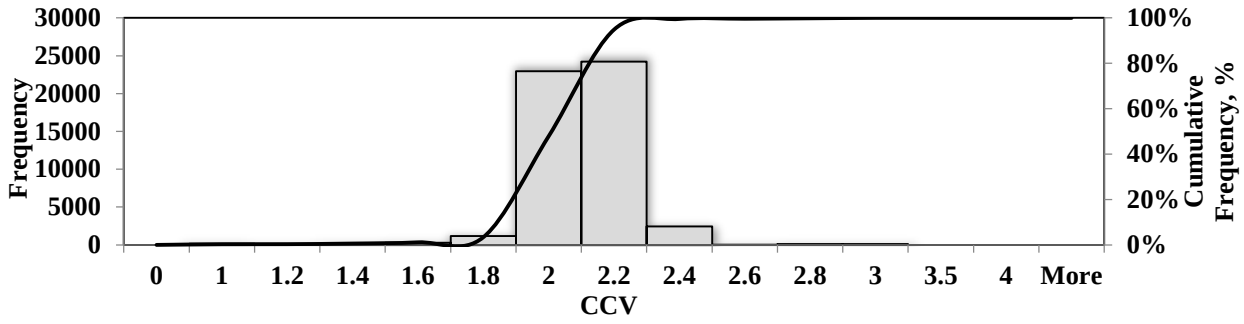

Figure B.4.16. Distribution of CCV data from SAKAI OEM system during pre-mapping (day 2)

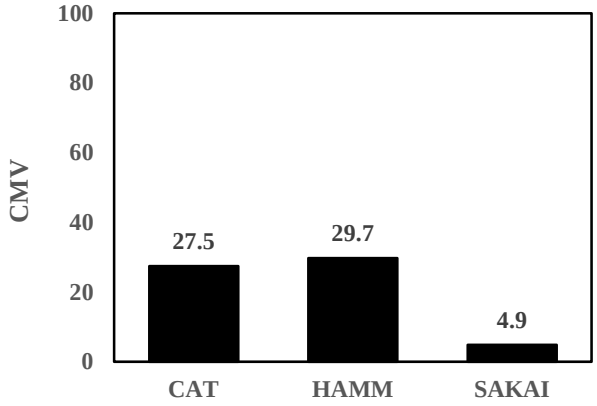

Figure B.4.17. Average of CMVs for three rollers during pre-mapping

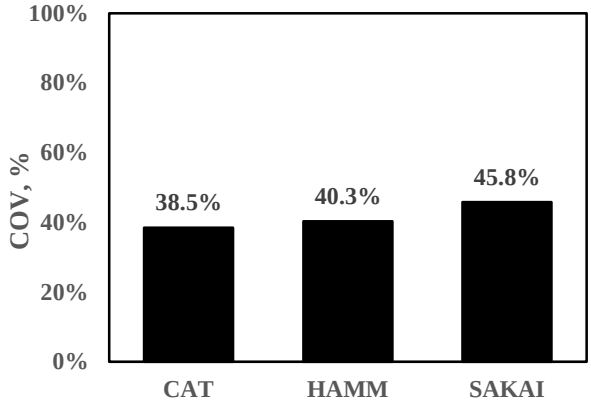

Figure B.4.18. Coefficient of variation of CMVs for three rollers during pre-mapping

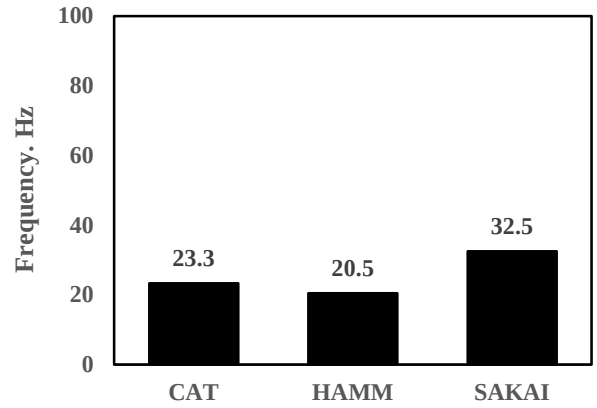

Figure B.4.19. Average of vibration frequency for three rollers during pre-mapping

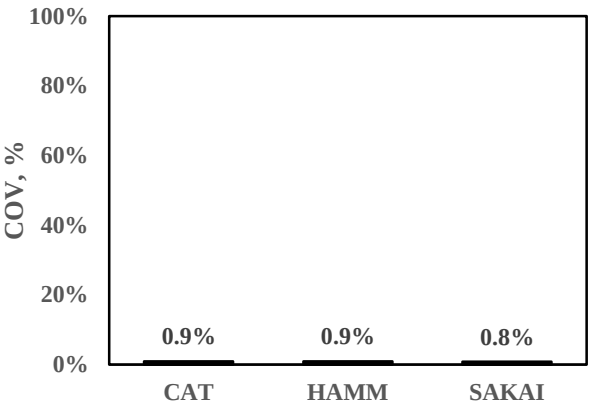

Figure B.4.20. Coefficient of variation of vibration frequency for three rollers during pre-mapping

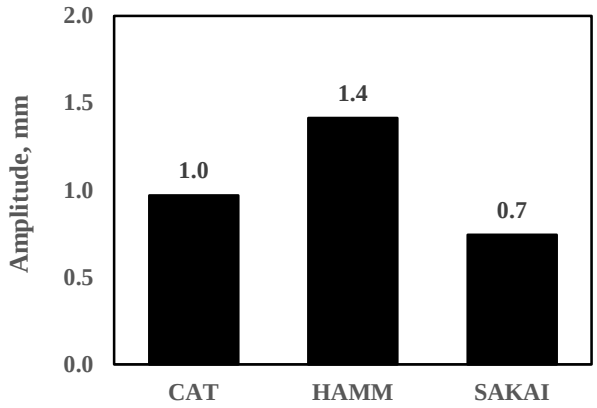

Figure B.4.21. Average of vibration amplitude for three rollers during pre-mapping

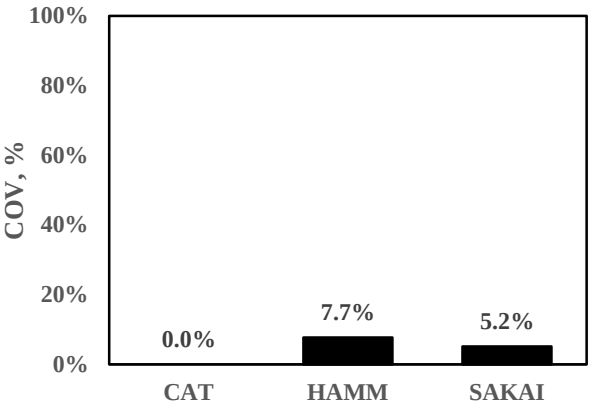

Figure B.4.22. Coefficient of variation of vibration amplitude for three rollers during pre-mapping

B.4.2. Compaction and Mapping of Subgrade Layer

Prior to the placement of the subgrade layer, a less stiff area was created toward the northeastern edge of the test section using a grader. The goal of creating a less stiff area was to assess the ability of different IC systems on different rollers to identify it during the compaction process. The clayey subgrade layer was placed on the existing layer on the third day of the operation. The moist materials were spread with a grader and then the CAT roller with the sheepfoot pad was employed to compact the subgrade layer. After the compaction with the padfoot roller, the subgrade layer was mapped using both the HAMM and SAKAI smooth drum rollers. Figures B.4.23 through B.4.25 illustrate the spatial variation of the CMVs from the retrofit systems on the HAMM and SAKAI rollers and from the padfoot CAT roller.

Figures B.4.26 through B.4.28 illustrate the distributions of the CMVs during the compaction of the subgrade layer with the three rollers. Due to some technical issues, the CMVs reported from the retrofit system on the SAKAI roller are lower than those reported with the HAMM roller.

Figures B.4.29 and B.4.30 compare the CMV data from the retrofit system on the HAMM roller with the OEM data in terms of HMV. Since the process of calculating both CMV and HMV are similar (using Equation 2.1.1), the ranges of these two indices as further compared in Figures B.4.31 and B.4.32 in the form of histograms are reasonably similar.

Figures B.4.33 and B.4.34 illustrate the CMV and CCV data collected with the SAKAI retrofit and OEM systems, respectively.

Figures B.4.37 through B.4.42 summarize the averages and coefficients of variation for the CMVs and vibration amplitude and frequencies from the two retrofit systems on the SAKAI and HAMM rollers with the ones captured from the CAT roller. Again, the CMVs from the retrofit system on the SAKAI roller seem to be a constant number due to some technical difficulties of the system.

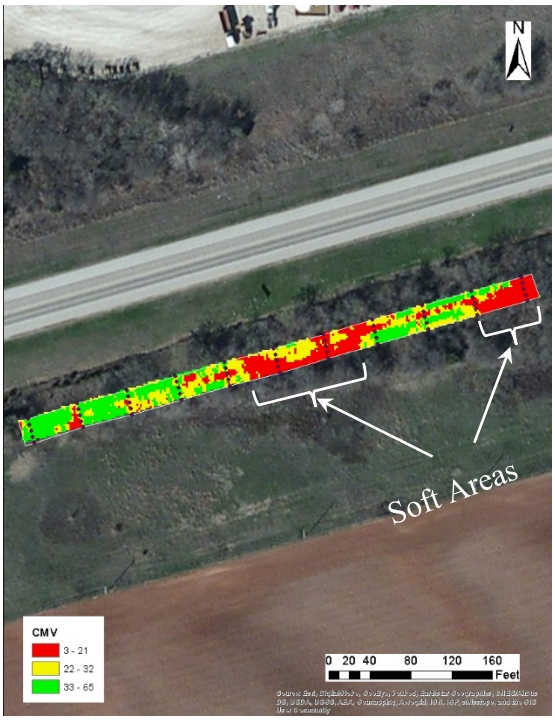

Figure B.4.23. Spatial variation of CMV data from HAMM Retrofit system during mapping of subgrade layer (day 3)

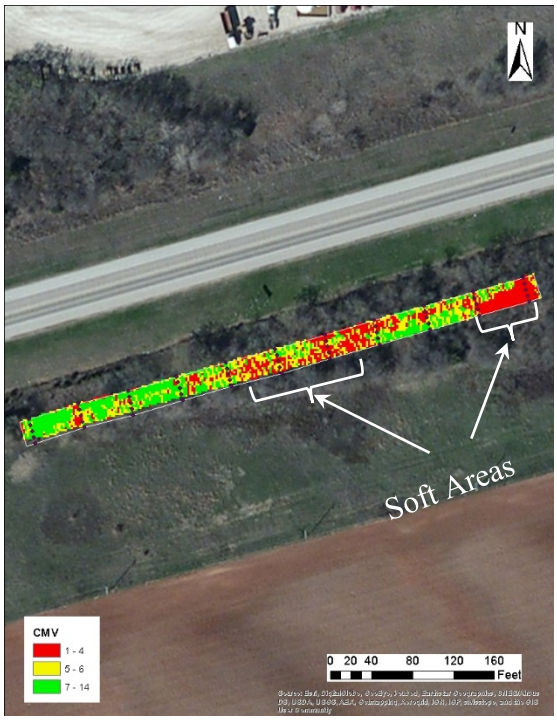

Figure B.4.24. Spatial variation of CMV data from SAKAI Retrofit system during mapping of subgrade layer (day 3)

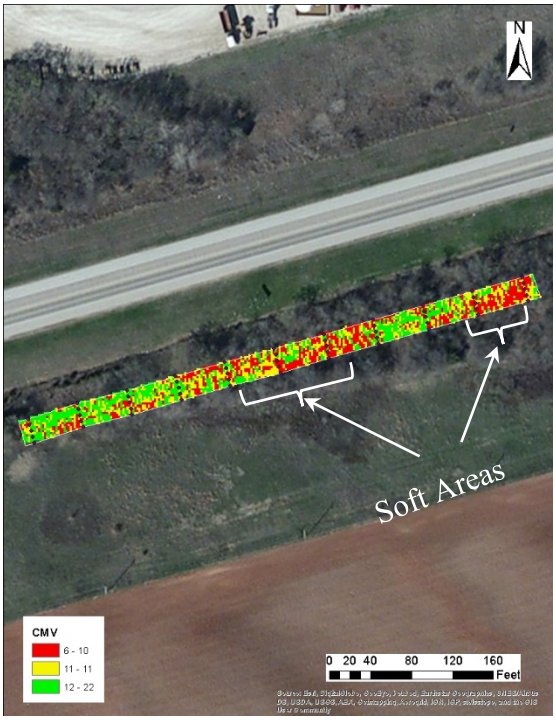

Figure B.4.25. Spatial variation of CMV data from CAT padfoot roller during compaction of subgrade layer (day 3)

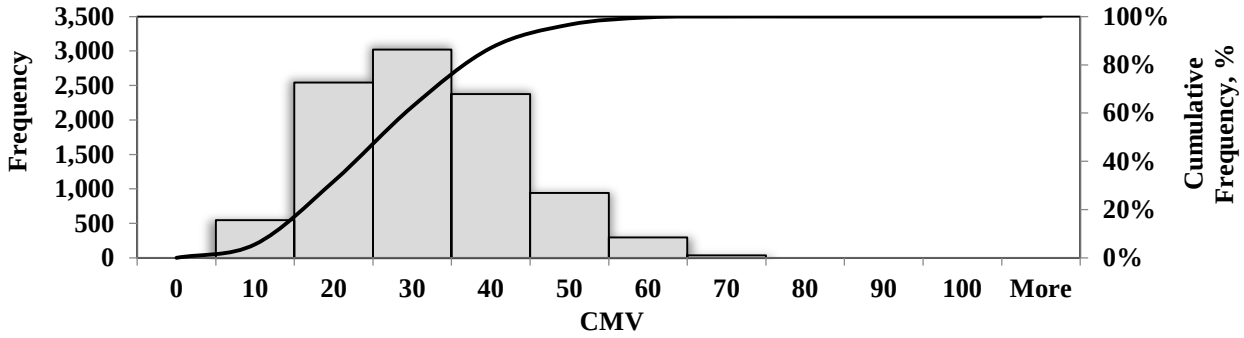

Figure B.4.26. Distribution of CMV data from HAMM Retrofit system during mapping of subgrade layer

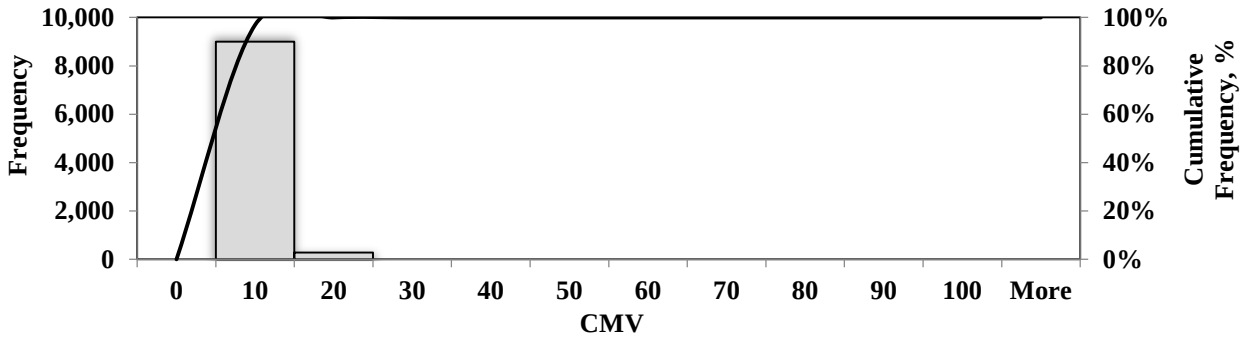

Figure B.4.27. Distribution of CMV data from SAKAI Retrofit system during mapping of subgrade layer

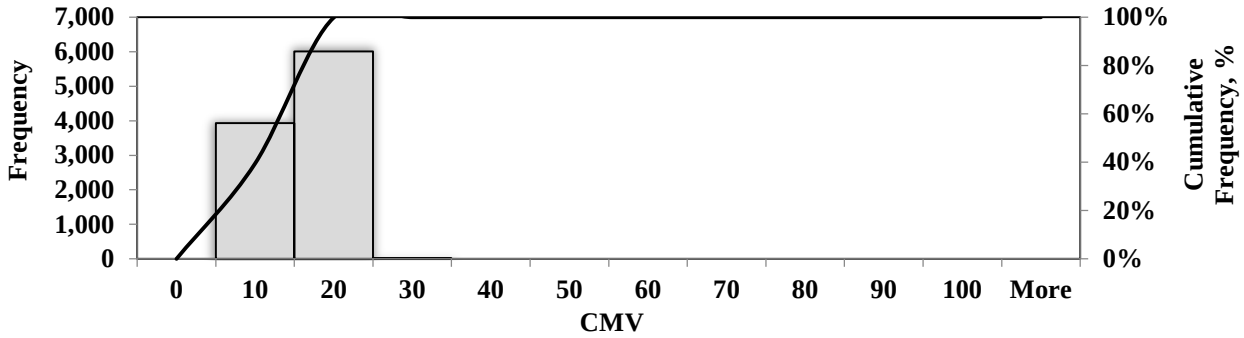

Figure B.4.28. Distribution of CMV data from CAT padfoot roller during compaction of subgrade layer

Figure B.4.43 shows the spatial variation of the CMVs from the CAT smooth drum roller on compacted subgrade layer during the last day of operation (about 18 hours after the compaction of the subgrade layer). Figure B.4.44 illustrates the histogram of the CMVs during the same operation.

Figure B.4.29. Spatial variation of CMV data from HAMM retrofit system during mapping of subgrade layer

Figure B.4.30. Spatial variation of HMV data from HAMM OEM system during mapping of subgrade layer

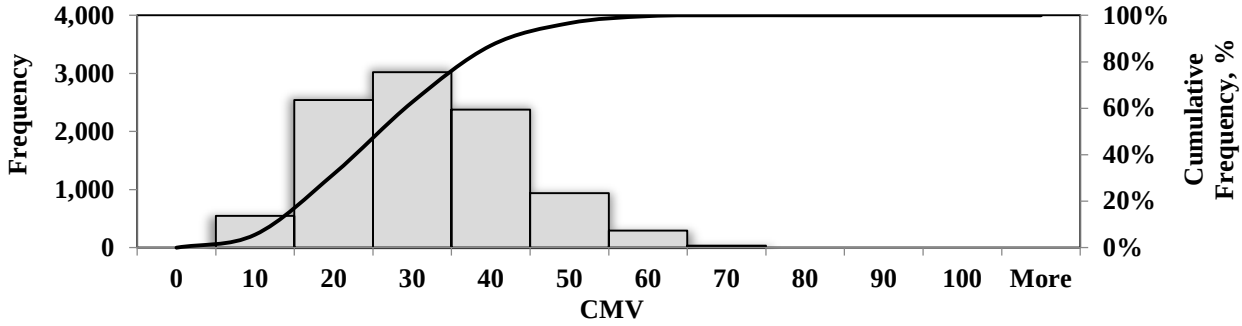

Figure B.4.31. Distribution of CMV data from HAMM retrofit system during mapping of subgrade layer

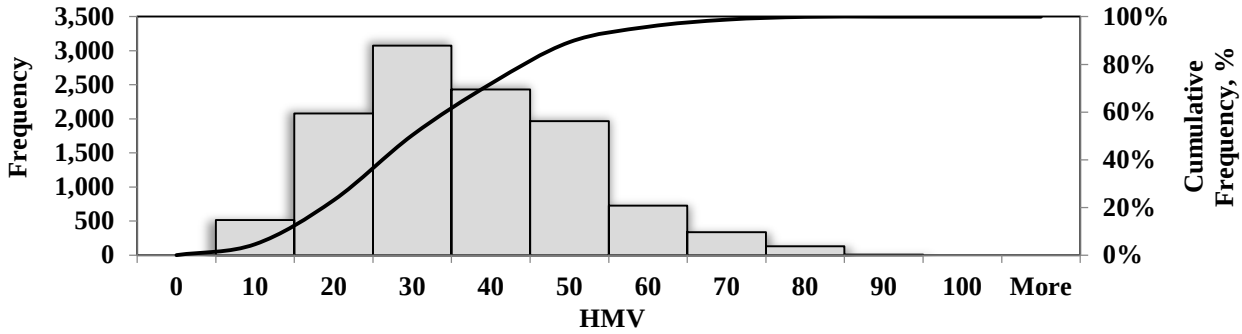

Figure B.4.32. Distribution of HMV data from HAMM OEM system during mapping of subgrade layer

Figure B.4.33. Spatial variation of CMV data from SAKAI retrofit system during mapping of subgrade layer

Figure B.4.34. Spatial variation of CCV data from SAKAI OEM system during mapping of subgrade layer

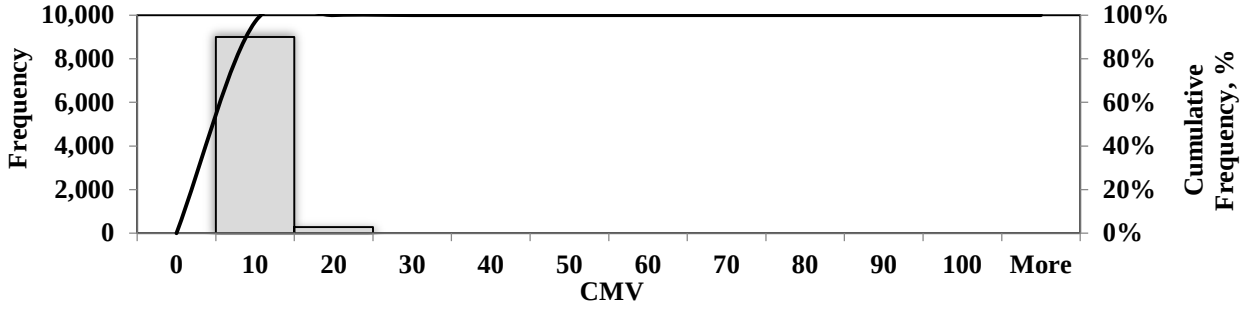

Figure B.4.35. Distribution of CMV data from SAKAI retrofit system during mapping of subgrade layer

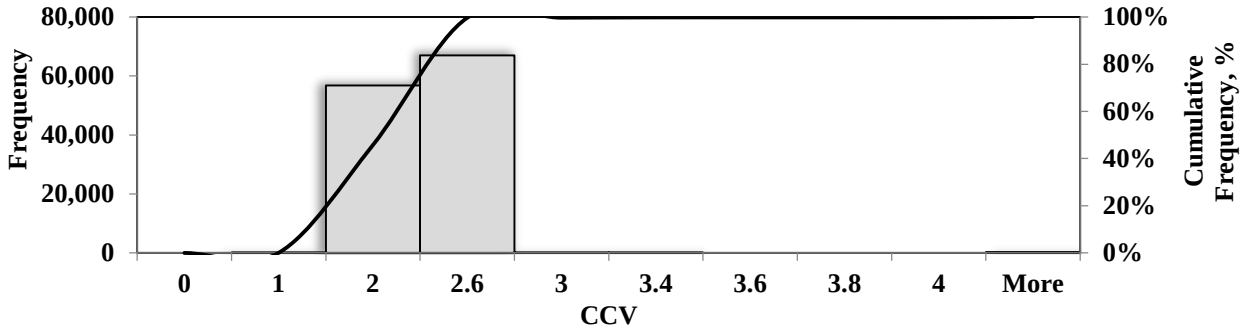

Figure B.4.36. Distribution of CCV data from SAKAI OEM system during mapping of subgrade layer

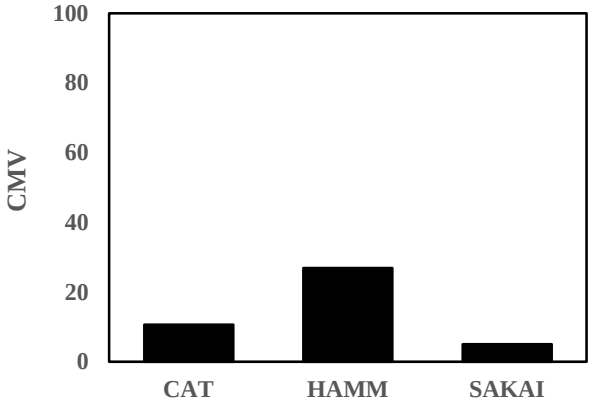

Figure B.4.37. Average of CMVs for three rollers during compaction and mapping of subgrade layer

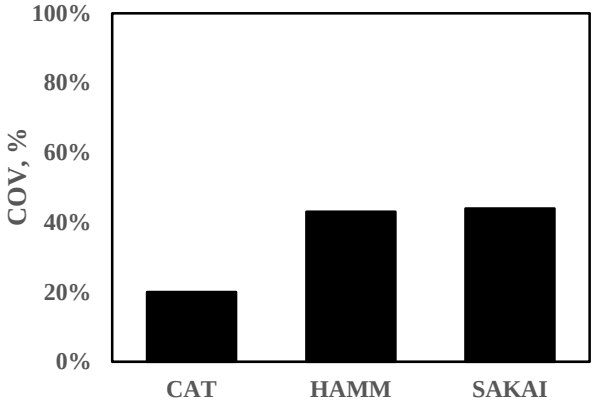

Figure B.4.38. Coefficient of variation of CMVs for three rollers during compaction and mapping of subgrade layer

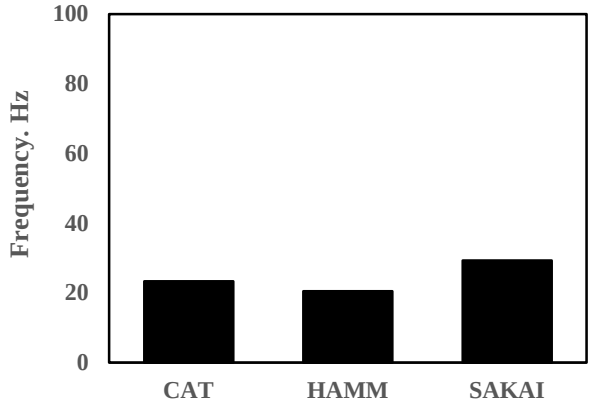

Figure B.4.39. Average of vibration frequency for three rollers during compaction and mapping of subgrade layer

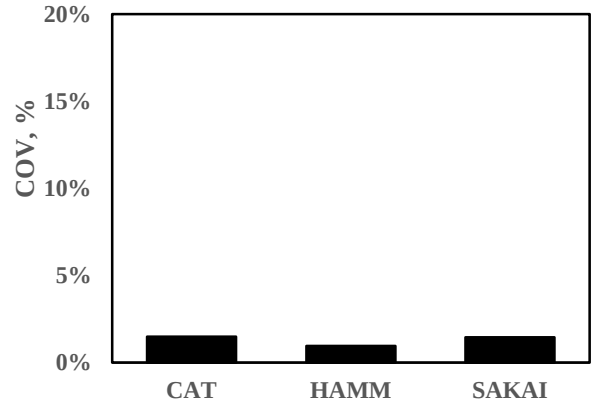

Figure B.4.40. Coefficient of variation of vibration frequency for three rollers during compaction and mapping of subgrade layer

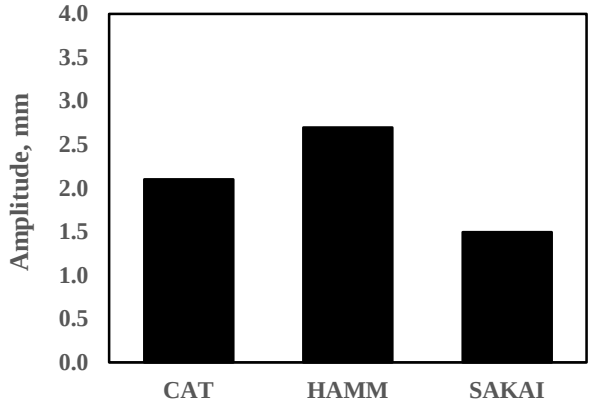

Figure B.4.41. Average of vibration amplitude for three rollers during compaction and mapping of subgrade layer

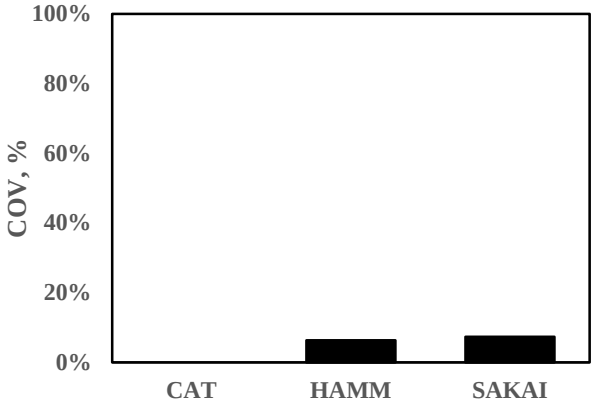

Figure B.4.42. Coefficient of variation of vibration amplitude for three rollers during compaction and mapping of subgrade layer

Figure B.4.43. Spatial variation of CMV data from CAT smooth drum roller during mapping of subgrade layer after 18 hrs (day 4)

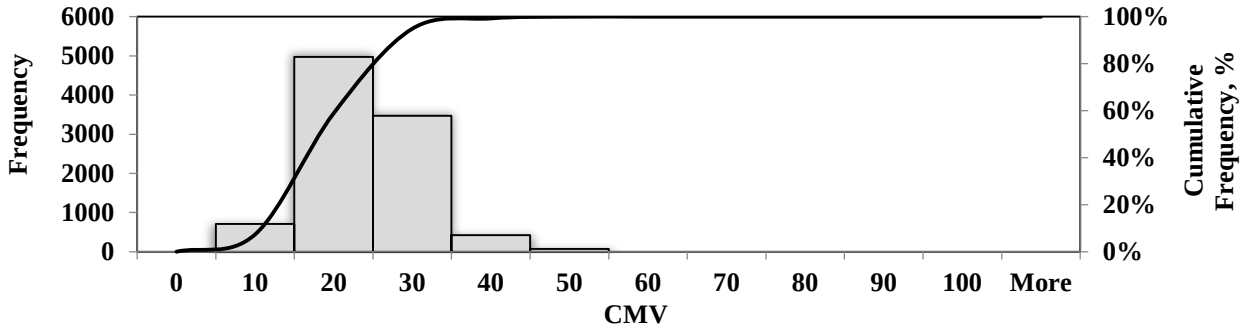

Figure B.4.44. Distribution of CMV data from CAT smooth drum roller during mapping of subgrade layer after 18 hrs (day 4)

B.5. VIBRATION DATA FROM VALIDATION SYSTEM

Figures B.5.1 through B.5.3 summarize the spectrograms of the vertical responses of the top geophone during the stationary tests with the CAT roller. The effects of the different vibration settings in terms of frequency and amplitude can be observed in these three figures.

Figures B.5.4 through B.5.7 illustrate the spectrograms of the vertical response from the top geophone during the stationary tests with the HAMM roller. The HAMM roller used three frequency settings of 1200, 1800 and 2400 vpm.

The stationary tests with the SAKAI roller were performed under two settings as summarized in Figures B.5.8 and B.5.9. Although both tests were performed at low frequency, the impact of the differences in the magnitudes of vibration cannot be observed in these two figures.

Figures B.5.10 through B.5.13 summarize the spectrograms of the vertical responses of the embedded geophone as well as the vibration responses of the mounted accelerometers during pre-mapping with the CAT roller on the existing embankment layer. The location of each pass within the test section as well as the direction of the roller movement are also shown in these figures. Two vibration settings as low amplitude-low frequency and high amplitude-low frequency were employed during these two passes.

Figures B.5.14 through B.5.17 summarize the spectrograms of vibration responses from the geophones and accelerometers during the pre-mapping with the HAMM roller. Again, two passes of the roller with the low-amplitude-low frequency and high amplitude-low frequency are shown in these figures. The hollow area in Figures B.5.14 and B.5.15 represent the time that the vibration was turned off due to some technical reasons and went back on after about 10 ft.

After the placement and compaction of the subgrade layer, the compacted layer was mapped with the instrumented SAKAI roller with different vibration settings. Figures B.5.18 through B.5.21 represent two passes of the SAKAI roller during the mapping of the subgrade layer at low-amplitude-low frequency and high amplitude-low frequency settings.

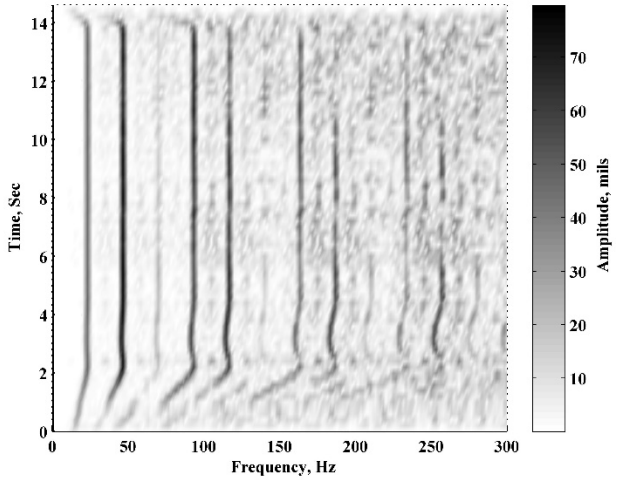

Figure B.5.1. Spectrogram of vertical response from the top geophone during stationary test (CAT roller) – high amplitude and low frequency

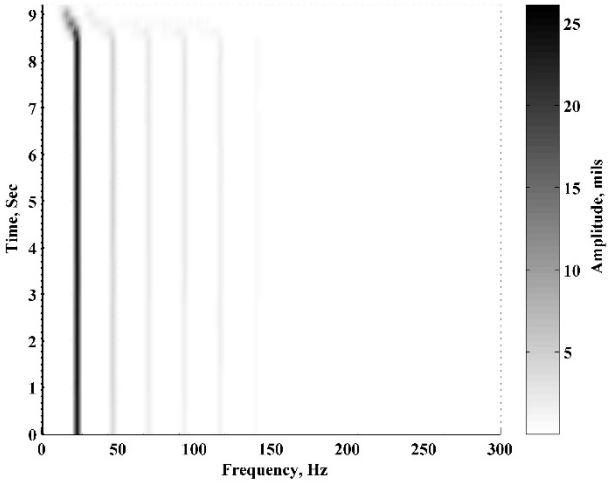

Figure B.5.2. Spectrogram of vertical response from the top geophone during stationary test (CAT roller) – low amplitude and low frequency

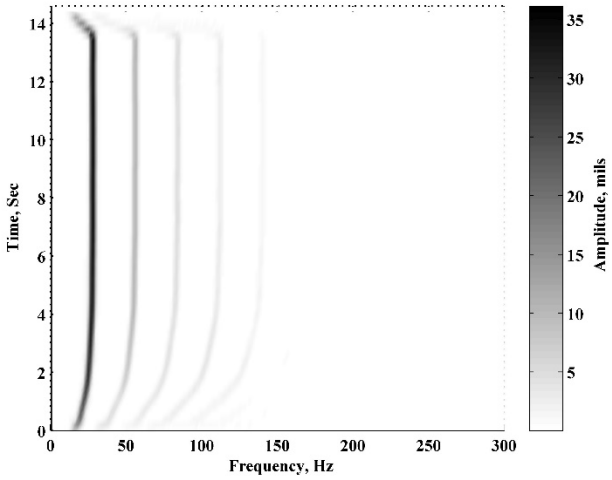

Figure B.5.3. Spectrogram of vertical response from the top geophone during stationary test (CAT roller) – low amplitude and high frequency

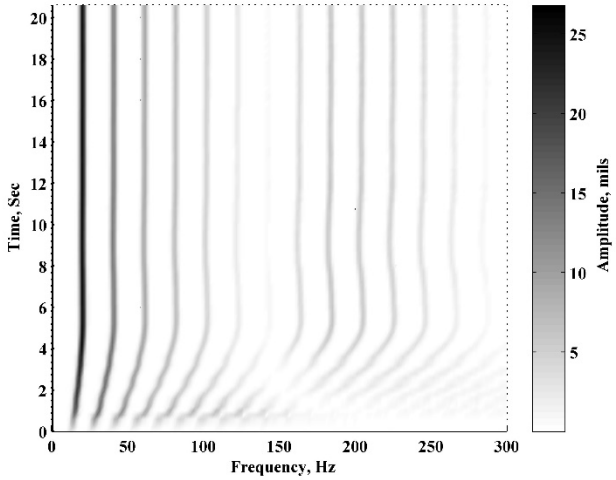

Figure B.5.4. Spectrogram of vertical response from the top geophone during stationary test (HAMM roller) – high amplitude and low frequency

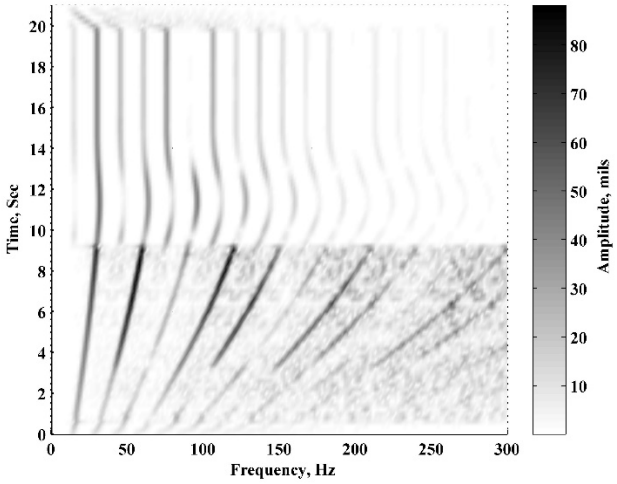

Figure B.5.6. Spectrogram of vertical response from the top geophone during stationary test (HAMM roller) – low amplitude and medium frequency

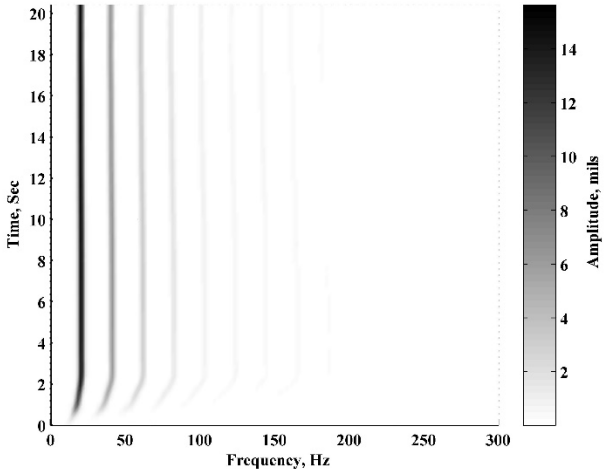

Figure B.5.5. Spectrogram of vertical response from the top geophone during stationary test (HAMM roller) – low amplitude and low frequency

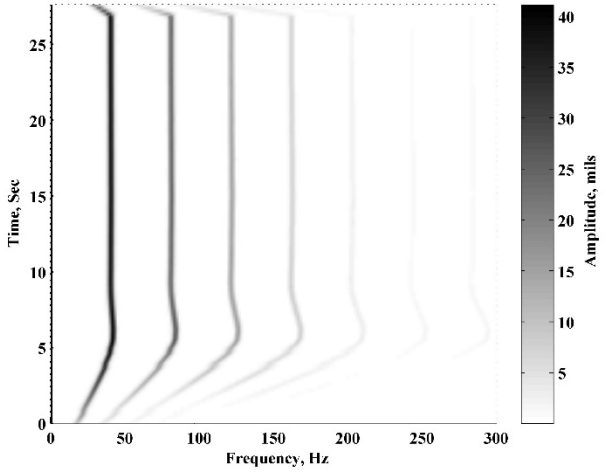

Figure B.5.7. Spectrogram of vertical response from the top geophone during stationary test (HAMM roller) – low amplitude and high frequency

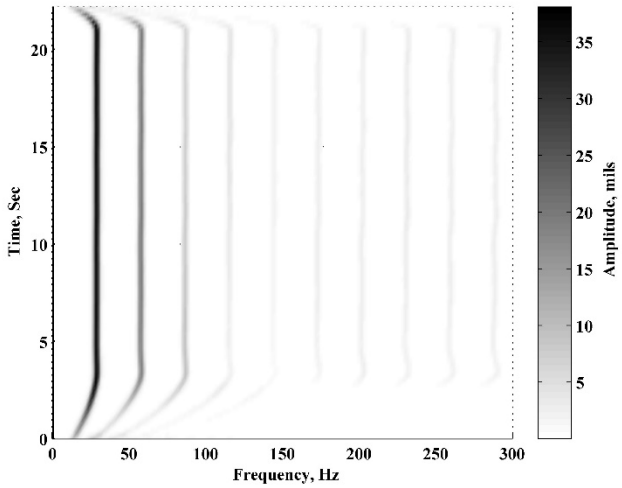

Figure B.5.8. Spectrogram of vertical response from the top geophone during stationary test (SAKAI roller) – high amplitude and low frequency

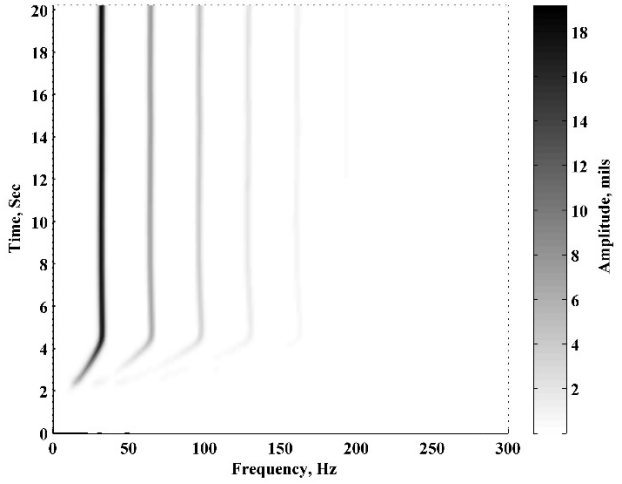

Figure B.5.9. Spectrogram of vertical response from the top geophone during stationary test (SAKAI roller) – low amplitude and low frequency

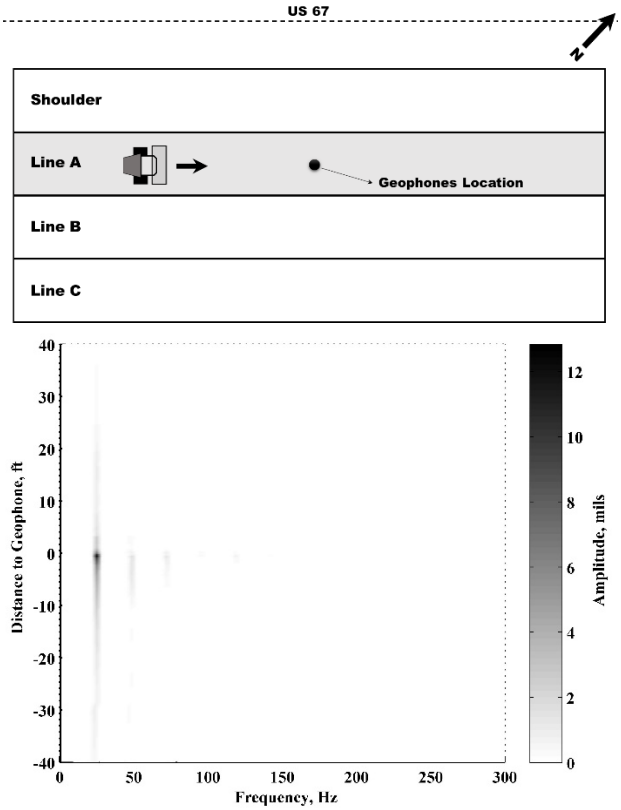

Figure B.5.10. Spectrogram of vertical response from the top geophone during moving test (CAT roller) – low amplitude and low frequency – pre-mapping

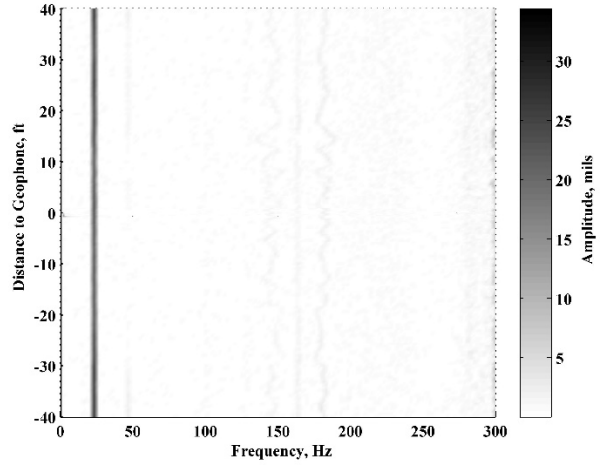

Figure B.5.11. Spectrogram of the vibration response from mounted accelerometer during moving test (CAT roller) – low amplitude and low frequency – pre-mapping

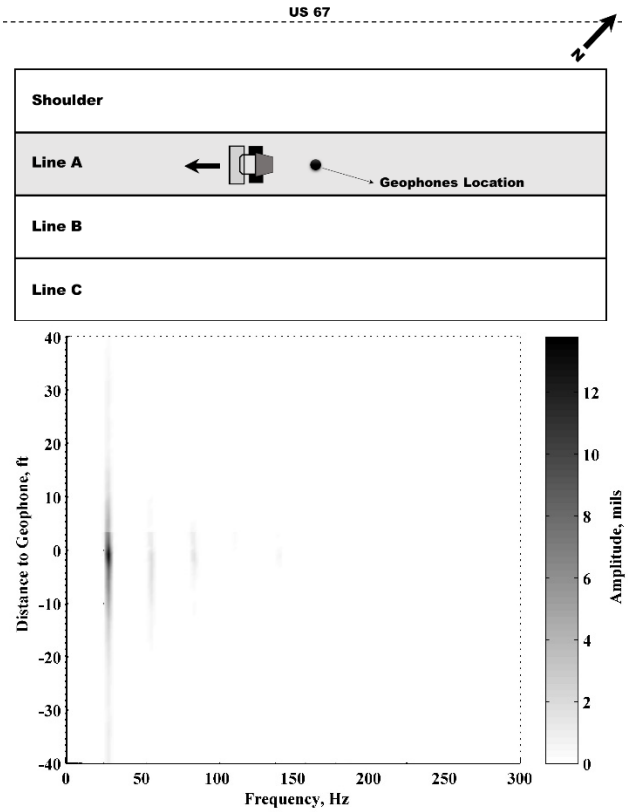

Figure B.5.12. Spectrogram of vertical response from the top geophone during moving test (CAT roller) – high amplitude and low frequency – pre-mapping

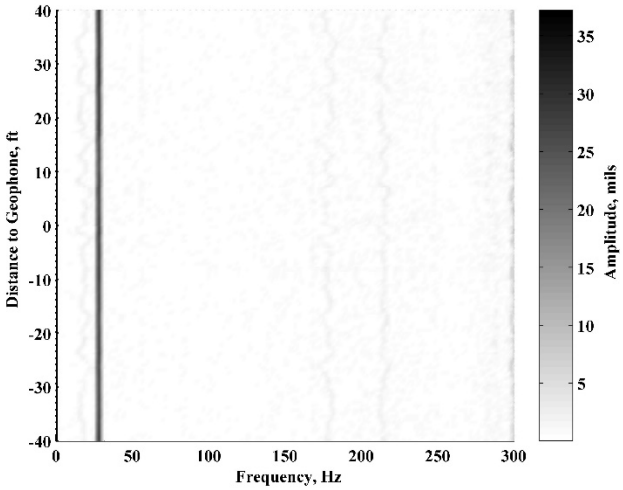

Figure B.5.13. Spectrogram of the vibration response from mounted accelerometer during moving test (CAT roller) – high amplitude and low frequency – pre-mapping

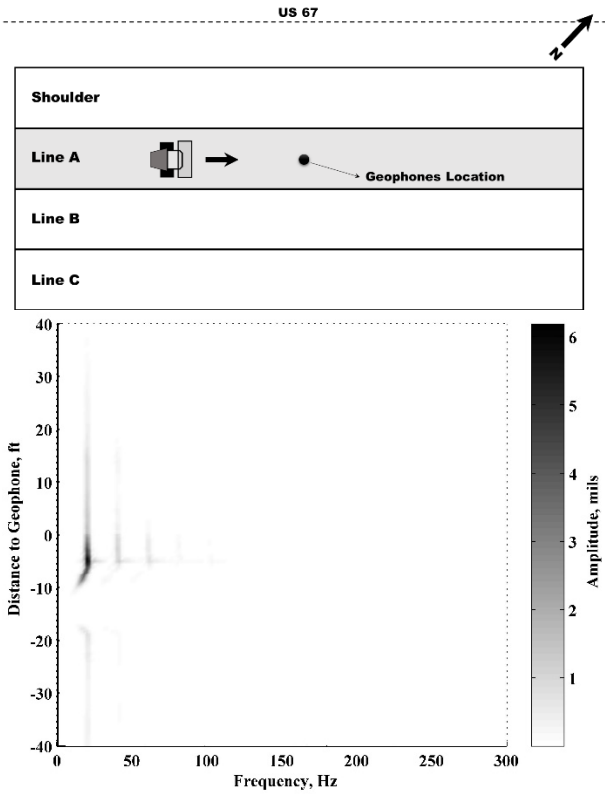

Figure B.5.14. Spectrogram of vertical response from the top geophone during moving test (HAMM roller) – low amplitude and low frequency – pre-mapping

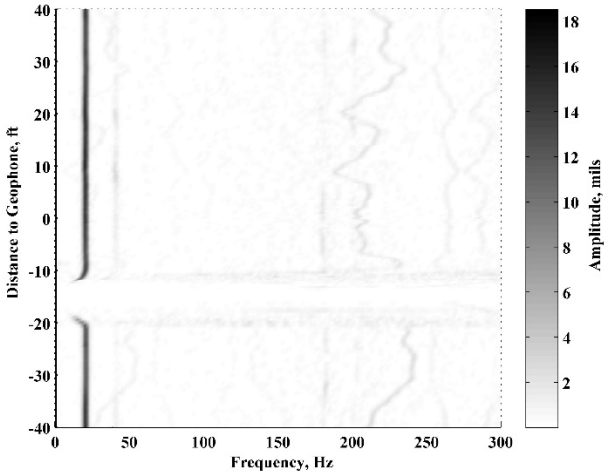

Figure B.5.15. Spectrogram of the vibration response from mounted accelerometer during moving test (HAMM roller) – low amplitude and low frequency – pre-mapping

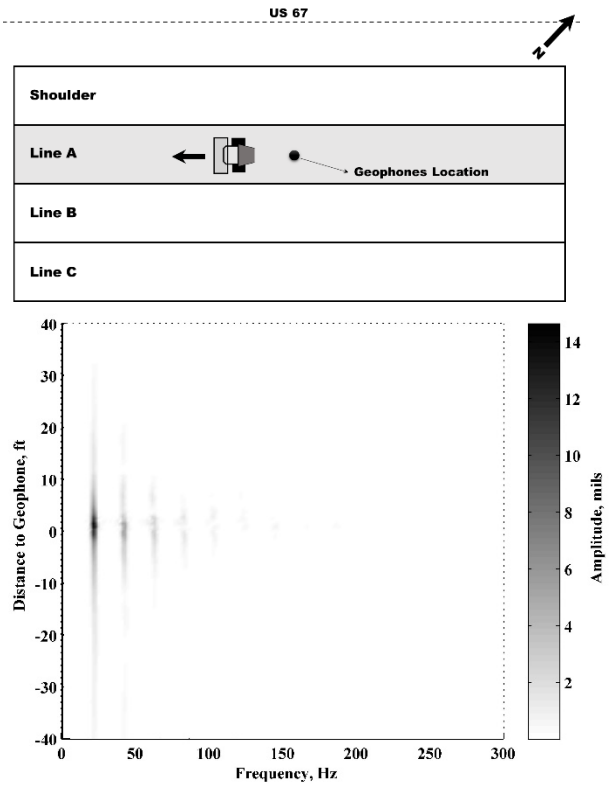

Figure B.5.16. Spectrogram of vertical response from the top geophone during moving test (HAMM roller) – high amplitude and low frequency – pre-mapping

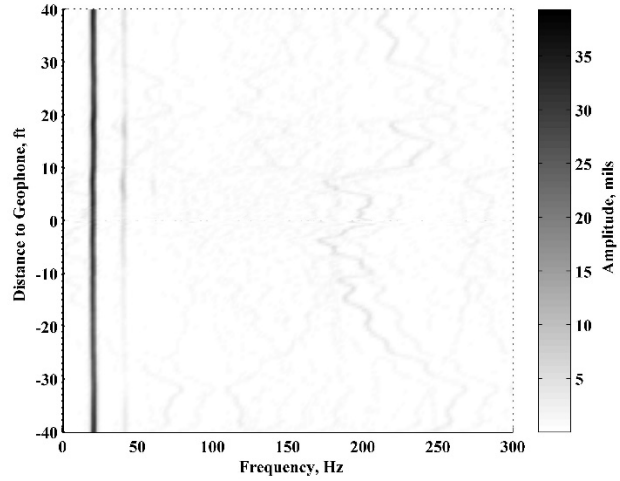

Figure B.5.17. Spectrogram of the vibration response from mounted accelerometer during moving test (HAMM roller) – high amplitude and low frequency – pre-mapping

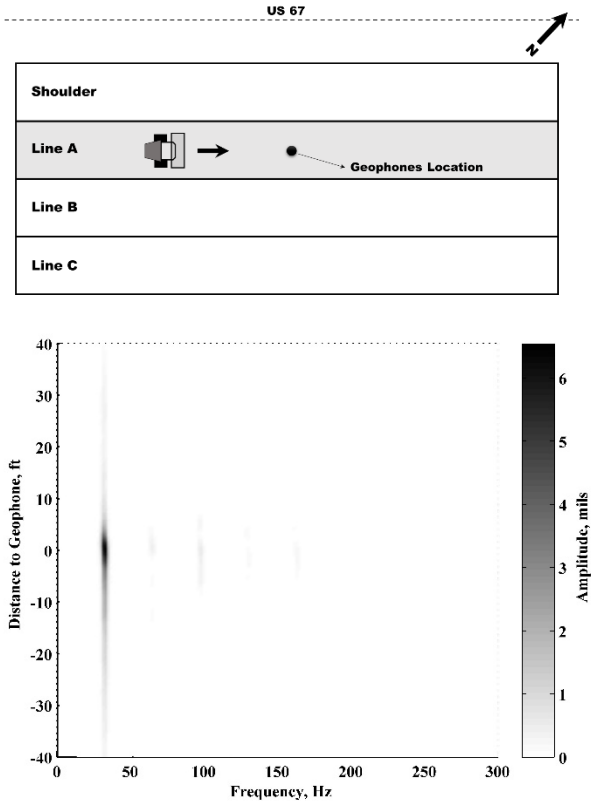

Figure B.5.18. Spectrogram of vertical response from the top geophone during moving test (SAKAI roller) – low amplitude and low frequency – mapping

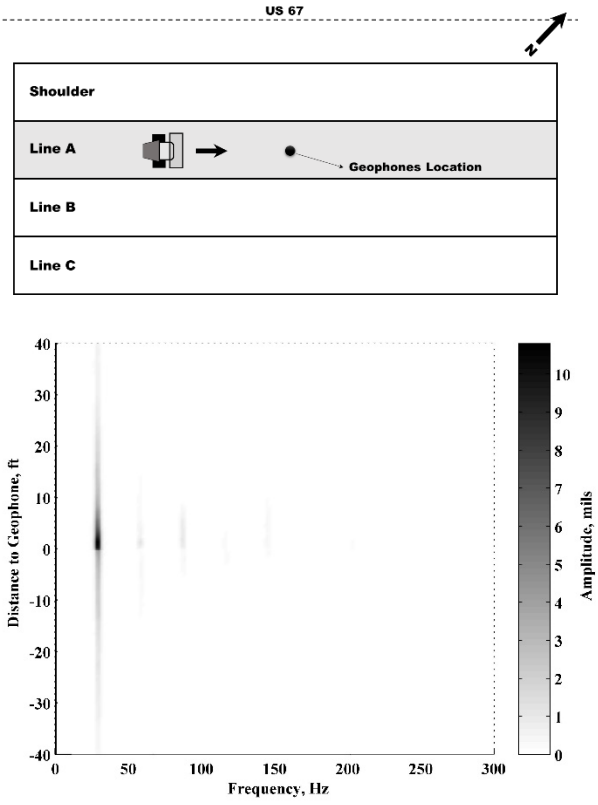

Figure B.5.20. Spectrogram of vertical response from the top geophone during moving test (SAKAI roller) – high amplitude and low frequency – mapping

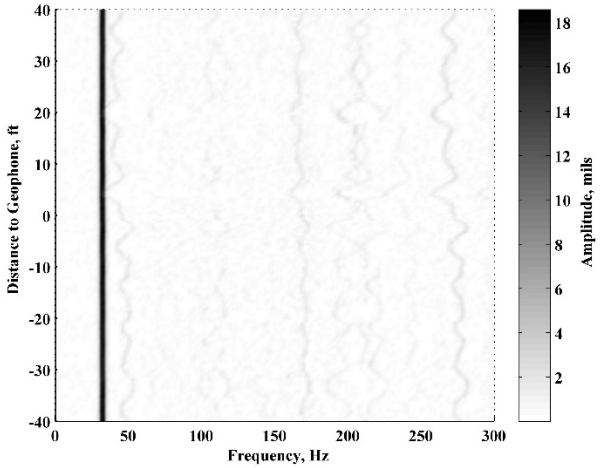

Figure B.5.19. Spectrogram of the vibration response from mounted accelerometer during moving test (SAKAI roller) – low amplitude and low frequency – mapping

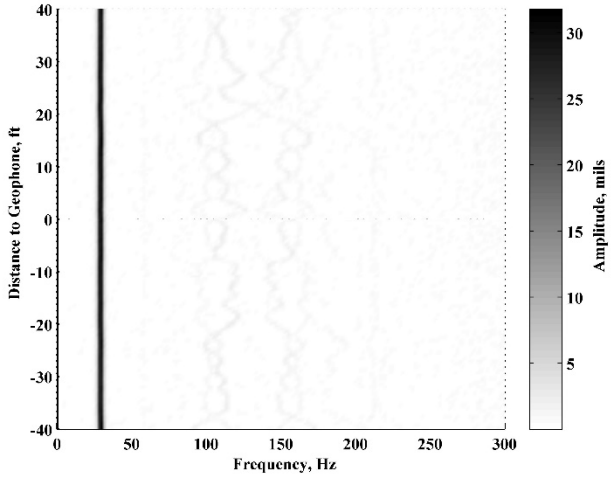

Figure B.5.21. Spectrogram of the vibration response from mounted accelerometer during moving test (SAKAI roller) – high amplitude and low frequency – mapping

The responses of the embedded geophones and mounted accelerometers during the stationary and moving tests were evaluated in terms of the surface deflections from the drum and ground deflections at two depths. Figures B.5.22 through B.5.24 summarize the surface and ground deflections for the three rollers during the stationary tests. It should be noted that the stationary high-amplitude and high-frequency setting for the CAT roller was not carried out to minimize the damage to the roller. Furthermore, only the data from the low-amplitude and low-frequency setting on the SAKAI roller were obtained since the responses of the sensors during the high frequency and high amplitude vibrations were out of the defined ranged in the data acquisition system.

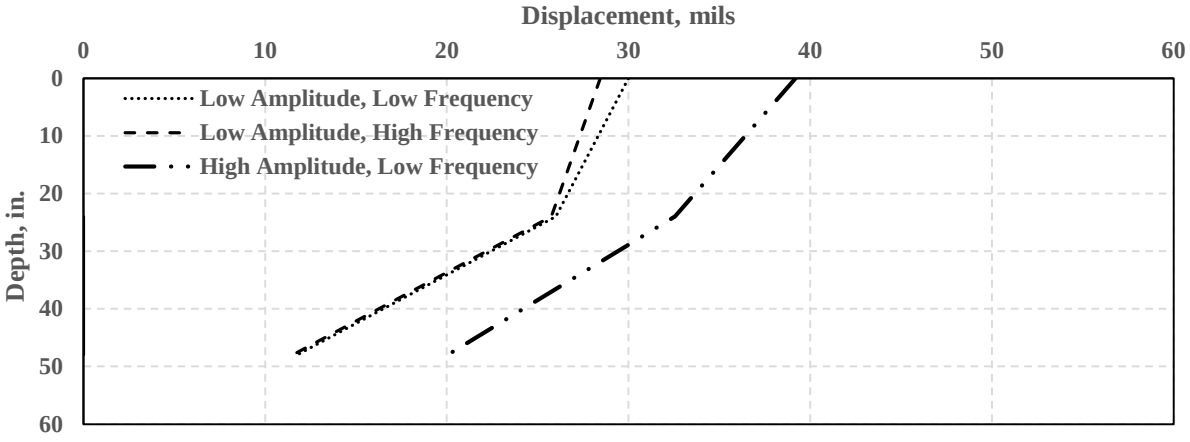

Figure B.5.22. Comparing the surface and ground displacements during different vibration settings – stationary tests (CAT roller)

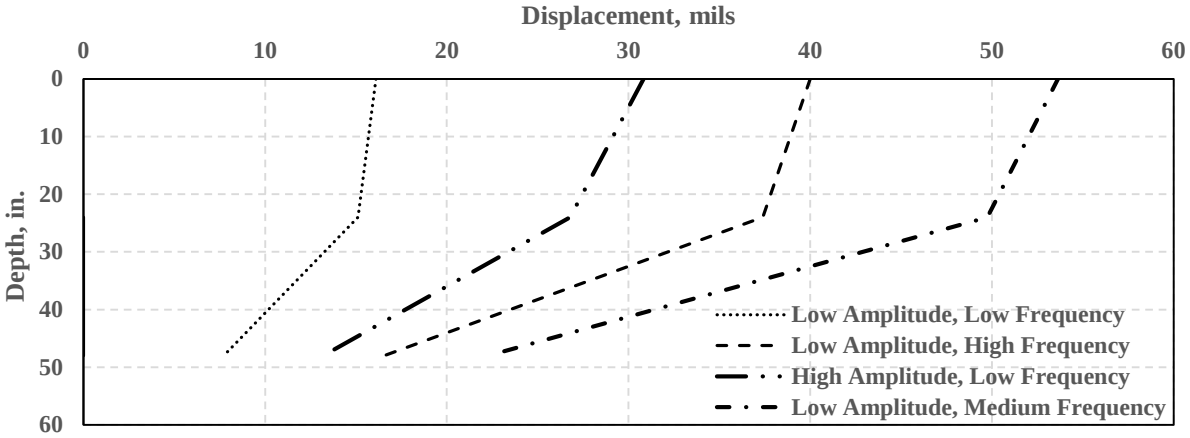

Figure B.5.23. Comparing the surface and ground displacements during different vibration settings – stationary tests (HAMM roller)

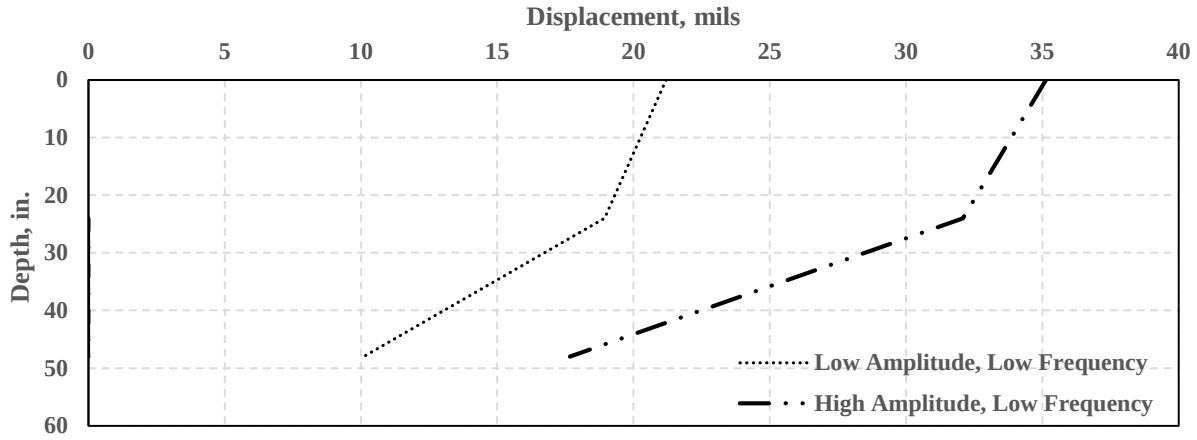

Figure B.5.24. Comparing the surface and ground displacements during different vibration settings – stationary tests (SAKAI roller)

The same types of analysis were performed on the vibration responses of the geophones and accelerometer during the moving tests. Figures B.5.25 through B.5.27 summarize the surface deflections obtained from the mounted accelerometer on the drum and the ground deflections from the embedded geophones during the pre-mapping process. For each roller, two settings were applied to study the impact of the vibration frequency and amplitude on the responses.

Figure B.5.27 summarize the deflections during the low-amplitude and low-frequency as well as high-amplitude and high-frequency for the mapping of the subgrade layer with the SAKAI roller.

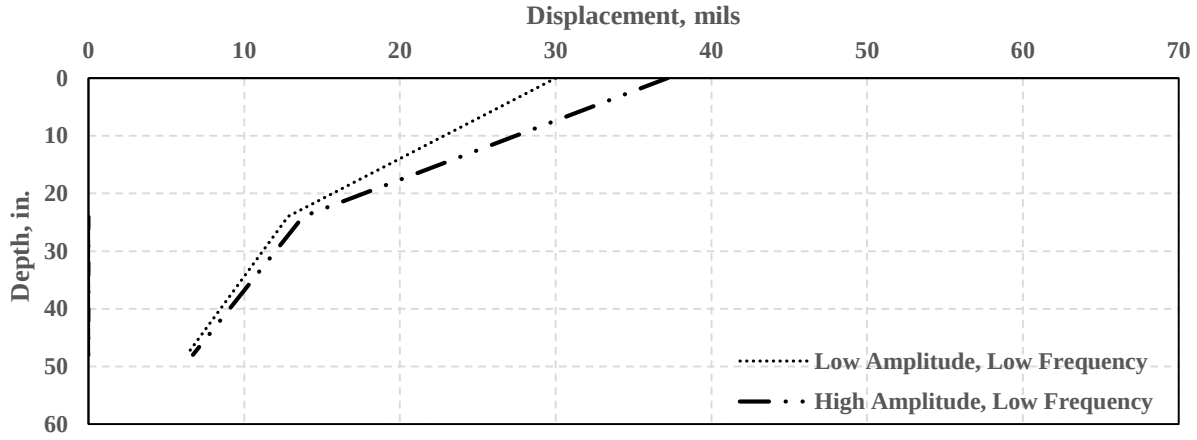

Figure B.5.25. Comparing the surface and ground displacements during different vibration settings – moving tests – (CAT roller) pre-mapping

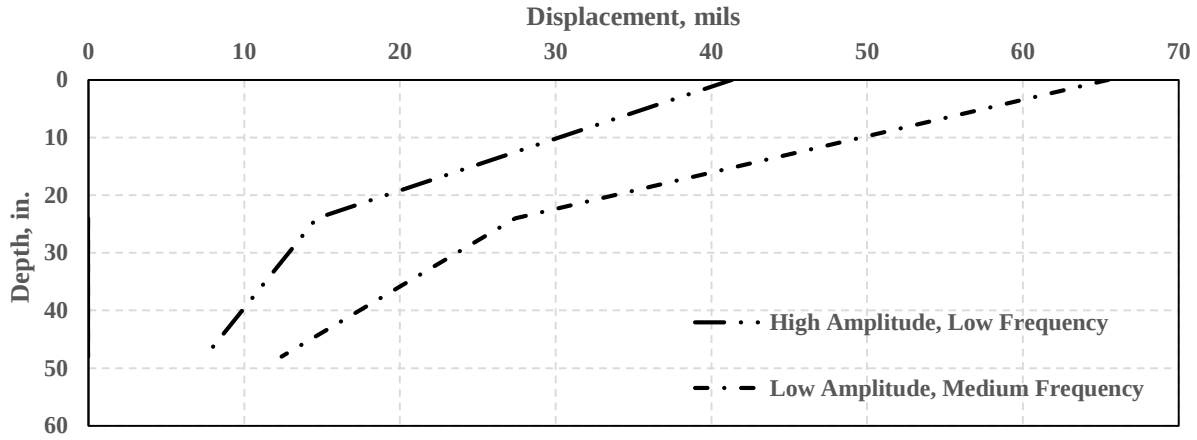

Figure B.5.26. Comparing the surface and ground displacements during different vibration settings – moving tests – (HAMM roller) pre-mapping

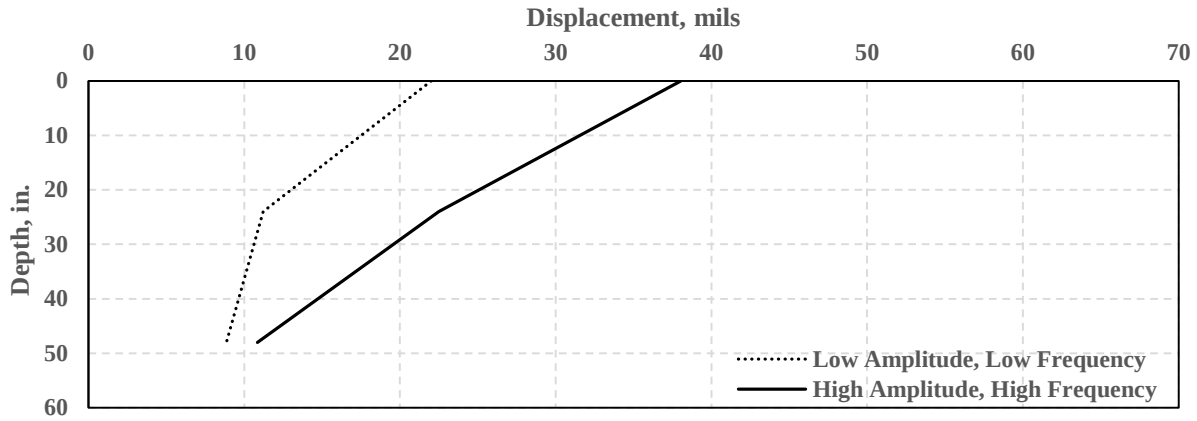

Figure B.5.27. Comparing the surface and ground displacements during different vibration settings – moving tests – (SAKAI roller) pre-mapping

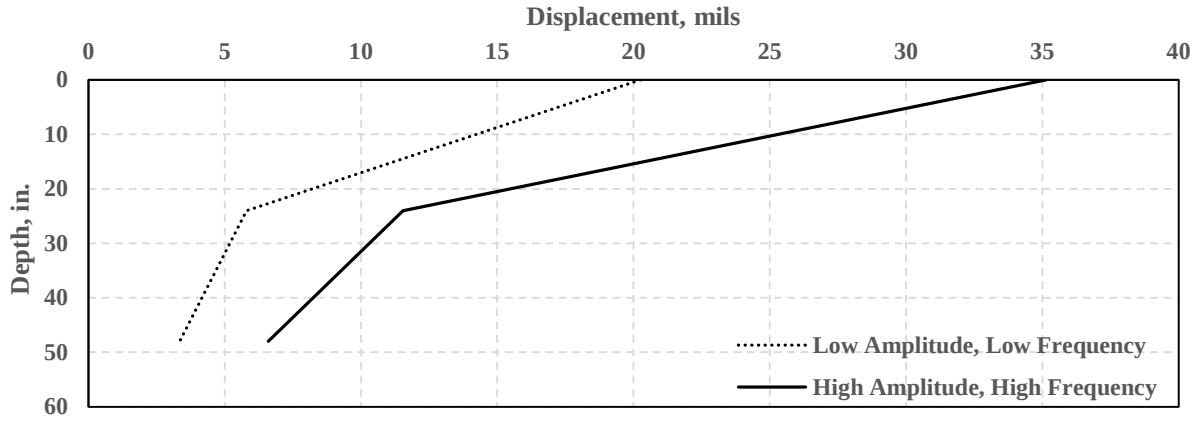

Figure B.5.28. Comparing the surface and ground displacements during different vibration settings – moving tests – (SAKAI roller) mapping

APPENDIX C – DATA REDUCTION PROCESS

C.1. INTRODUCTION

A system was developed in this project to evaluate the vibration characteristics of the IC rollers as well as the response of the ground layers during the IC operations. The roller vibration data were collected with up to two accelerometers mounted on each side of the drum of a roller. The three dimensional (vertical, transversal and longitudinal) responses of the ground layers were recorded using two 3D geophones embedded at different depths. An example of an accelerometer time-record is illustrated in Figure C.1.1. The range of data in this example is about ±1 Volt. A close up view of the acceleration time record from two accelerometers is shown in Figure C.1.2.

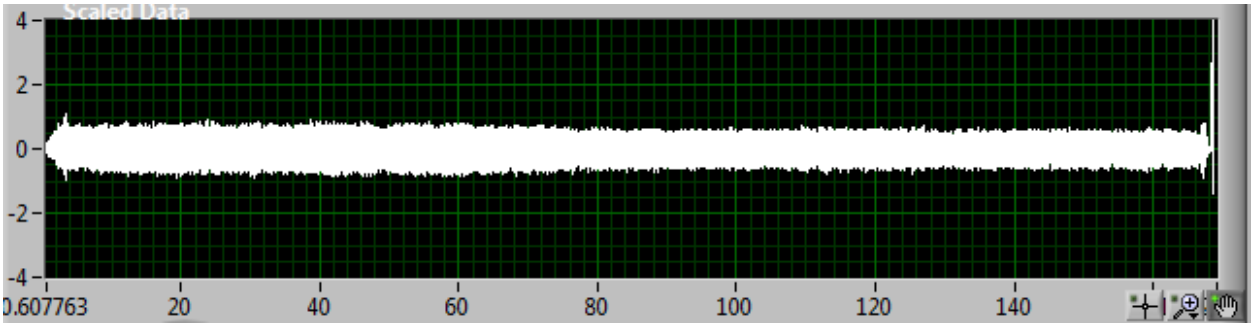

Figure C.1.1. Time-record of acceleration data from both accelerometers mounted on the roller

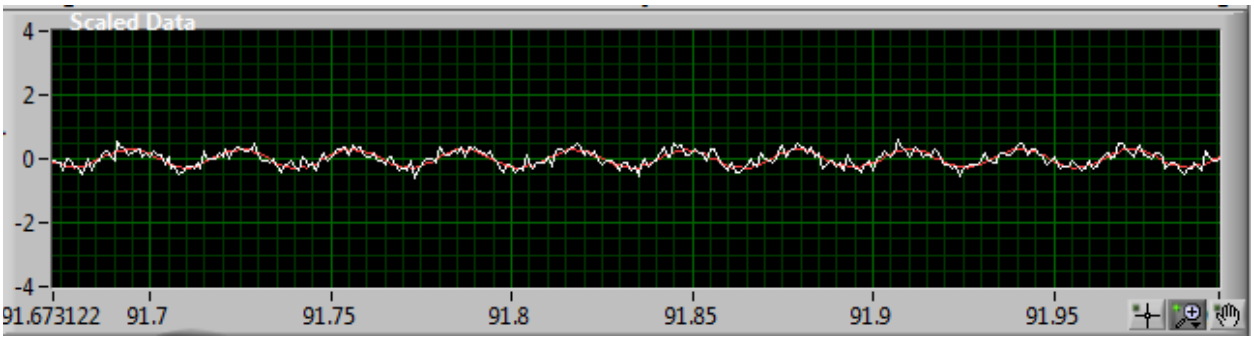

Figure C.1.2. A closer view of acceleration time-record from both accelerometers mounted on the roller

An example of voltage outputs from six geophones is illustrated in Figure C.1.3 for the same pass of the roller as shown in Figure C.1.1. The magnitudes of the responses increase as the roller gets closer to the location of the embedded geophones. A closeup look of the voltage outputs of the six components of the two geophones is shown in Figure C.1.4.

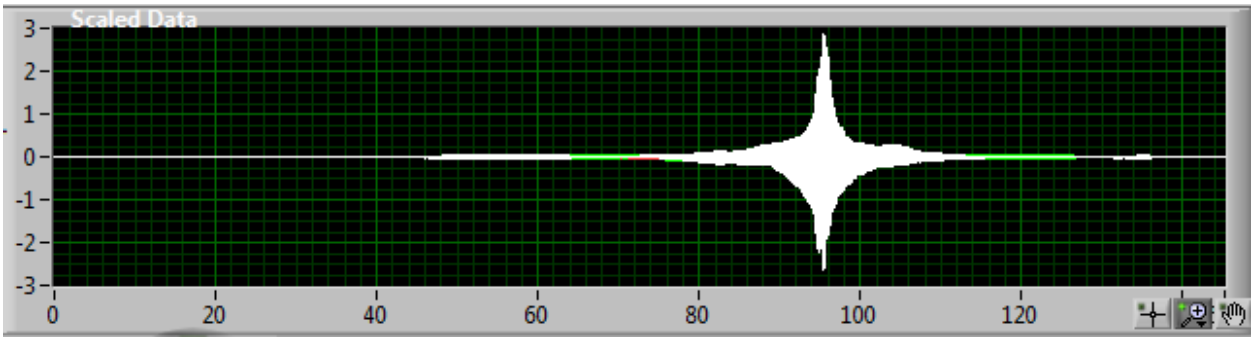

Figure C.1.3. Time-record of velocity data from embedded geophones

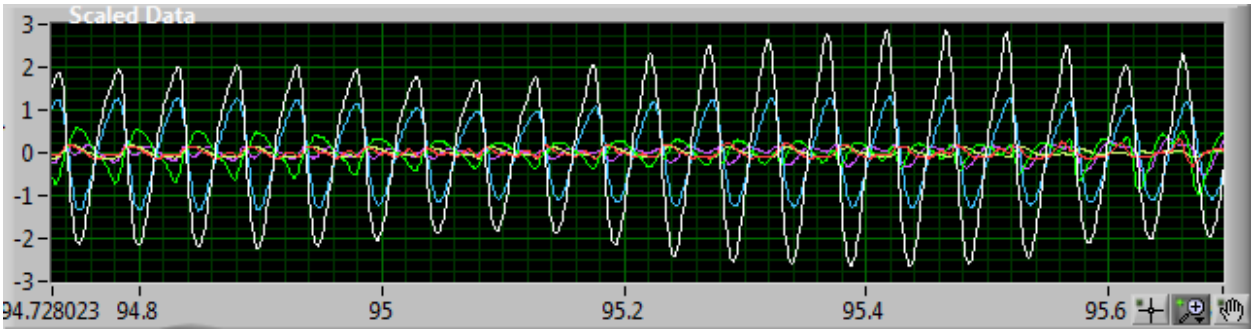

Figure C.1.4. A closer view of time-records for the six responses from the two embedded geophones

C.2. DATA REDUCTION PROCESS

Two GPS units, one on the roller and the other in the vicinity of the embedded geophones, were connected to the two data acquisition systems. Sensor data were collected at 1000 samples per second in 200-point intervals every 0.2 seconds in a synchronized manner. The synchronization was carried out using the GPS clock which was collected at a frequency of 5 Hz (i.e. 5 position data samples per second). Therefore, 200 sensor data samples exist for each reported position of the GPS. The computer time, also synchronized with the GPS clocks, was used for the naming of the files that were generated.

The time-domain voltage outputs were subjected to a Hanning window and then transformed into the frequency domain using a Fast-Fourier Transform (FFT) algorithm. The FFT of a time signal represents the frequency composition of the signal. An example of the amplitude spectrum (amplitude vs. frequency) after those operations on the time-record data is shown in Figure C.2.1. The fundamental frequency and its multiples as well their associated amplitudes were extracted from that amplitude spectrum.

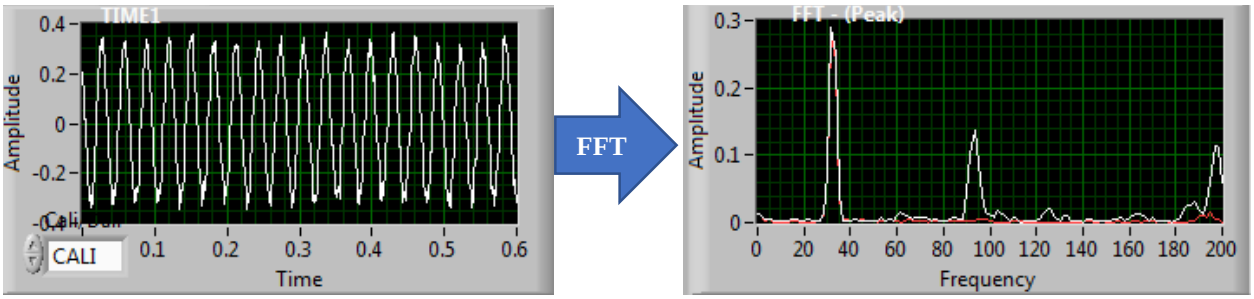

Figure C.2.1. Transforming sensor data from time-domain to frequency domain employing a FFT algorithm

The precision of the analysis in the frequency-domain, Δf, is controlled by the number of data points selected from the time-domain record, N, and the rate of sampling the data in the time-domain, Δt, through:

$$\Delta f = \frac{1}{(N.\Delta t)}$$

As such, the fewer the number of data points and the more densely the time records are sampled, the lower the resolution of the data analysis in the frequency domain. Using blocks of 200 vibration data points digitized at 1000 samples/second results in a frequency resolution, Δf, of 5 Hz, which may not be adequate for the IC application. However, a block of 600 data points was chosen to conduct the FFT, for a frequency resolution of 1.67 Hz. At first glance, it may seem appropriate to utilize more data points to improve the frequency resolution even further. However, such action has an unintended consequence. As more data points are used, the length of the data collected increases. Since the roller is moving during the IC operation, the longer time length translates to longer distance between the data points reported, i.e., the ability of the roller to spot less stiff areas decreases. Considering a roller speed of 2 mph, the spatial resolution of roller measurements is 1.7 ft for 600 data points (0.6 sec). As the best compromise between the frequency and spatial resolutions, the FFT was conducted on 600 points using a moving average of 200 data points (i.e., each frequency-domain analysis was done on 600 points with each two consecutive analyses having 400 points in common. The impact of such decisions on the reduced IC data is discussed further in Section C.3.

Once the FFT algorithm was applied to a block of data, the appropriate calibration was applied to the data to convert voltage output spectrum to either acceleration spectrum for the accelerometers or particle velocity spectrum for the geophones. The accelerometer data were then integrated once to obtain velocity spectrum data and once more to obtain deflection spectrum. The geophones' velocity spectra were differentiated once to obtain the acceleration spectra, and integrated once to obtain displacement spectra. The reduced data in terms of acceleration, velocity and displacement spectra were exported to *.csv files. The generated data in the frequency domain contained the time stamps, GPS coordinates and frequency spectrum data at a Δf of 1.67 Hz. An example of frequency domain data for the two accelerometers mounted on the roller is depicted in Figure C.2.1.

Figures C2.2 and C2.3 represent the steps performed to analyze the geophone and accelerometer data, respectively.

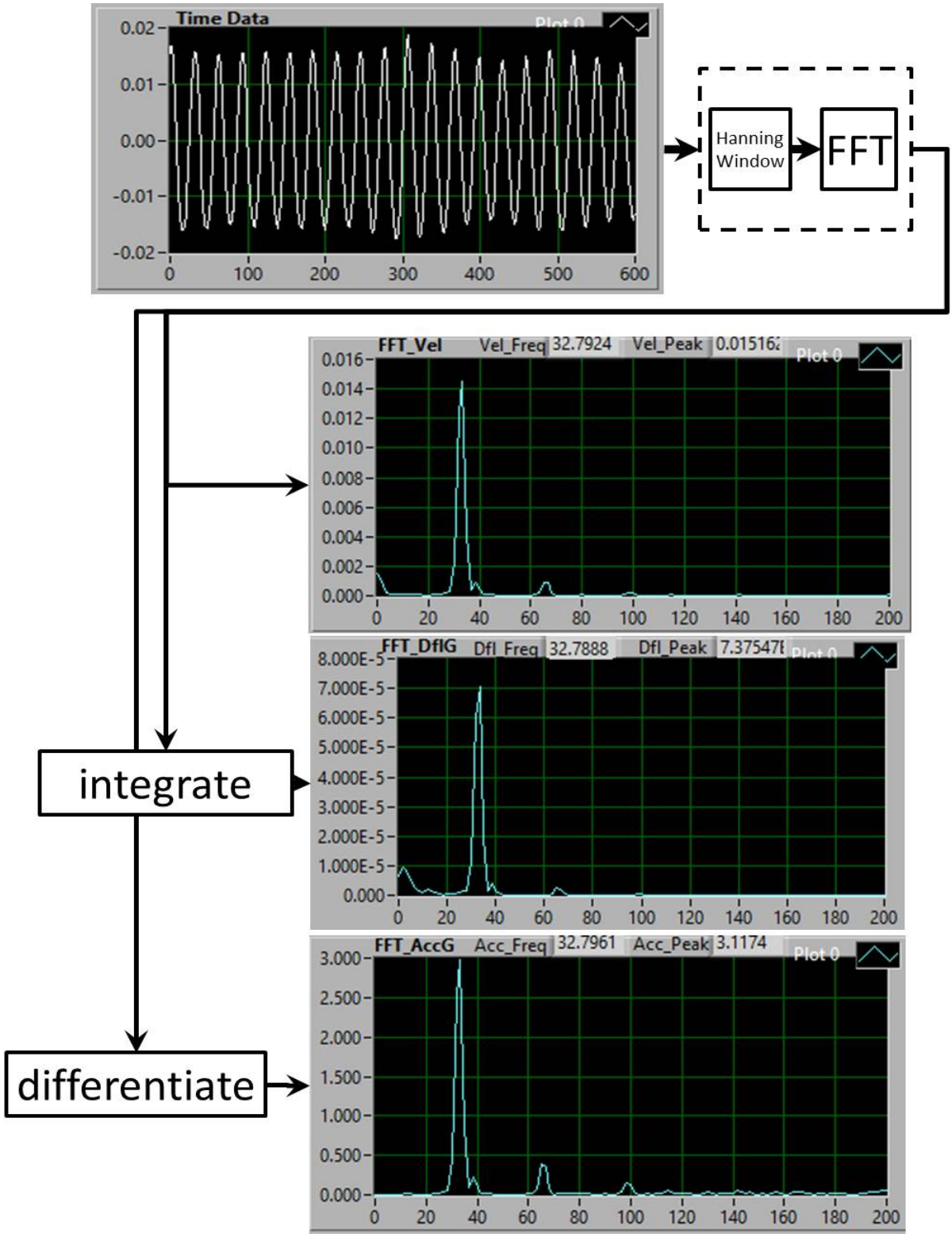

Figure C.2.2. Steps performed to analyze geophone data.

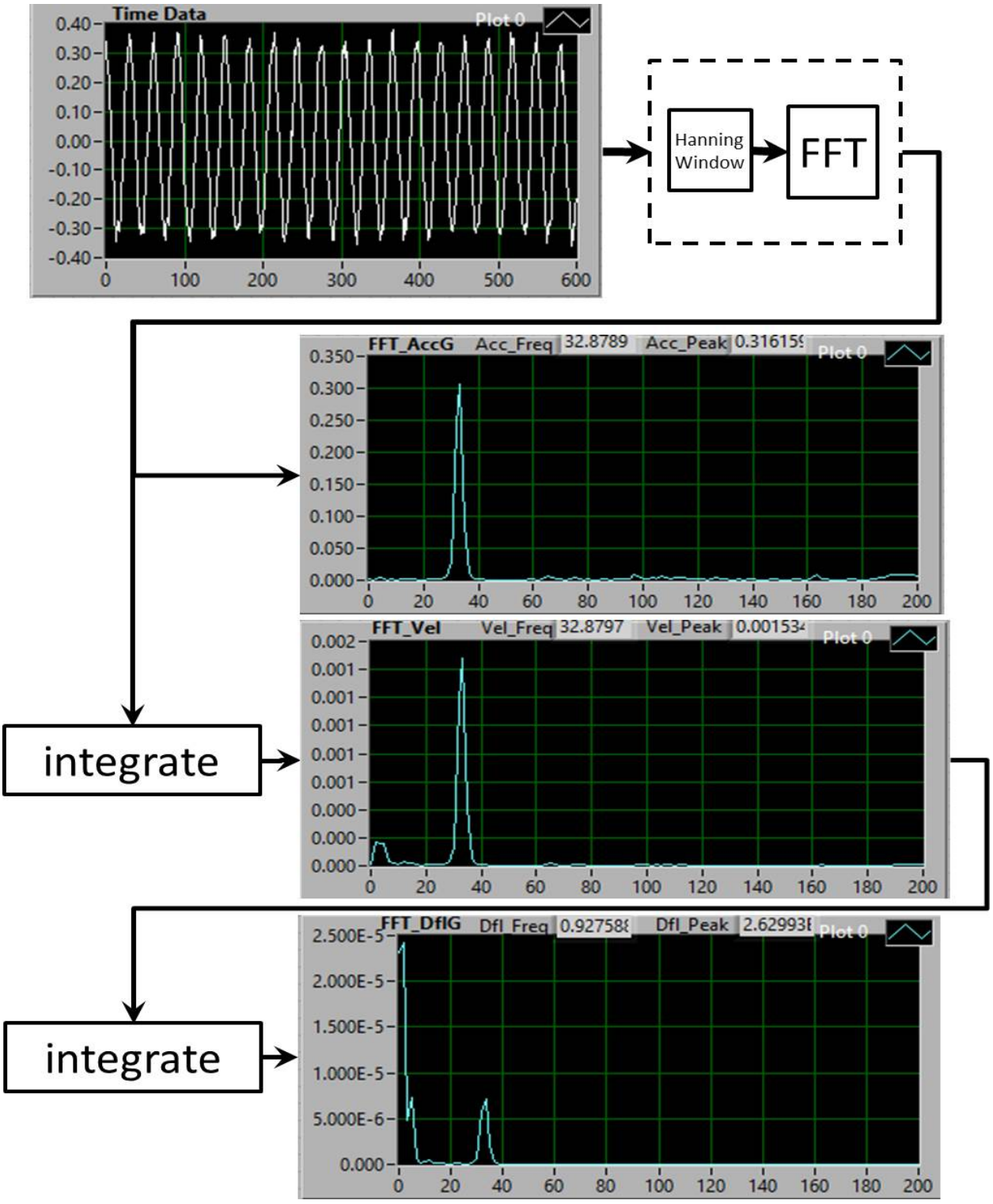

Figure C.2.3. Steps performed to analyze accelerometer data.

The information in the *.csv files were fed into an algorithm developed to identify the fundamental frequency and its multiples as well as the peak amplitudes for each set of collected data.

A summary analyses of the reduced data are included in Chapter 4 and more details for each equipment rodeo are included in Appendices A and B.

C.3. EVALUATION OF DATA REDUCTION APPROACHES

As mentioned earlier, the number of data points used in the analysis of the vibration data to obtain the CMV impacts the frequency and spatial resolutions. Figure C.3.1 summarizes the impact of selecting different number of data points on the peak amplitudes of one set of vibration data for the California site during pre-mapping of the base layer. To maintain the spatial density of the data, a 200 point moving average was used for all cases. As such, the amplitude trend related to the 200 data points does not contain overlapping data between consecutive data points. On the other hand, the results from the 1000 data point analysis contain 800 data points of overlap between the consecutive data points. This overlap will result in a smoothing of the data because of poorer spatial resolution. However, more data points increase the frequency resolution, resulting in more accurate amplitude. Selecting 600 data points seems to be a proper tradeoff between the level of spatial detail and the amplitude fidelity.

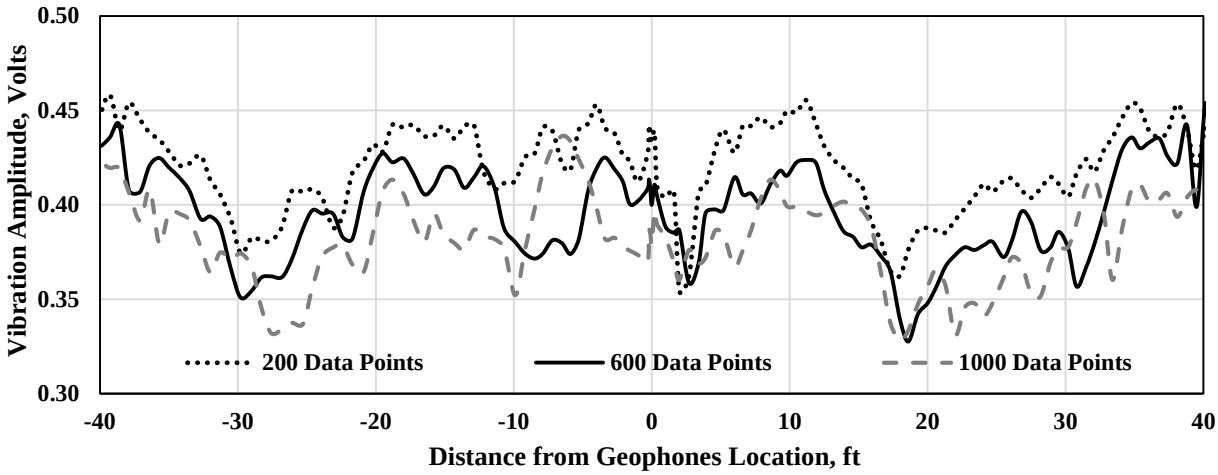

Figure C.3.1. Effect of selecting number of data points in the data block to perform the analysis with moving average on the peak amplitude of vibration

Figure C.3.2 shows the impact of the same analysis on the fundamental frequency of the roller vibration during the operation. Again, increasing the number if data points in the analysis block up to 600 would not impact the results of the vibration frequency. However, such increase will improve the frequency resolution so that subtle changes in the frequency of vibration can be detected. This additional resolution comes at the expense of losing the spatial resolution.

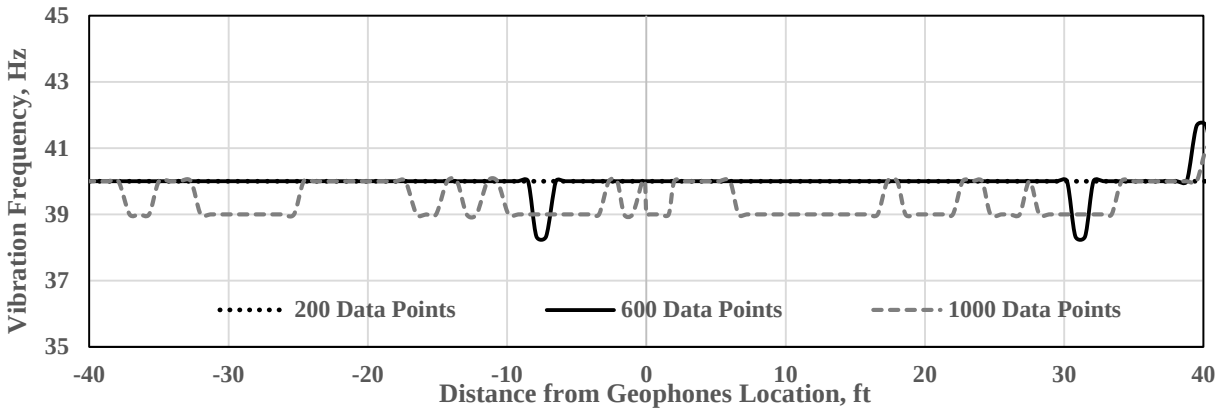

Figure C.3.2. Effect of selecting number of data points in the data block to perform the analysis with moving average on the fundamental frequency of vibration

Figure C.3.3 illustrates the impact of selecting a different number of data points on the calculated CMVs. Expectedly, increasing the number of data points increases the confidence in the values of the CMVs, once again at the expense of smearing the details along the roller path.

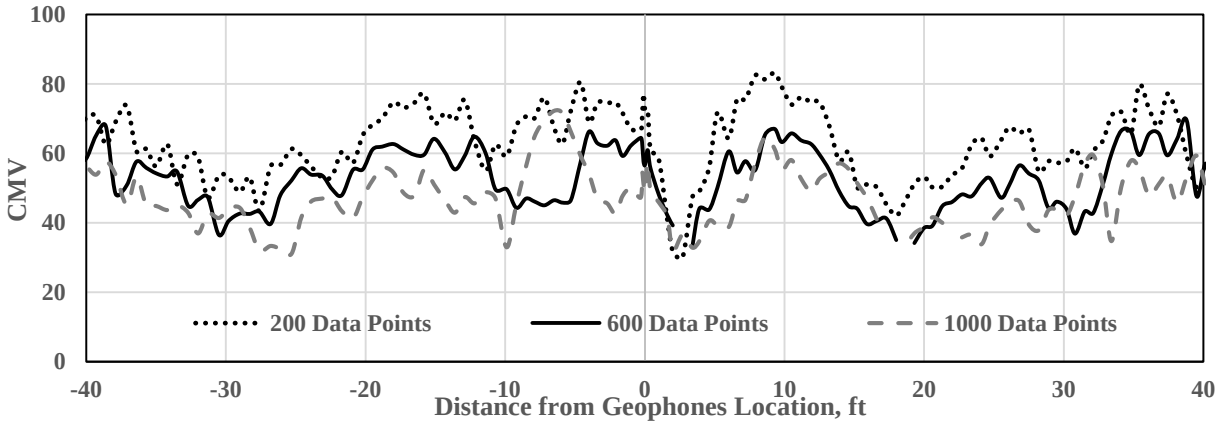

Figure C.3.3. Effect of selecting number of data points in the data block to perform the analysis with moving average on the calculated CMV

Another way of analyzing the vibration data for calculating CMV is to eliminate moving averaging from the analysis, as illustrated in Figure C.3.4. In this case, as the number of data points increases, the spatial interval between consecutive data points increases. As such, increasing the number of data points in this process acts like a smoothing algorithm.

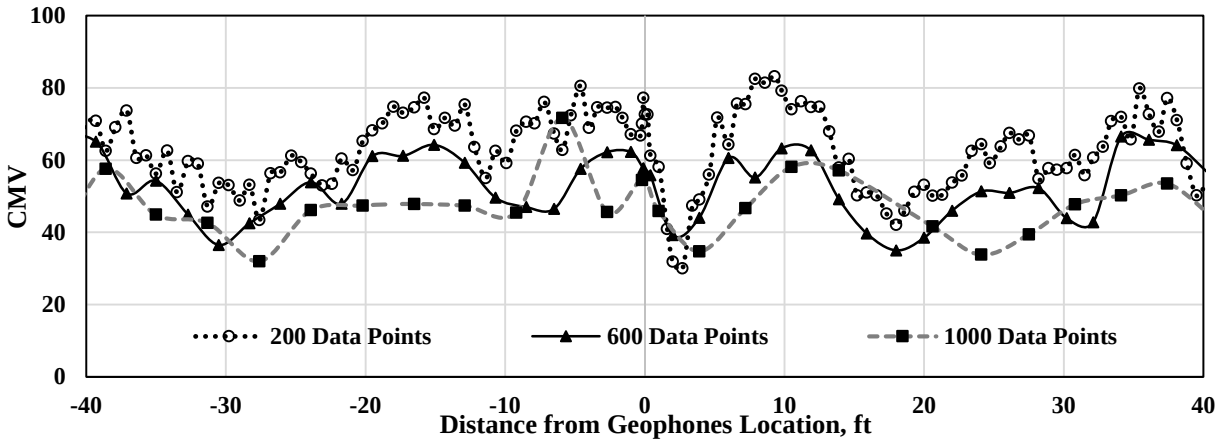

Figure C.3.4. Effect of selecting number of data points in the data block to perform the analysis with no moving average on the calculated CMV

Figure C.3.5 compares the CMVs from 600 data points with and without moving averaging. The data corresponding with the 200 point moving average seems to be a good compromise between the level of spatial detail and the accuracy of the CMVs. As such, these parameters were selected in this project. This type of analysis applies to the CMVs reported by the other systems as well. However, the research team does not know the analysis parameters selected by the different vendors. Some of the differences in the results among the different systems can be attributed to this phenomenon.

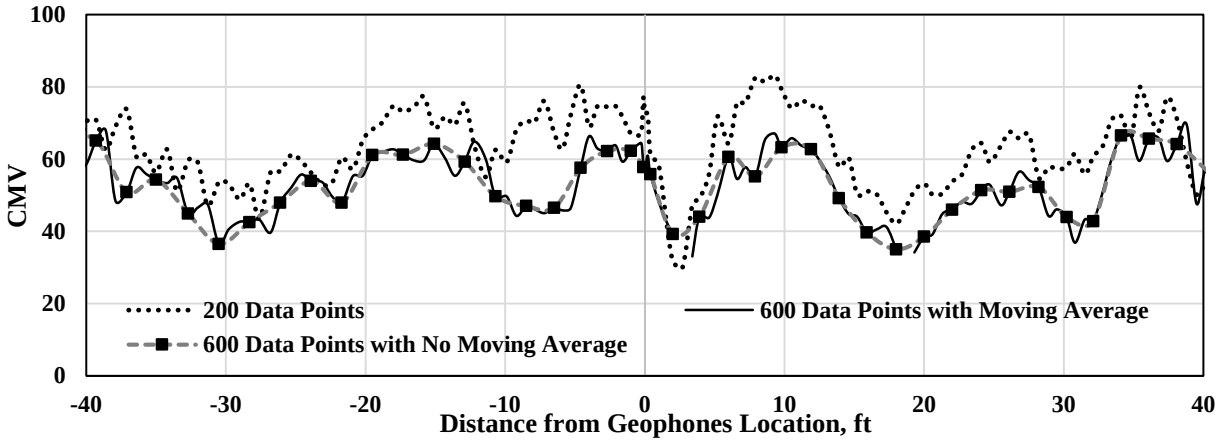

Figure C.3.5. Effect of selecting the data reduction approach on the calculated CMV

APPENDIX D – TRAINING MATERIALS

For access to the presentation and video please send an e-mail to ctis@utep.edu

EDC2 - Intelligent Compaction Retrofit Kits Evaluation

Standard Procedure for Retrofit Kit Installation and Setup
Part 1 – Summary Guidelines



Outline

- Introduction to IC Retrofit Kit
- Components of IC Roller Kits
- How IC Retrofit Kit Works
- Features, Benefits and Limitations of IC Retrofit Kit
- Comparison of Retrofitted and OEM IC Rollers
- Operational Steps For Installation of Retrofit Kit
- Initial Setup Of IC Retrofit Kits

Introduction to IC Retrofit Kit

Two Types of IC Rollers

OEM IC roller is equipped with Factory-Installed IC components	IC Retrofit components are installed on a host conventional roller as an after-market component
Original Equipment Manufacturer (OEM) IC Roller	IC Retrofit Kit

Performance of IC Retrofit Kits

- Performance of retrofitted IC rollers depends on following factors:
  - ✓ Roller model and make (i.e., physical configuration of drum)
  - ✓ Position of vibration sensor (accelerometer) on roller
  - ✓ Accuracy of GPS system
  - ✓ Availability of local (virtual) base stations

Retrofit Kit vs. OEM IC Roller: Sensors

Retrofitted Sensor | **OEM Sensor**


Retrofit Kit vs. OEM Systems: In Cab Control

(This setup was prepared for research purposes and it's not common)

IC Retrofit Kit: Introduction

Retrofitting existing roller with IC Retrofit Kit is generally more affordable than purchasing new OEM IC rollers

It can be installed on almost any vibratory rollers

IC Retrofit Kit: Components

*Image Courtesy of Trimble

IC Roller Kit: Components' Functions

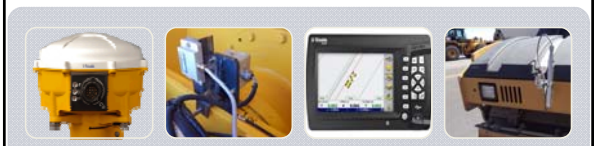

GPS information is used to track roller positions for IC measurements	Accelerometer is used to collect roller vibration data for computing intelligent compaction measurement values (ICMV)	Onboard computer provides real time display of IC measurements maps	Temperature sensors for use with asphalt IC rollers

*Image Courtesy of Trimble

IC Retrofit Kit: Information

Maps	Feedback	Reports
Pass Count	Speed	Compaction Performance
ICMV	Location (GPS)	Coverage Map
Temperature (for asphalt operations)	Amplitude	ICMV Data
	Frequency	

IC Retrofit Kit: Feedback

Compaction Monitoring with

- pass counts, surface temperatures
- roller speed, vibration frequency and amplitude
- color-coded ICMV map

In-field compaction reports (optional)

Avoiding over/under-compaction and identification of soft spots

IC Retrofit Kits: Initial Set Up

GPS Setup and verification

- Connect GPS receiver to a local GPS base station or Virtual Reference System (VRS).
- Configure GPS settings to select required coordinate system.
- Verify GPS readings with a standard traceable measurements such as hand-held rover.

Accelerometer Mounting and Verification

- Select proper location to mount accelerometer
- Ensure accelerometer is mounted so that direction of measurement is vertical (as marked on sensor)
- Ensure accelerometer is mounted firmly to avoid wobbling.
- Route cables properly to avoid loose connection and damage.

Onboard Display Setup

- Select proper measurement unit and coordinate system (UTM or State Plane).
- Ensure proper connection with GPS and sensors.
- Customize display parameters for IC maps (pass counts, ICMV, temperatures, speed, amplitude, frequency and amplitudes)

IC Retrofit Kits: Things to Remeber

Employ a certified technician to install IC Retrofit Kit

Export IC data via:

USB Drive or Cloud Storage

Verify integrity of Data Collected Daily

Operation if IC Roller/Retrofit Kit: Contractor's Check List

- Check that IC system works properly before collecting data
- Avoid mounting accelerometer on damped parts
- Create a new data folder for each operation
- Verify GPS readings to avoid data shift
- Include pre-mapping (if possible) and mapping processes
- Make sure that roller is on vibration mode during pre-mapping and mapping
- Maintain required speed, amplitude and frequency during pre-mapping and mapping
- Monitor color-coded maps for roller overlaps and identification of soft spots
- Transfer IC data to storage (thumb drive or cloud) on a daily basis

IC Roller/Retrofit Kit Operation: Inspector's Check List

- Receive IC data from contractor/operator on a daily basis
- Check for possible data shift after each day of operation
- Check IC data quality and quantity before acceptance
- Check for possible zeros and negative numbers in IC data
- Transfer IC data to data storage

IC Roller/Retrofit Kit: Daily Maintenance Check List

- Ensure Vibration Sensor is working properly
- Check GPS Data Quality (fixed or float)
- Ensure Temperature Sensors (if applicable) are working properly
- Check IC Settings of In-Cab Control Box
- Perform a Dry Run to Ensure Proper Data Collection
- Report any Malfunction to Engineer Immediately

EDC2 - Intelligent Compaction Retrofit Kits Evaluation

Standard Procedure for Retrofit Kit Installation and Setup
Part 2 -Video Tutorial



Operational Steps for Installation of IC Retrofit Kit

APPENDIX E – FREQUENTLY ASKED QUESTIONS

- *What is intelligent compaction retrofit kit?*

  The intelligent compaction (IC) retrofit kit (after-market kit) is an alternative option from original equipment manufacturer (OEM) IC systems that can be installed on a regular vibratory compactor and collect IC data. The retrofit kit can be installed on both single-drum and double-drum vibratory rollers for asphalt and soils applications.

- *What are the components of an IC retrofit kit?*

  An IC retrofit kit comprises of:

  - an accelerometer that is mounted inside the drum to capture the vibration of the drum
  - an in-cab control box that is designed to collect IC data and display live information to operator
  - a GPS receiver and antenna that are installed on the cabin and connected to the in-cab control box to record GPS coordinates
  - connections/wires, to connect the accelerometer and GPS system to the in-cab control box

- *What is the installation process for an IC retrofit kit?*

  A summary of installation steps along with a video tutorial is provided in Appendix D of this report. The retrofit kit should be installed by a certified technician to ensure proper operation. A dry run on a test section should be performed prior to the IC data collection process.

- *What are the available IC retrofit kits?*

  The only available IC retrofit kit during this study was manufactured by Trimble®. Recently, TOPCON® has also introduced an IC retrofit kit.

- *What is the measurement unit of IC data collected by the retrofit kit?*

  The retrofit kit provided by Trimble represents the stiffness as Compaction Meter Value (CMV), which is the same for the OEM system on the CAT roller. The SAKAI OEM system reports the stiffness as Compaction Control Value (CCV). The OEM system on the HAMM roller estimates the stiffness as HAMM Measurement Value (HMV). All the above ICMVs are unitless. On the other hand, the roller-integrated soils stiffness K_b value and vibration modules E_{vib}, which were not evaluated under this study, use physical units of stiffness. The vibration data collected with the data acquisition system developed for this study are in terms of raw vibration signals that can be used to calculate either CMV, CCV or HMV as necessary.

- *What are the precautions prior to the IC operation using the retrofit kit?*

  The installed system should be carefully checked to ensure that the components are properly connected and that the vibration sensor is mounted vertically, securely and in a position that can capture the actual vibration of the drum. The roller configuration and installation parameters should be defined as part of the installation of in-cab control box. In some IC systems, the design file could be uploaded for better understanding of the roller position during the operation.

- *What is the process to calibrate GPS system?*

  GPS calibration process should be performed prior to any data collection. Either a physical or virtual base station along with a hand-rover could be utilized to perform the calibration process. The corrected GPS coordinates should be applied to the in-cab control settings. For a detailed calibration process please refer to Section 3.4 of the main report.

- *Can we use a virtual reference system (VRS) to calibrate the GPS?*

  Even though the use of virtual base stations was successfully conducted in this study, it is recommended to use a survey-grade handheld rover to accurately calibrate the GPS units of IC systems prior to the field operations.

- *How can we transfer IC data from retrofit kit?*

  The data transfer process was evaluated in this study using cloud storage and a thumb drive. Downloading the collected IC data through each vendor's online data management system (e.g., VisionLink for Trimble/CAT, SiteLink3D for Topcon/Sakai and HAMM Compaction Quality navigator) seems to be more straightforward. Even though transferring collected IC data through a thumb drive is included in the retrofit kit options, it is recommended to download the IC data through the cloud storage and export them to specific file format for further analysis.

- *How frequent should we download IC data from the retrofit kit?*

  Since operational malfunction or missing data without the knowledge of the QC manager/ technician can occur, the collected data should be downloaded daily, either from the cloud storage or locally using a thumb drive, and checked to ensure integrity of the data.

- *How to interpret collected IC data from a retrofit kit?*

  The interpretation of IC data collected by a retrofit kit is similar to that of OEM systems. For a reasonable geospatial interpretation of collected IC data, a color-coded map is recommended. Even though different color levels could be used based on various statistical parameters, this study recommends the use of three colors (green, yellow and red) based on the concept that the green areas representing stiffer areas while the red areas representing the less stiff areas. It is recommended to color-code the ICMV using the quantile classification method as discussed earlier in this report.

- *How can we manage IC data collected by a retrofit kit?*

  Since IC data are associated with GPS coordinates, geospatial and geostatistical data analyses should be performed on collected data. Veta® is a standard tool required in the FHWA, AASHTO, and many DOT IC specifications to view IC data on the map and perform statistical analysis on the collected data. The ArcGIS package can be used as a research tool to conduct more advanced analyses.